ABSTRACT

Title of Document: INTENSE LASER ACCELERATION OF QUASI-MONOENERGETIC PROTONS

Tung-Chang Liu, Doctor of Philosophy, 2013

Directed By: Professor Chuan S Liu, Physics

By irradiating an ultra-thin overdense foil with an intense circularly polarized laser beam, the laser radiation pressure can push the foil forward. This scheme, laser radiation pressure acceleration, is one of the most actively studied laser-plasma acceleration scheme to generate quasi-monoenergetic proton beams. However, during the acceleration process, the Rayleigh-Taylor instability may destruct the foil into a bubble-like structure with interleaving high and low density regions. The laser will then penetrate through the underdense transparent regions and cease to push the electrons effectively.

To overcome the short acceleration duration problem, a multi-species foil instead of a pure hydrogen foil is applied. The proton layer can continue to be accelerated by the Coulomb repulsion force from the partially shielded heavy ions even after electrons becoming underdense. The scheme combining shielded Coulomb repulsion and radiation pressure acceleration can significantly extend the acceleration time and obtainable proton energy with quasi-monoenergetic properties.

In this work, we examine by numerical simulation the whole process of the laser proton acceleration scheme, including the energy evolution of radiation pressure acceleration, the development of the Rayleigh-Taylor instability, the effect of shielded Coulomb repulsion using a multi-species foil and further improvement in the scheme itself to pursue a high energy quasi-monoenergetic proton beam accelerated by an intense laser beam.

INTENSE LASER ACCELERATION OF QUASI-MONOENERGETIC PROTONS

By

Tung-Chang Liu

Dissertation submitted to the Faculty of the Graduate School of the
University of Maryland, College Park, in partial fulfillment
of the requirements for the degree of
Doctor of Philosophy
2013

Advisory Committee:
Professor Chuan S Liu, Chair
Professor Wendell Hill
Professor Kiyong Kim
Dr. Xi Shao
Professor Philip Sprangle

© Copyright by
Tung-Chang Liu
2013

Dedication

Dedicated to my parents.

Acknowledgments

There are a number of people without whom this thesis might not be written, and to whom I am greatly indebted.

I would like to express the deepest appreciation to my parents, Chin-San and Liang-Yiu, who are always encouraging and supportive throughout these years when I was pursuing the doctoral degree alone in a foreign country.

I would like to express my sincere gratitude to my committee chair, Prof. Chuan-Sheng Liu, for the continuous support of my Ph.D. study and research, for his patience, motivation, enthusiasm, and immense knowledge. Without his guidance and persistent help, this dissertation would not have been possible.

I would like to thank my co-advisor, Dr. Xi Shao, for his patiently continuous guiding in every aspect and every detail of my research works.

I would also thank Dr. Jyhpyng Wang and Dr. Shih-Hung Chen for providing precious opportunities to access their advanced computing resources and to collaborate with excellent experimentalists.

I would also thank all my colleagues, Dr. Jao-Jang Su, Dr. Min-qing He, Dr. Galina Dudnikova, Dr. Roald Sagdeev and Dr. Dennis Papadopoulos for their precious comments and suggestions.

I thank the committee members, Dr. Wendell Hill, Dr. Kiyong Kim and Dr. Philips Sprangle (alphabetically) for spending time attending my doctoral defense and willingly providing their precious comments.

I also thank University of Maryland for providing me the opportunity to pursue the Ph.D. degree here and for the financial support as a teaching assistant for the first few years. I would also like to thank the funding agency, NSF DoE for the financial support.

I also place on record, my sense of gratitude to one and all who, directly or indirectly, have lent their helping hand in this venture.

Table of Contents

List of Tables

List of Figures

Chapter 1

Introduction

In 1873, James Clerk Maxwell derived the existence of radiation pressure from his electromagnetic theory [1], and Adolfo Bartoli also derived from thermodynamics that radiation emitted by a body with nonzero temperature should impart a pressure to an object due to reflection in 1876 [2]. However, the radiation from normal light sources such as sunlight or light bulbs are so feeble that it could not be experimentally detected until 1900, when Pyotr Lebedev measured experimentally the pressure of light [3], not to mention to be applied in particle acceleration. In 1917, Albert Einstein established the theoretical foundations for the laser (light amplification by stimulated emission of radiation) [4] via a re-derivation of Max Planck's law of radiation [5]. In 1950, Alfred Kastler proposed the method of optical pumping [6], and four years later, James P. Gordon, Herbert J. Zeiger and Charles Hard Townes applied this technique to produce the first maser (microwave amplification by stimulated emission of radiation) [7], which then opened up the possibility to use light to accelerate particles.

1.1. High-Intensity Laser

At the time where laser was first invented, although the light beam had the advantages of being non-dispersive, monochromic and in-phase, which could largely concentrate the intensities at a small focal point, the focused intensity is still not significant enough for application in particle acceleration compared to the contemporary particle accelerators such as linear particle accelerators (first built by

Rolf Wideröe in 1928 [8],) cyclotrons (invented by Ernest Lawrence and first operated in 1932 [9]) or synchrotrons (first constructed by Edwin McMillan in 1945 [10].) The main difficulty limiting the laser intensity is the damage to the gain medium through nonlinear processes such as self-focusing at intensities of gigawatts per square centimeter. Under this consideration, the peak power of laser pulses was limited to sub-terawatt level for very large multi-beam facilities in order to maintain the intensity of laser pulses below the threshold of the nonlinear effects.

In 1985, Donna Strickland and Gérard Mourou demonstrated chirped pulse amplification (CPA) for lasers [11], successfully increasing the laser intensity to terawatt, and subsequently petawatt level. The technique of CPA was originally used to increase the available power in radar (radio detection and ranging) in 1960 [12]. In CPA, a short laser pulse is stretched out in pulse duration prior to the gain medium using a pair of gratings that are arranged so that the component of higher frequencies of the laser pulse travels with longer path lengths. After going through the grating pair, the laser pulse duration is extended by a factor of 10^3 to 10^5, and hence the intensity is sufficiently low compared with the intensity limit of the gain medium. After being amplified by a factor 10^6 or more, the lengthened laser pulse is recompressed back to the original pulse width through the reversal process of stretching. With the technique of CPA, the peak power of output laser pulse can achieve orders of magnitude higher than before[13], essentially leading to the possibility of accelerating particles by high-intensity lasers.

1.2. Laser-Electron Acceleration

The application of laser acceleration of objects can be traced back to 1966, when G. Marx proposed to use laser to propel interstellar vehicle distantly [14]. Although the obstacle of the original proposal was considered insurmountable after being reviewed 25 years later [15], laser propulsion was proven feasible in idea and was first designed by Arthur R. Kantrowitz in 1972[16]. The concept that laser beams are capable of generating high energy particles was also successfully demonstrated and continually studied.

The laser-electron accelerator was first proposed in 1979 by Tsuyoshi Tajima and John M. Dawson[17] to acquire high-energy electrons by the schemes of laser wakefield acceleration (LWFA) and laser beat wave acceleration (LBWA) with electric fields of the order of tens of gigavolts per centimeter and short pulse duration. Great progress has been made since successful production of mono-energetic electrons in 2004 [18–20]. Quasi-monoenergetic electrons close to 1 GeV has recently been obtained as well[21,22], and effective acceleration of multi-GeV electrons and strong field gradients has also been observed in Stanford Linear Accelerator Center (SLAC) experiments[23].

There are several mechanisms of contemporary laser-electron acceleration, and most of them are based on wakefield acceleration, such as LWFA, LBWA and self-modulated laser wakefield acceleration (SMLWFA) [23,24]. In wakefield acceleration, when a well-tailored laser beam propagates in the neutral media, the ponderomotive force evacuates the electrons at the wave front, and the abundant ions in the bubble-region then attract electrons from the back with great acceleration field. The laser

amplitude profile is modulated to construct resonance condition between the wavelength of the electron plasma wave and the length of a node (LBWA) or the length of the laser pulse (LWFA) so that the electrons at the rear side of the ion bubble can surf on the peak of the electric field stably and be accelerated to nearly speed of light within a significantly shorter distance compared to the traditional radio-frequency (RF) acceleration scheme.

1.3. Laser-Proton Acceleration

After successful experimental demonstrations of electron acceleration, the possibility to accelerate ions with high-intensity laser then attracts lots of interests. Unfortunately, the acceleration of ions by laser irradiation of foils has been pursued actively by experiments, theory and simulations, but the wakefield scheme proposed in laser-electron acceleration could not be applied to accelerate ions since they are nearly stationary within electron-plasma oscillation period. However, laser acceleration of protons has been successfully achieved with different mechanisms. There are also several mechanisms for proton acceleration with laser irradiation on a foil such as target normal sheath acceleration (TNSA), radiation pressure acceleration (RPA) , shielded Coulomb repulsion (SCR), shock acceleration, etc.

TNSA is the first experimentally verified laser-proton acceleration scheme to generate protons with energy up to MeV level, where the target foil with thickness ranging from a few to several tens of laser wavelengths are applied[25–35]. In TNSA, the hot electrons in the target foil are heated by high-intensity linearly polarized laser beam, escaping from the rear side of the foil, and consequently, protons are accelerated

by the electric field created by the hot electrons. The requirement for TNSA is relatively lower than other laser-proton acceleration schemes. However, in most cases, the resulting ion energy spectra are broad and only few protons reach the maximum energy, which is less suitable for applications requiring monoenergetic protons.

On the other hand, with additional requirements on laser and foil profiles, RPA can produce high energy protons with monoenergetic properties. The scheme of RPA has been actively studied in theory and simulation [36–48] and by experiment [49]. In RPA, almost all the electrons of the ultra-thin foil are pushed forward by the laser ponderomotive force of a circularly polarized laser beam, forming charge separation between the electron and proton layers. The proton layer is then accelerated by the electrostatic force due to such charge separation. These two layers are accelerated as a whole like a light sail pushed by the laser radiation pressure. Using a circularly polarized laser beam with high contrast ratio and an ultra-thin foil, RPA is a more efficient acceleration process for producing high energy monoenergetic protons, suitable for many applications requiring that the accelerated protons have good beam quality and a narrow energy spectrum.

It has been shown by theory and simulation that RPA is stable in one-dimensional (1D) environment[40,42] and can continuously accelerate the protons unlimitedly. However, it has also demonstrated with two-dimensional (2D) particle-in-cell (PIC) simulations[39,41,43–45,50–52] that the Rayleigh-Taylor instability (RTI) can limit the acceleration achieved by RPA and undesirably broaden the proton beam's energy spectrum so that significantly less protons carry the desired energy. RTI is one of the most important instabilities arising when a thin plasma foil is accelerated by the

laser radiation pressure. It puts a limit on the time a foil can be accelerated before it becomes transparent to the laser light and loses its monoenergetic properties. For RPA of a thin-foil target of one species, the energy scaling study with PIC simulations[44] indicates that a petawatt power laser is needed to obtain around 200 MeV quasi-monoenergetic protons. Several researches on understanding and overcoming the unfavorable RTI effect were performed[51–55], and it is still an ongoing problem.

In order to overcome this disadvantage, several schemes have been studied[47,54–61], including modifying laser polarization, foil shape, applying target foils with multiple layers or multiple species. Among these schemes, we are particularly interested in the scheme using a foil made of multiple species, as it can significantly increase the proton energy without losing its monoenergetic property and is practical to be applied by experiments. Two mechanisms have been proposed on laser acceleration of protons using multi-species foils. One is direct Coulomb explosion[56], which accelerates the protons by heavy ions after sweeping nearly all the electrons away by extremely high-intensity lasers. The other is leaky light sail acceleration[57], which accelerates the protons by partially remaining radiation pressure when the electrons are ahead of protons with their density slightly below the critical value. However, neither of these mechanisms can be applied to the parameter range that we are interested in since we use moderate laser intensity and thin foils so that the electrons, with their density soon becoming far below the critical value, cannot be fully removed from the system.

We analyze the simulation results of laser acceleration of protons from a multi-species thin foil made of carbon and hydrogen (C-H foil) and found that there are two

different stages involved during the acceleration process: the RPA and the shielded Coulomb repulsion (SCR). The RPA first separate the protons from the carbon ions due to their different charge-to-mass ratio while the electrons are overdense, and then the left-behind carbon ions continue to push the protons stably by electron shielded Coulomb repulsion. The Coulomb repulsion to the proton layer by the carbon layer can help remedy the RTI and further accelerate the protons. By solving the equation of motion by 1D Poisson equation, we realized that there is soliton-like structure in the localized carbon ion density distribution, which is also observed by experiments [62], and that the acceleration is positively related to two crucial parameters: the number of electrons escaping in transverse dimension and the electron temperature. Consequently, we then modified the laser polarization and spot size profiles to increase the value of these parameters and successfully achieved significant improvement in the obtainable proton energy.

1.4. Medical Implications of Quasi-Monoenergetic Proton Beams

One major motivation of active researches in the generation of high energy monoenergetic proton beams is the applications in proton cancer therapy. The concept of using high energy proton in cancer treatment is first proposed by Robert R. Wilson in 1946[63]. Using high energy ion beams to destruct detrimental cancer cell causes significantly less collateral damage to healthy tissues than using electron beams or electromagnetic waves[64–66]. In 1954, the first patient was treated by proton therapy in Lawrence Berkeley Laboratory, and thousands of patients have been treated in various research laboratories until 1990, when the world's first hospital-based proton therapy center was built at the Loma Linda University Medical Center in California[67].

Until now, there are totally 43 particle therapy facilities in operation, having treated nearly a hundred thousand patients, as shown in Table 1.1 [68]. Table 1.1 also shows that until now, mainly traditional cyclotrons and synchrotrons accelerators (denoted as C and S in the fourth column) are used to produce monoenergetic proton or carbon ion beams (denoted as p and C-ion in the third column).

Recently, laser proton accelerators are considered attractive alternatives to the traditional accelerators since the acceleration gradient can reach as high as tens of GeV per centimeter, much greater than traditional accelerators, allowing a significant reduction in costs and system sizes [69–71]. A general concern about particle therapy with laser accelerated protons beam is whether the quality of the protons is monoenergetic enough to suppress unwanted collateral damage. In order to study the interaction between the laser-accelerated proton beams and the human tissues, we use Stopping and Range of Ions in Matter (SRIM) to simulate the energy deposition of the proton beams generated from PIC simulation with a thick layer of water particles, the majority material of human tissues. The energy deposition as a function of depth when inputting the monoenergetic proton beams into water forms a shape of sharp peak called Bragg peak. By observing the Bragg peak with a variety of proton profiles, we can understand the dependence of the proton penetrating depth to the input proton energy and how the energy spread affects the width of the Bragg peak. We observed that the proton energy spectra obtained by laser acceleration of C-H foils can significantly reduce the width of Bragg peak compared to the results using pure hydrogen foils, allowing us to aim on the depth more accurately.

There are still other applications using laser acceleration of ions such as fast ignitions [72,73] and proton imaging [74,75]. Our study about laser acceleration of protons gives a theoretical understanding to the acceleration mechanisms, provides some perceptions in approaching an optimal scheme, and could help to revolutionize the particle acceleration technology with a wide variety of applications.

1.5. Structure of the Thesis

The structure of this thesis is as follows. Chapter 2 describes the background acceleration schemes used contemporarily to accelerate electrons and ions. In particular, the theoretical acceleration model and its prediction in RPA is discussed in detail since it is the principal scheme applied in several following chapters.

Chapter 3 compares the simulation results of RPA with the theoretical calculation. The scaling of obtainable quasi-monoenergetic proton energy with respect to the input laser amplitude is also studied. The growth rate of RTI and how it affect the acceleration time are also discussed.

Chapter 4 describes the acceleration scheme combining RPA and Coulomb repulsion by utilizing a multi-species foil and how it can largely increase the proton energy with quasi-monoenergetic property. The scaling with varying the concentration of these two ion species is also studied.

Chapter 5 further provides a polarization switching scheme based on the acceleration scheme described in Chapter 4 to further accelerate the proton without increasing the input laser power. The scaling of different polarization switch times is

also presented, suggesting that there exists an optimal switching time to maximize the obtainable proton energy.

In Chapter 6, a realistic laser profile is applied in the simulation and verifies that the acceleration scheme described above is also valid using a short laser pulse. Different spot sizes with fixed pulse power and duration are also studied to acquire an optimal spot size to maximize the energy flus.

In Chapter 7, we discuss the medical implication of such accelerated protons. Since the energy requirement of medical use falls on the range of 50-250 MeV, the proton energy obtained in our scheme could be suitable for medical use. Energy dosages with different beam energies are also studied to determine the relationship between the penetration depth and the particle energy.

Chapter 8 gives the summary of this thesis.

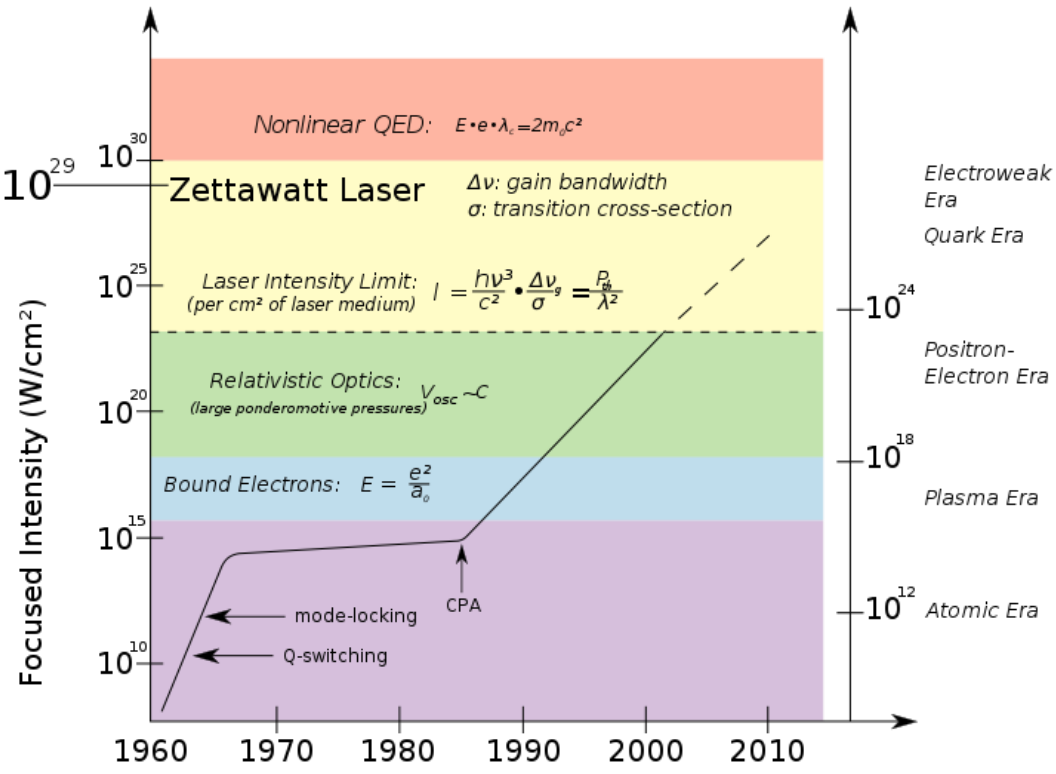

Figure 1.1: Laser intensities achieved in the past 50 years. Courtesy of Wikipedia (*http://upload.wikimedia.org/wikipedia/commons/6/6c/History_of_laser_intensity.svg*).

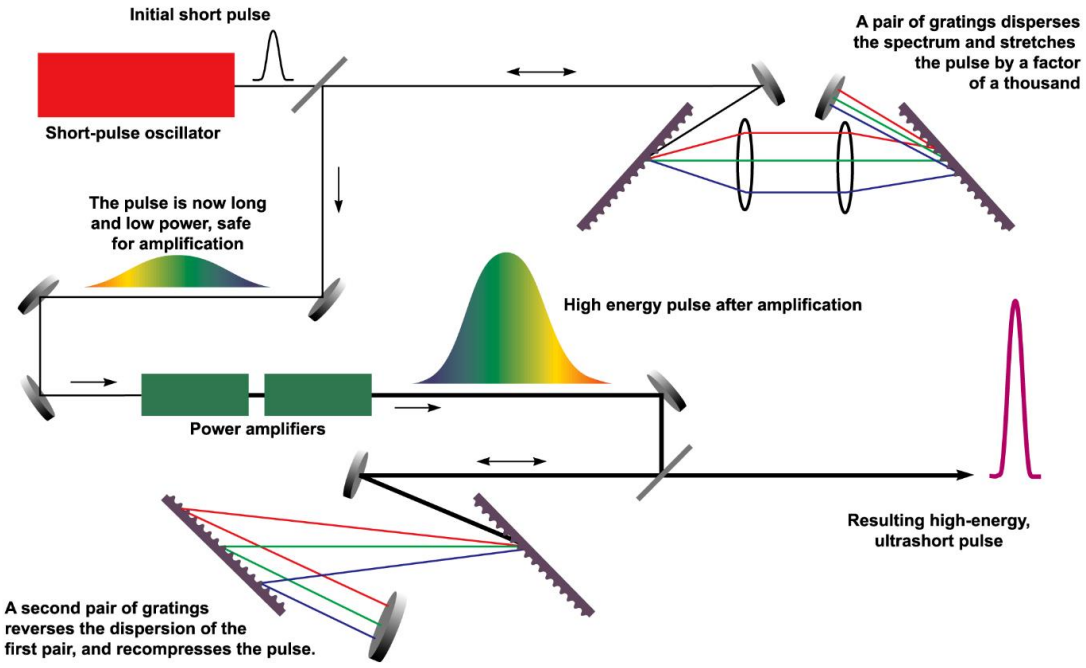

Figure 1.2: Diagrammatic scheme of chirped pulse amplification. Courtesy of Wikipedia (*http://upload.wikimedia.org/wikipedia/en/a/ae/Chirped_pulse_amplification.png*).

Table 1.1: Particle therapy facilities in operation [68].

Facility and Location	Country	Ptcl.	Type & Energy	Beam Direction	Start	Total Patient	Date of Total
ITEP, Moscow	Russia	p	S 250	1 horiz.	1969	4246	10-Dec
St.Petersburg	Russia	p	S 1000	1 horiz.	1975	1386	12-Dec
PSI, Villigen	Switzerland	p	C 250	1 gantry, 1 horiz.	1996	1409	12-Dec
Dubna	Russia	p	C 200	1 horiz.	1999	922	12-Dec
Uppsala	Sweden	p	C 200	1 horiz.	1989	1267	12-Dec
Clatterbridge	England	p	C 62	1 horiz.	1989	2297	12-Dec
Loma Linda	CA.,USA	p	S 250	3 gantry, 1 horiz.	1990	16884	12-Dec
Nice	France	p	C 65	1 horiz.	1991	4692	12-Dec
Orsay	France	p	C 230	1 gantry,2 horiz.	1991	5949	12-Dec
NRF - iThemba Labs	South Africa	p	C 200	1 horiz.	1993	521	11-Dec
IU Health PTC, Bloomington	IN.,USA	p	C 200	2 gantry, 1 horiz.	2004	1688	12-Dec
UCSF	CA.,USA	p	C 60	1 horiz.	1994	1515	12-Dec
HIMAC, Chiba	Japan	C-ion	S 800/u	horiz,vertical.	1994	7331	13-Jan
TRIUMF, Vancouver	Canada	p	C 72	1 horiz.	1995	170	12-Dec
HZB (HMI), Berlin	Germany	p	C 72	1 horiz.	1998	2084	12-Dec
NCC, Kashiwa	Japan	p	C 235	2 gantry	1998	1226	13-Mar
HIBMC,Hyogo	Japan	p	S 230	1 gantry	2001	3198	11-Dec
HIBMC,Hyogo	Japan	C-ion	S 320/u	horiz.,vertical	2002	788	11-Dec
PMRC(2), Tsukuba	Japan	p	S 250	2 gantry	2001	2516	12-Dec
NPTC, MGH Boston	MA.,USA	p	C 235	2 gantry, 1 horiz.	2001	6550	12-Oct
INFN-LNS, Catania	Italy	p	C 60	1 horiz.	2002	293	12-Nov
SCC, Shizuoka Cancer Center	Japan	p	S 235	3 gantry, 1 horiz.	2003	1365	12-Dec
STPTC, Koriyama-City	Japan	p	S 235	2 gantry, 1 horiz.	2008	1812	12-Dec
WPTC, Zibo	China	p	C 230	2 gantry, 1 horiz.	2004	1078	12-Dec
MD Anderson Cancer Center, Houston	TX.,USA	p	S 250	3 gantry, 1 horiz.	2006	3909	12-Dec
UFPTI, Jacksonville	FL.,USA	p	C 230	3 gantry, 1 horiz.	2006	4272	12-Dec
NCC, IIsan	South Korea	p	C 230	2 gantry, 1 horiz.	2007	1041	12-Dec
RPTC, Munich	Germany	p	C 250	4 gantry, 1 horiz.	2009	1377	12-Dec
ProCure PTC, Oklahoma City	OK.,USA	p	C 230	1 gantry, 1 horiz, 2 horiz/60 deg.	2009	1045	12-Dec
HIT, Heidelberg	Germany	p	S 250	2 horiz.	2009	252	12-Dec
HIT, Heidelberg	Germany	C-ion	S 430/u	2 horiz.	2009	980	12-Dec
UPenn, Philadelphia	PA.,USA	p	C 230	4 gantry, 1 horiz.	2010	1100	12-Dec
GHMC, Gunma	Japan	C-ion	S 400/u	3 horiz., vertical	2010	537	12-Dec
IMP-CAS, Lanzhou	China	C-ion	S 400/u	1 horiz.	2006	194	12-Dec
CDH Proton Center, Warrenville	IL.,USA	p	C 230	1 gantry, 1 horiz, 2 horiz/60 deg.	2010	840	12-Dec
HUPTI, Hampton	VA., USA	p	C 230	4 gantry, 1 horiz.	2010	489	12-Dec
IFJ PAN, Krakow	Poland	p	C 60	1 horiz.	2011	15	12-Dec
Medipolis Medical Research Institute, Ibusuki	Japan	p	S 250	3 gantry	2011	490	12-Dec
CNAO, Pavia	Italy	p	S 250	3 horiz./1 vertical	2011	58	13-Mar
CNAO, Pavia	Italy	C-ion	S 400/u	3 horiz./1 vertical	2012	22	13-Mar
ProCure Proton Therapy Center, Somerset	NJ., USA	p	C 230	4 gantry	2012	137	12-Dec
PTC Czech r.s.o., Prague	Czech Republic	p	C 230	3 gantry,1 horiz.	2012	1	12-Dec
SCCA, Proton Therapy, a ProCure Center, Seattle	WA., USA	p	C 230	4 gantry	2013	1	13-Mar

Chapter 2

Laser Particle Acceleration Schemes

In this chapter, we would like to briefly introduce some laser particle acceleration schemes that are commonly used in recent decades. These schemes are proven by experiments to successfully accelerate particles to energies of MeV or even GeV levels. The acceleration schemes to accelerate electrons and ions are completely different and are introduced separately in different subchapters below. In particular, we will emphasize more on laser acceleration of ions and discuss them in detail in the following chapters.

2.1. Laser Electron Acceleration

As described in Chapter 1.2, The laser-electron accelerator was first proposed in 1979 by Tsuyoshi Tajima and John M. Dawson[17]. In their paper, the schemes of LWFA and LBWA with electric fields of the order of tens of gigavolts per centimeter and short pulse duration. It is significantly greater than the electric fields created in conventional accelerators, which are in the order of megavolts per meter and are limited by the breakdown of the media materials.

In a laser-electron accelerator, high amplitude plasma density waves are excited by impinging a laser pulse into a plasma medium and transform the electromagnetic energy of the laser pulse into kinetic energy of accelerated electrons. The intense laser pulse repels the electrons out of its path through the ponderomotive force. The ions, in contrary, are almost stationary due to their heavy mass and therefore are left unshielded,

creating a positively charged region behind the laser pulse. The electrostatic force then pulls the electron back to the center axis, forming an electron density peak. The structure of alternating positive and negative charges continues nearly periodically within a short range and is referred to as a laser wake. The plasma wave is highly relativistic with phase velocity $v_{\mathrm{ph}} = (1 - \omega_{\mathrm{pe}}^2 / \omega_{\mathrm{photon}}^2)c$ close to the speed of light c and oscillates at the electron plasma frequency ω_{pe}, which scales as the square root of the plasma density n_{e} as shown in the relationship

$$\omega_{\mathrm{pe}} = \sqrt{\frac{n_{\mathrm{e}} e^2}{\varepsilon_0 m_{\mathrm{e}}}}, \tag{2.1}$$

where ε_0 is the vacuum permittivity, ω_{photon} is the photon frequency, and e and m_{e} are the charge and mass of an electron[17].

The mechanism repelling the electrons is the ponderomotive force, which is a nonlinear force that a charged particle experiences in an inhomogeneous oscillating electromagnetic field. Considering an electron under the influence of an electromagnetic field, the momentum equation can be expressed as

$$\frac{\mathrm{d}\mathbf{p}}{\mathrm{d}t} = -e(\mathbf{E} + \mathbf{v} \times \mathbf{B}), \tag{2.2}$$

where $\mathbf{p}$ is the momentum, $\mathbf{E} = -\partial \mathbf{A} / \partial t$ and $\mathbf{B} = \nabla \times \mathbf{A}$ are the electric and magnetic field of the laser, $\mathbf{A} = A\mathbf{e}_{\perp}$ is the vector potential and $\mathbf{e}_{\perp}$ is a unit vector in transverse direction. We can then separate the electron momentum into $\mathbf{p} = \mathbf{p}_{\mathrm{q}} + \delta\mathbf{p}$, where $\mathbf{p}_{\mathrm{q}}$ is the quiver momentum and $\delta\mathbf{p}$ is the slow varying response. In non-relativistic limit $|\mathbf{v}| << c$, or equivalently $a \equiv eA / m_{\mathrm{e}} c << 1$ in normalized unit, we then have

$$\frac{\partial \mathbf{p}_{\mathrm{q}}}{\partial t} = -e\mathbf{E} \Rightarrow \mathbf{v}_{\mathrm{q}} = \frac{\mathbf{p}_{\mathrm{q}}}{m_{\mathrm{e}}} = -\frac{e\mathbf{E}}{m_{\mathrm{e}}\omega} = \frac{e\mathbf{A}}{m_{\mathrm{e}}}, \tag{2.3}$$

and

$$\begin{aligned} \frac{\mathrm{d}\delta\mathbf{p}}{\mathrm{d}t} &= \frac{\mathrm{d}\mathbf{p}}{\mathrm{d}t} - \frac{\mathrm{d}\mathbf{p}_{\mathrm{q}}}{\mathrm{d}t} = -e\mathbf{v}_{\mathrm{q}} \times (\nabla \times \mathbf{A}) - (\mathbf{v}_{\mathrm{q}} \cdot \nabla)\mathbf{p}_{\mathrm{q}} \\ &= -e\frac{e\mathbf{A}}{m_{\mathrm{e}}} \times \nabla A \times \mathbf{e}_{\perp} - (\frac{e\mathbf{A}}{m_{\mathrm{e}}} \cdot \nabla)e\mathbf{A} \\ &= -\frac{eA}{m_{\mathrm{e}}}\nabla Ae = -\frac{e^2}{m_{\mathrm{e}}}\nabla\frac{A^2}{2} = -m_{\mathrm{e}}c^2\nabla\frac{a^2}{2} \end{aligned} . \tag{2.4}$$

The time average of the last term is then called the ponderomotive force $\mathbf{F}_{\mathrm{p}} = -m_{\mathrm{e}}c^2\nabla < a^2/2 > \propto \nabla I$, where I is the laser intensity. Under the condition of a strong field, the relativistic correction should be considered and the ponderomotive force then can be expressed as [76]

$$\begin{aligned} \mathbf{F}_{\mathrm{p}} &= -\frac{m_{\mathrm{e}}c^2}{< \gamma >}\nabla\frac{< a^2 >}{2} \\ < \gamma > &= \sqrt{1 + \left(\frac{< p >}{m_{\mathrm{e}}c}\right)^2 + < a^2 >} \end{aligned} . \tag{2.5}$$

It was shown [24,77–79] that after the plasma waves are created by the ponderomotive force of the laser pulse, the electrons can then surf on the laser wake and be accelerated with acceleration gradient reaching

$$\frac{E_{\mathrm{S}}}{E_0} = \frac{a_0^2}{\sqrt{1 + a_0^2}} \approx \begin{cases} a_0^2, & a_0 << 1 \\ a_0, & a_0 >> 1 \end{cases} \tag{2.6}$$

as an optimal case while the length of the electromagnetic wave package L_{L} is half the wavelength of the plasma waves in the wake,

$$L_{\mathrm{L}} = \frac{\pi c}{\omega_{\mathrm{pe}}} = \frac{\lambda_{\mathrm{pe}}}{2}, \tag{2.7}$$

where E_{S} is the optimal longitudinal electric field that electron can surf on, $E_0 = m_{\mathrm{e}}\omega_{\mathrm{L}}c/e$ is a normalization factor of electric field, $a_0 = E_{\mathrm{L}}/E_0$ is the normalized peak amplitude of the input laser beam, and $\lambda_{\mathrm{pe}} = 2\pi c/\omega_{\mathrm{pe}}$ is the plasma wavelength. With typical plasma density of $n_{\mathrm{e}} = 10^{16}\text{-}10^{18}\,\mathrm{cm}^{-3}$, the acceleration gradient can reach $E_{\mathrm{L}} = 10^{8}\text{-}10^{9}\,\mathrm{V/cm}$, about three orders of magnitude greater than the conventional RF accelerators. That is, to reach the same particle energy, plasma accelerators can then, in principle, be three orders of magnitude shorter than their conventional counterparts.

The optimal condition shown in Equation (2.7) can be reached in a couple of different ways [80]. In LWFA, a short laser pulse with pulse length L_{L} is used to excite the wakefield. In LBWA, two long laser pulses with slightly different frequencies ω_1 and ω_2 are superposed to form a laser beam with beat frequency $\omega_{\mathrm{beat}} = |\omega_1 - \omega_2| = \omega_{\mathrm{pe}}$. In SMLWFA, the laser pulse modulates itself into a beat-wave like structure by stimulated Raman forward scattering instability.

2.2. Laser Ion Acceleration

Besides laser acceleration of electrons, the possibility of utilizing laser to accelerate ion attract lots of interests as well. However, accelerating a particle with about 2000 times in mass in obviously more difficult and requires larger laser intensity. As described in the previous section, the ions in the laser wakefield acceleration scheme

are nearly stationary due to the heavy masses, and as a consequence we must search for alternative schemes to accelerate ions. The most significant difference between the acceleration schemes of electrons and ions is the target density. Since the ions is almost immobile during the electron plasma oscillation period, instead of oscillating electrons transversely, we attempt to remove the electrons entirely from the target longitudinally by using overdense plasma targets. Depending on different laser and target profiles, the acceleration schemes can be classified differently such as TNSA, RPA, SCR, etc.

2.2.1. Target Normal Sheath Acceleration

Several experiments in 2000 showed that energetic ion bunches from both front and rear side of the targets were observed in laser-plasma interaction [50,81,82]. In 2001, Wilks *et al.* provided an analytic model to explain such ion acceleration mechanism based on Denavit's derivation [25,83]. The cartoon in Figure 2.1 shows their explanation in the original paper. When the laser pulse is impinged onto an overdense target with thickness in the order of 100 wavelength, the laser energy is partially absorbed and transferred into kinetic energy of the plasma electrons, which are accelerated into the target. Those energetic electrons pushed by the laser ponderomotive force then penetrate the target, reach the rear side and form a cloud of hot electrons. The electric force accelerating the ions to move forward due to these hot electrons could be evaluated as [25,31]

$$m_{\mathrm{i}} \frac{\mathrm{d}v_{\mathrm{i}}}{\mathrm{d}t} = eE_{\mathrm{S}} = \frac{k_{\mathrm{B}}T_{\mathrm{e}}}{L_{\mathrm{n}}}, \tag{2.8}$$

where $L_n = c_s t$ is the scale length of ion density, k_B is Boltzmann constant, m_i is the ion mass, $c_s = \sqrt{Z_i k_B T_e / m_i}$ is the ion acoustic velocity and Z_i is the charge ratio of an ion to the elementary charge. The electron temperature $T_e = (\gamma - 1) m_e c^2$ can be estimated by considering a simplified case of placing a single electron under the influence of an oscillating electric field with frequency ω_L as

$$\frac{\mathrm{d}(\gamma m_e v)}{\mathrm{d}t} = eE_L \Rightarrow \omega_L \gamma m_e \sqrt{1 - \frac{1}{\gamma^2}} = \omega_L m_e \sqrt{\gamma^2 - 1} = a m_e \omega_L c \,, \tag{2.9}$$

or simply $< \gamma > \approx \sqrt{1 + a_0^2 / 2}$ after taking the time average, which shows that the electron temperature scales linearly with a_0 for large laser amplitude $a_0 >> 1$. This model successfully explained the forward and backward acceleration of ion due to different scale length, but also revealed that the acceleration is due to thermal motion of electrons, indicating broad ion energy spectra and nearly spherical ion expansion.

There are several experiments on laser acceleration of ions studying the maximum proton energy obtainable by TNSA, and they all reported board energy spectra [50,84,85]. It was reported in 2011 that a proton beam with cutoff energy 67 MeV was obtained using a laser beam with intensity 10^{20} W/cm^2 and energy 80 J [86].

2.2.2. Radiation Pressure Acceleration

In order to obtain a monoenergetic proton beam, an acceleration scheme depending on electron thermal motion like TNSA does not appear to be an effective approach. Therefore, a direct push from laser energy to particle energy by radiation pressure is then a natural alternative and is widely studied [36–48], and RPA was shown

to be an relatively efficient way in obtaining quasi-monoenergetic ion beams. In RPA, a laser pulse pushes the entire electron layer forward and separates it from the ion layer. The electrostatic force due to the charge separation then pull the ions forward along with the electron layer. The process is shown as a series of cartoons in Figure 2.2. In an accelerating frame moving with the double layer structure, the electrons are balanced by the radiation pressure and the Coulomb attractive force, whereas the ions are balanced by the Coulomb force and the inertial force. The double-layer structure can therefore be accelerated stably with quasi-monoenergetic property. The balance of these two opposing forces forms a trap for the ions in real and phase spaces. These stably trapped ion and electron layers form a self-organized double layer in one dimension, accelerated as a whole by the laser radiation pressure, and the ions thus accelerated are nearly monoenergetic. There are a couple of requirements to be satisfied in RPA, and some of them are relatively challenging in experiments. To reduce the thermal effect of electrons, a circularly polarized laser instead of a linearly polarized one should be applied to eliminate the oscillating components of the ponderomotive force as shown in Equation (2.4) [37]. To prevent the ultra-thin target be blown out by the pre-pulse, the contrast ratio of the laser is required to be extremely small (less than 10^{-9}). It was shown by experiments that a laser pulse with a pre-pulse arriving 11 ps before the main pulse with contrast ratio 5×10^{-8} can deteriorate the quality of the proton beam significantly due to amplified spontaneous emission [87,88]. To increase the efficiency of acceleration, the target foils are made ultra-thin. The optimal thickness of radiation acceleration can be calculated by a simple force balance condition, where the electrostatic force is balanced by the radiation pressure force. In the following

paragraph, we first derive the form of radiation pressure, solve the equation of motion to obtain energy scaling, and finally calculate the optimal thickness condition.

To estimate the acceleration or RPA, we started from the expression of radiation pressure P_{R}, which can be expressed in the moving frame as

$$P_{\mathrm{R}} = (1+|R|^2)\frac{<I_{\mathrm{L}}>}{c}, \tag{2.10}$$

where $|R|^2$ is the reflectivity and $<I_{\mathrm{L}}>$ is the time-average of the intensity of the incident laser beam. The radiation pressure pushes the foil, providing kinetic energy per time per area being

$$\frac{1}{A}\frac{\mathrm{d}\varepsilon_{\mathrm{i}}}{\mathrm{d}t'} = P_{\mathrm{R}} v_{\mathrm{i}}, \tag{2.11}$$

where v_{i} is the foil velocity and t' is the time in the moving frame. By energy conservation, the incident power is equal to the energy increase of the foil per time plus the reflected power

$$<I_{\mathrm{L}}>=<I_{\mathrm{L}}>|R|^2 + P_{\mathrm{R}} v_{\mathrm{i}}. \tag{2.12}$$

Combine Equations (2.10) and (2.12), we have

$$P_{\mathrm{R}} v_{\mathrm{i}} = <I_{\mathrm{L}}> - <I_{\mathrm{L}}>\left(\frac{P_{\mathrm{R}} c}{<I_{\mathrm{L}}>} - 1\right) = 2<I_{\mathrm{L}}> - P_{\mathrm{R}} c, \tag{2.13}$$

or

$$P_{\mathrm{R}} = \frac{2<I_{\mathrm{L}}>}{v_{\mathrm{i}} + c} = \frac{2<I_{\mathrm{L}}>/c}{1+\beta_{\mathrm{i}}}, \tag{2.14}$$

where $\beta_i = v_i / c$ is the normalize foil velocity. Returning to the lab frame, where the intensity of the incident beam is increased due to a compression in the pulse, which can be expressed as

$$dt' = \frac{dt}{1-\beta_i} \tag{2.15}$$

and thus the expression for the radiation in the lab frame is

$$P_R = \frac{2 < I_L >}{c} \frac{1-\beta_i}{1+\beta_i}. \tag{2.16}$$

Therefore, the equation of motion can be written down as

$$\frac{d\gamma_i \beta_i c}{dt} = \frac{P_R A}{m_i n_0 A l_0} = \frac{2 < I_L >}{m_i n_0 l_0 c} \frac{1-\beta_i}{1+\beta_i}, \tag{2.17}$$

where $\gamma_i = (1-\beta_i^2)^{-1/2}$ is the relativity factor and $m_i n_0 A l_0$ is the total mass of the foil. The equation above can be normalized by dimensionless units by introducing normalized electric field amplitude

$$a_0 = \frac{eE_L}{m_e \omega_L c}, \tag{2.18}$$

and noticing that the average intensity of a circularly polarized wave can be expressed as

$$< I_L >= \varepsilon_0 E_L^2 c = \varepsilon_0 \frac{m_e^2 \omega_L^2 c^3}{e^2} a_0^2. \tag{2.19}$$

Substitute Equation (2.19) into Equation (2.17), we then obtain

$$\frac{d\gamma_i \beta_i}{d(t/T_L)} = \frac{2a_0^2 T_L \varepsilon_0 m_e^2 \omega_L^2 c^2}{e^2 m_i n_0 l_0 c} \frac{1-\beta_i}{1+\beta_i} = 2a_0^2 \frac{m_e}{m_i} \frac{\lambda_L}{l_0} \frac{n_{cr}}{n_0} \frac{1-\beta_i}{1+\beta_i}, \tag{2.20}$$

where $n_{cr} = \varepsilon_0 m_e \omega_L^2 / e^2$ is the electron critical density. Let $S_0 = 2a_0^2 \frac{m_e}{m_i} \frac{\lambda_L}{l_0} \frac{n_{cr}}{n_0}$ be the normalized acceleration coefficient, $\tau = t / T_L$ be the normalized time and $u_i = \gamma_i \beta_i$ be the normalized relativistic velocity, the equation of motion can be further simplified as

$$\frac{\mathrm{d}u_i}{\mathrm{d}\tau} = S_0 \frac{\sqrt{u_i^2 + 1} - u_i}{\sqrt{u_i^2 + 1} + u_i}. \tag{2.21}$$

The equation of motion is analytically solvable with several steps [36,40,41]. First of all, making substitution with $u_i = \frac{1}{2}\left(\psi - \frac{1}{\psi}\right)$, we have $\sqrt{u_i^2 + 1} = \frac{1}{2}\left(\psi + \frac{1}{\psi}\right)$ and $\frac{\mathrm{d}u_i}{\mathrm{d}\tau} = \frac{d\psi}{d\tau}\frac{1}{2}\left(1 + \frac{1}{\psi^2}\right)$, therefore

$$\frac{d\psi}{d\tau}\frac{1}{2}\left(1 + \frac{1}{\psi^2}\right) = S_0 \frac{1/\psi}{\psi} \Rightarrow \frac{d\psi}{d\tau} = \frac{2S_0}{\psi^2 + 1}. \tag{2.22}$$

Integrate once, we then obtain

$$\frac{1}{3}\psi^3 + \psi \Big|_1^{\psi} = \frac{1}{3}\psi^3 + \psi - \frac{4}{3} = \int_0^{\tau} 2S_0 d\tau. \tag{2.23}$$

Let again $\psi = 2\sinh\phi$, we have $\psi^3 + 3\psi = 2(4\sinh^3\phi + 3\sinh\phi) = 2\sinh 3\phi$, therefore

$$\sinh 3\phi = \int_0^{\tau} 3S_0 d\tau + 2. \tag{2.24}$$

The final equation of motion can then be expressed in term of ψ as

$$\psi(\tau) = 2\sinh\left[\frac{1}{3}\sinh^{-1}\left(6\frac{m_e}{m_i}\frac{\lambda_L}{l_0}\frac{n_{cr}}{n_0}\int_0^\tau a_0^2 d\tau + 2\right)\right]. \tag{2.25}$$

As mentioned above, the optimal thickness for obtaining maximum acceleration can be calculated by force balance condition. Using the normalized radiation pressure expression in Equations (2.16) and (2.19) with initial stationary condition $\beta_i = 0$, we have

$$P_R = \frac{2 < I_L >}{c} = 2\varepsilon_0 \frac{m_e^2 \omega_L^2 c^2}{e^2} a_0^2 = n_0 l_0 e \frac{n_0 l_0 e}{2\varepsilon_0}. \tag{2.26}$$

Using again $n_{cr} = \varepsilon_0 m_e \omega_L^2 / e^2$ and $c = \lambda_L \omega_L / 2\pi$, we obtain

$$\frac{a_0}{\pi} = \frac{n_0}{n_{cr}}\frac{l_0}{\lambda_L}, \tag{2.27}$$

which is the theoretical optimal thickness condition in dimensionless units. This describes a very simple relationship between the laser amplitude, target density and thickness to maximize the efficiency. Moreover, to minimize the wave tunneling through the target, $l_0 > c/\omega_{pe}$ or equivalently $2a_0\omega_L/\omega_{pe} > 1$ should be satisfied as well.

The evolution of the ion kinetic energy is then

$$\varepsilon_{quasi\text{-}mono} = \frac{(\psi - 1)^2}{2\psi} m_i c^2. \tag{2.28}$$

Figure 2.3 shows the kinetic energy evolution of a hydrogen foil by RPA with optimal thickness using a laser beam of normalized amplitude $a_0 = 5$, corresponding to a laser intensity of $10^{20}\,\mathrm{W/cm^2}$ with wavelength λ_L = 0.8 μm, a typical value of Titanium-

sapphire type laser. By further applying the optimal thickness condition, Eq. (2.27), we have

$$\varepsilon_{\text{non-rel}} \approx 2(\pi a_0 \frac{m_e}{m_i} \frac{t}{T_L})^2 m_i c^2 \tag{2.29}$$

for $\pi a_0 t_s / T_L << m_i / m_e$, a classical limit with energy scales as t^2 and

$$\varepsilon_{\text{ultra-rel}} \approx (\frac{3}{2}\pi a_0 \frac{m_e}{m_i} \frac{t}{T_L})^{1/3} m_i c^2 \tag{2.30}$$

for $\pi a_0 t_s / T_L >> m_i / m_e$,an ultra-relativistic limit with energy scales as $t^{1/3}$, consistent with the results derived from previous works [36,40,41,55].

Due to a strict requirement on laser profile, the experiments of RPA are not conducted until recent years[49,62,89–91]. In 2009, Using a 30 TW laser with a peak intensity of $5\times10^{19}\,\text{W/cm}^2$ irradiated on a diamond-like carbon (DLC) foil of thickness 5.3 nm, Henig *et al.* obtained a C^{6+} ion beam with a distinct peak energy of around 30 MeV and an energy spread of around 20 MeV by both 2D simulations and experiments and first demonstrated experimentally that a circularly polarized laser beam is more effective in obtaining monoenergetic ion beams[49], and similar results are obtained by other experiments as well.

2.2.3. Improvement

Although the RPA scheme can apparently push the foil quasi-monoenergetically with great efficiency, there is one fundamental defect limiting the quality of the ion beam. Since the foil is so thin, the laser can penetrate the thin foil and cease to push the electrons soon after being irradiated on the foil. The main factor

causing laser penetration is RTI, which is a well-known effect observed while placing a fluid with large density above one with small density [92,93]. Pegoraro and Bulanov[51] first showed by simulation that the observation of the bubble-like structure on the foil during the process of RPA, a typical sign of RTI. There are now several different approaches to extend the acceleration time. One is using multi-species or multi-layer foils, where the repulsion force between different ion species is used to further accelerate the proton after electrons becoming transparent[47,54,56,57,94]. The examination of RTI and this scheme will be discussed in depth in the following chapters, and we will show that this scheme can significantly increase the particle energy while retaining the quasi-monoenergetic property. Another approach which is widely studied is to tailor the foil density profile and make use of shock acceleration [35,46,95–98], where a plasma mirror accelerated by RPA pushes the particles in front of it further ahead with an initially decreasing density profile. In particular, although with few particle number, Haberberger *et al.* successfully obtained a proton beam of energy 20 MeV with only 1% energy spread using shock acceleration induced by a laser pulse train of peak power 4 TW[95]. There are still other approaches using foil shaping, density profile modulation, multi-pulses to reduce the effect of RTI [53,99–101] as well, indicating that laser acceleration of quasi-monoenergetic ions is an attractive and promising alternative to traditional acceleration techniques.

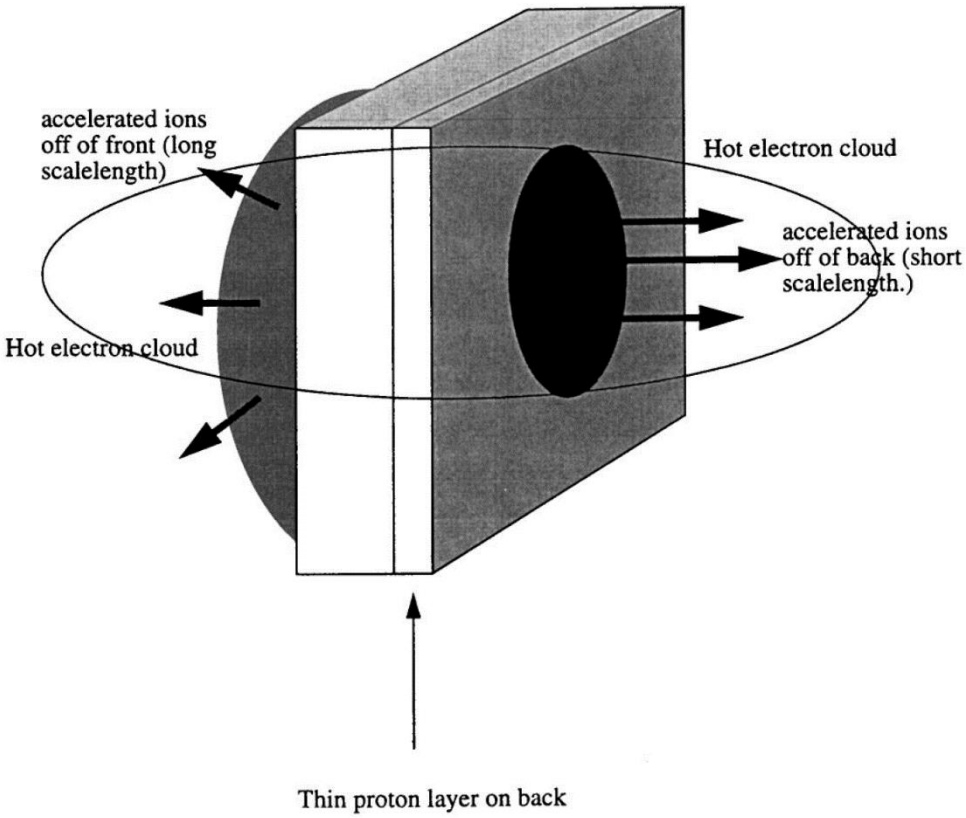

Figure 2.1: The mechanism of TNSA in Wilks *et al.*'s paper.

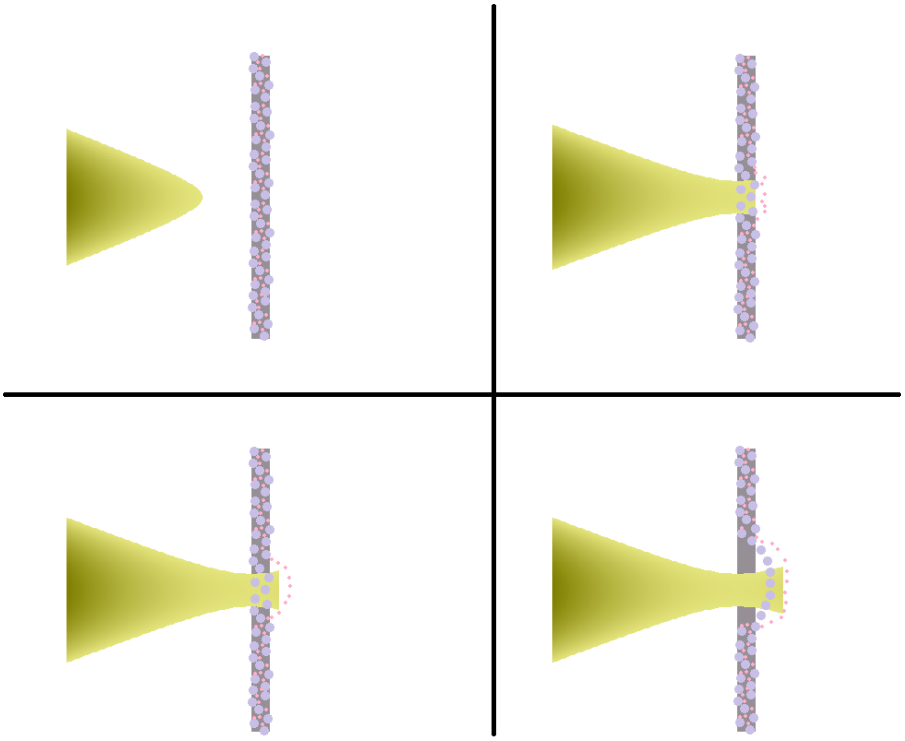

Figure 2.2: A cartoon showing the process of radiation pressure acceleration. The laser beam is shown in yellow, electrons in pink and protons in purple.

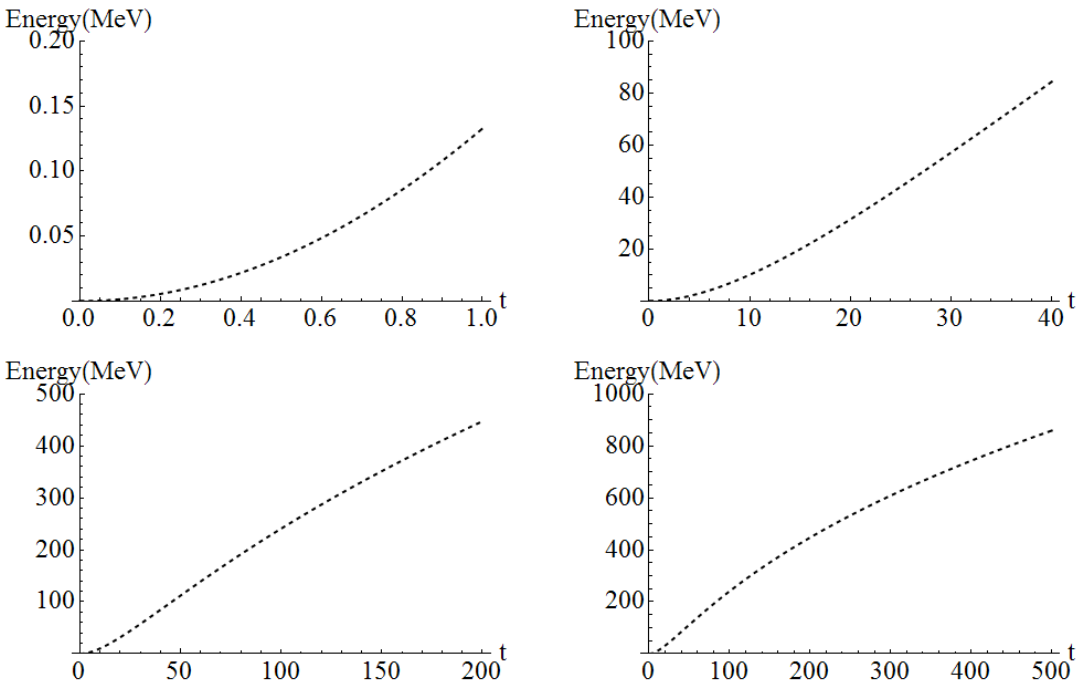

Figure 2.3: Kinetic energy evolution of a hydrogen foil with laser amplitude $a_0 = 5$ and optimal thickness at different time ranges.

Chapter 3

Laser Acceleration of Ions Using Single-Species Thin Foils – Radiation Pressure Acceleration and Rayleigh Taylor Instability

Radiation pressure acceleration was actively studied recently since it can accelerate almost all the target foil as a whole with quasi-monoenergetic property in the ion energy spectrum, indicating a significantly better energy conversion efficiency. However, the system is also more difficult to build due to a higher requirement on the laser and the foil. That is, high intensity circularly polarized lasers with high contrast ratio and ultra-thin foils are necessary in this scheme. This setting is utilized as a main framework through the thesis; further improvements and modifications based on this scheme will be discussed in the following chapters. In this chapter, we discuss the acceleration mechanism, present the simulation results of RPA, and deliberate the advantages and limitations (especially the Rayleigh-Taylor instability) of this mechanism.

3.1. Introductions

Recently, RPA was considered an efficient way of accelerating quasi-monoenergetic ions [37–42,54,55,102], where a self-organized double layer plasma is accelerated by reflecting the laser. In comparison to the conventional TNSA-scheme [27], the conversion efficiency with the RPA scheme is estimated to be more than 40 times higher. In this paper, we address factors limiting the energy of RPA accelerated ions and the energy scaling of quasi-monoenergetic ions as a function of the laser power.

Both questions are important for theoretical understanding, experimental planning and future applications.

In 1D RPA theory as shown in Chapter 2.2.2, the foil could be unlimitedly accelerated as long as being impinged by the laser. However, not all of the particle can be fully accelerated. There will be a fraction of the ions un-trapped and being left behind the accelerated foil. The space-charge electric field between these ions and the electrons keeps the rest of the ions trapped in the foil. Through a balance between the electric force and the inertial force in the accelerated frame, the fraction of un-trapped ions can be estimated as [42] $N_{\text{untrapped}} / N_0 = 2\varepsilon_0 I_0 / N_0^2 e^2 c$, where $N_0 = n_{i0} l_0$ is the total surface number density of ions. Moreover, the time for monoenergetic ion acceleration with RPA is limited by the duration in which the double layer can maintain its overdense properties, which can be lost due to the development of the Rayleigh-Taylor instability (RTI) [51,54,55,102], which is one of the most important instabilities arising when a thin plasma foil is accelerated by the radiation pressure of an intense laser. It poses a limit on the time a foil can be accelerated before it loses its monoenergetic properties.

3.2. Simulation and Observation

The acceleration process could be analyzed numerically by particle-in-cell (PIC) simulations, where many macro-particles are coordinated on finely discretized space domain so that we can calculate the field and particle data at each individual grid and reconstruct the distribution. There are two different PIC tools we used in simulating the acceleration process throughout the thesis: OOPIC Pro [103], a two dimensional (2D)

PIC code, and its next-generation product VORPAL [104], a PIC code capable of handling 1D, 2D and 3D geometry. Here we employ 2D PIC simulations to demonstrate the generation and energy scaling of quasi-monoenergetic ions by the RPA with laser radiation intensity. The simulation domain is $-4 \le x/\lambda_{\mathrm{L}} \le 12$; $-12 \le y/\lambda_{\mathrm{L}} \le 12$ and is divided into 64 grids per wavelength. The boundary condition is periodic in y direction and out flow in x direction. The foil is initially located at $0 \le x \le l_0$ with $l_0 = 0.2\lambda_{\mathrm{L}}$ being the foil thickness and is resolved by about 10^6 quasi-particles of each species (protons and electrons). The time step is $0.0027T_{\mathrm{L}}$, which is four times finer than the Courant–Friedrichs–Lewy condition, to avoid inaccuracy from simulation approximation and ensure that the results are a consequence of real physics, where $T_{\mathrm{L}} = 3.33\mathrm{fs}$ is the laser period, corresponding to $\lambda_{\mathrm{L}} = 1\mu\mathrm{m}$. The amplitude of the incident circularly polarized laser has a Gaussian profile in the transverse direction with the spot size being $16\lambda_{\mathrm{L}}$ in diameter and a trapezoidal time profile with $3T_{\mathrm{L}}$ rising, $24T_{\mathrm{L}}$ flat, and $3T_{\mathrm{L}}$ falling time, respectively.

Figure 3.1 shows 2D PIC simulation results of the RPA of a thin foil with a normalized incident laser amplitude $a_0 = 25$, initial foil density $n_{\mathrm{e0}} = 41.7n_{\mathrm{cr}}$ and foil thickness $l_0 = 0.2\lambda_{\mathrm{L}}$ corresponding to the optimal thickness as defined in Eq. (2.27). It shows that the RTI can destroy the electron layer and widen the energy spectrum of the ions. For effective acceleration and production of monoenergetic particles, it is important to maintain the target density as over-dense, i.e. $n_{\mathrm{e}} \ge \gamma_{\mathrm{e}} n_{\mathrm{cr}}$, where $\gamma_{\mathrm{e}} = (1 - v_{\mathrm{e}}^2/c^2)^{-1/2}$ provides the relativistic correction and $n_{\mathrm{cr}} = \varepsilon_0 m_{\mathrm{e}} \omega_{\mathrm{L}}^2 / e^2$ is the

non-relativistic critical density. For the electron layer driven by laser light, γ_e within the laser penetration depth will be approximately equal to a_0 for $a_0 >> 1$ so the relativistic critical density can be approximated as $n_{cr} a_0$. During the linear phase of the RTI, small perturbations, or ripples, on the surface of the foil grow exponentially. These perturbations will grow into large amplitude periodic structures and form interleaving high density blobs and low density regions for both the electron and ion layers, as shown in Figure 3.1. Figure 3.1 also shows that the transverse wavelength of the periodical structure is comparable to the laser wavelength. The density difference between the high and low density regions can grow very rapidly and filaments, or fingerlike structures, can be further developed. Once the density of the low density region of the foil falls below the critical value (evolution shown in the third column in Figure 3.1, the laser light can penetrate that region (the fifth column in Figure 3.1), after which the energy cannot be converted into foil acceleration efficiently, and the particle energy spread will be significantly increased (the sixth column in Figure 3.1) due to laser-induced heating and Coulomb explosion. This leads to a leakage of radiation through the target by self-induced transparency. After this stage, the foil can no longer be accelerated efficiently and the energy spectrum starts to broaden dramatically and thus loses its monoenergetic property.

Figure 3.2(a) shows the general agreements between theory and simulation for the time evolution of the ion momentum p_{ix} averaged over a $0.5\lambda_L \times 2\lambda_L$ window co-moving with the target. The simulation shows slightly higher values of p_{ix} than the 1D theoretical calculation for $10T_L < t < 20T_L$ due to that some ions are being pushed

away from the axis in the transverse direction and the remaining ions within the window are accelerated more efficiently by the radiation pressure. At later stages after $t = 20T_{\mathrm{L}}$, the simulation shows a lower value of p_{ix} than the theoretical calculation due to the RTI-induced transparency. The evolution and broadening of the ion energy spectra within the window can be seen from Figure 3.2(b). Significant broadening of the energy spectra with energy spread ratio ($\Delta E / E_{\mathrm{p}}$) greater than 20%, where ΔE is the full width half maximum energy spread and E_{p} is the average energy of the trapped ions, occurs around $t = 16T_{\mathrm{L}}$. In Figure 3.2(c), the evolution of the normalized average electron density within a $0.05\lambda_{\mathrm{L}} \times 4\lambda_{\mathrm{L}}$ window co-moving with the target (blue line) shows that the radiation pressure initially compresses the electron layer to a state with higher density (greater than 3 times the initial density), and then the RTI starts to broaden the foil and decrease the electron density. After $t = 16T_{\mathrm{L}}$, the normalized average electron density $n_{\mathrm{e}} /(n_{\mathrm{cr}} a_0)$ drops below 1, which indicates that the electron density is below the relativistic critical density, and the foil becomes transparent to the laser light. This can be further inferred from the evolution of the normalized average electron gamma factors ($\gamma_{\mathrm{e}} / a_0$, $\gamma_{\mathrm{e}\|} / a_0$, and $\gamma_{\mathrm{e}\perp} / a_0$) within the window in Figure 3.2(c). During the RPA, as the electron layer density decreases due to the RTI, the laser light penetrates deeper into the electron layer and the transverse kinetic energy of the electrons within the laser penetration depth will become ultra-relativistic so that $\gamma_{\mathrm{e}\perp} \sim a_0$. Therefore, the normalized average electron gamma factor $\gamma_{\mathrm{e}\perp} / a_0$ grows larger as the laser light penetrates deeper and when the laser light fully penetrates the foil, we have $\gamma_{\mathrm{e}\perp} / a_0 \approx 1$ occurring around $t = 16.5T_{\mathrm{L}}$. At a later stage, the electron

parallel velocity continues to grow as shown by $\gamma_{e\|} / a_0$ due to the development of the filamentation instability after the laser penetrating into the underdense plasma. We also note that during the RPA, the ion layer is compressed into a high energy density state as shown in Figure 3.2(d). The energy density of the proton layer can be as high as $u_0 \sim 10^{17}\,\mathrm{J/m^3}$.

To explore the scaling of the maximal obtainable energy of monoenergetic ions as a function of the incident laser power, we defined a quasi-monoenergetic ion beam as having an energy spread ratio $\Delta E / E_p$ below 20%, and performed two sets of 2D PIC simulations, one for the RPA of protons and the other for carbon ions. In the simulations, the foil density is chosen to scale linearly with the normalized incident laser amplitude a_0 so that the foil thickness is fixed to be $l_0 = 0.2\lambda_L$, satisfying the optimal thickness condition described in Eq. (2.27). Figure 3.3 shows the maximal quasi-monoenergetic ion energy vs the incident laser amplitude along with the occurrence time of the maximum energy, t_s. Here the maximal quasi-monoenergetic ion energy is almost proportional to a_0 with a nearly constant t_s / T_L (15.8 ± 1.7 and 12.9 ± 1.4 for protons and carbon ions, respectively).

3.3. Analysis and Discussion

To explain the weak dependence of t_s on laser power in the RPA, we apply the theory of mode growth of the RTI. First, we estimate the required density reduction for the occurrence of underdense condition which can induce the broadening of the proton energy spectrum. In our simulation the foil thickness is fixed to be $l_0 = 0.2\lambda_L$, and thus

the initial density in the target is related to the critical density through $n_{e0} = (a_0/\pi)(\lambda_L/l_0)n_{cr} = 1.6a_0 n_{cr}$. Relativistic underdense condition $\varepsilon = 1 - n_e/(a_0 n_{cr}) > 0$ is met when the density drops to satisfy $n_e < a_0 n_{cr} = n_{e0}/1.6$. Therefore, the density reduction factor for the underdense condition $n_e(t_s)/n_{e0} = 1/1.6$ is a constant independent of a_0 in our simulations.

Figure 3.4(a) and (b) show the simulated transverse distribution of average ion density at three instants for two different laser intensities, indicating the occurrence of mode growth of the RTI. For the higher laser intensity $a_0 = 25$ [Figure 3.4(b)], the ion density develops periodic structures with a periodicity comparable to the laser wavelength, while for $a_0 = 5$ [Figure 3.4(a)], the structures have shorter periodicity. The growth rate of the RTI is proportional to $\sqrt{gk}$ for a mode of characteristic transverse wave number *k*, where *g* is the acceleration. We define the total RTI growth factor as $\alpha = \sqrt{k_s}\int_0^{t_s}\sqrt{g(t)}\mathrm{d}t$ to represent the exponential growth of the density fluctuation amplitude, where $2\pi/k_s$ is the dominant transverse periodic structure scale length appearing just before the broadening of the proton energy spectrum and can be obtained from the simulation. The acceleration $g(t) = \mathrm{d}(\gamma v)/\mathrm{d}t$ can be obtained from Eq. (2.17). This factor α at the saturation time $t = t_s$ for different input laser amplitudes a_0 are calculated from our simulations.

Figure 3.4(c) shows that the dependence of the calculated total growth factor α on the laser amplitude a_0, indicating that the growth factor is nearly independent of

the laser amplitude a_0. To explain this, we can explore the dependence of the contributing factors $\int_0^{t_s}\sqrt{g(t)}\mathrm{d}t$ and k_s to α on a_0. Figure 3.4(d) shows that the factor $\int_0^{t_s}\sqrt{g(t)}\mathrm{d}t$ increases with a_0 but is flattened for large a_0. For $a_0 > 20$, the Doppler effect of the laser radiation as shown in Eq. (2.17) limits the acceleration and consequently determines the weak dependence of the growth factor on laser amplitude. From the dependence of the saturation wave number on a_0 shown in Figure 3.4(d), it can be seen that for a laser amplitude $a_0 < 10$, the transverse periodic structure has a dominant scale length less than λ_L, which is due to that smaller length-scale structures grow faster and the RTI did not yet reach saturation when the induced transparency occurs. For laser amplitudes $a_0 > 20$, the transverse periodic structures have scale lengths approximately equal to λ_L, the saturation length scale for the RTI, a situation already discussed in previous works [51,52]. Combining the opposite dependence of $\int_0^{t_s}\sqrt{g(t)}\mathrm{d}t$ and k_s on a_0, we can explain the growth factor α thus obtained is nearly independent of the laser amplitude a_0.

Therefore, given that both the growth factor α and the density reduction factor for reaching the underdense condition are nearly independent of the laser amplitude a_0, we can therefore explain the weak dependence of the quasi-monoenergetic ion beam development time t_s on the laser amplitude a_0.

The scaling of the quasi-monoenergetic ion energy calculated in Equation (2.25) is shown as dashed lines in Figure 3.3, where $6n_{C0} = n_{p0} = n_{e0}$ and

$m_C = 12m_p = 12 \times 1836 m_e$ are applied, and agrees well with the simulation results for the RPA of both protons and carbon ions. Here t_s is chosen to be $18T_L$ for protons and $14T_L$ for carbon ions, slightly longer than those from the simulations to compensate the loss of ions off the axis during the acceleration in the 2D simulation. Equation (2.28) also shows that, since $n_{C0}m_C = 2n_{p0}m_p$, the acceleration of the carbon foil is half that of the proton foil, indicating that the average energy of carbon ions is then 3 times that of proton ions at the same time since $m_C v_C^2 / 2 = (12m_p)(v_p / 2)^2 = 3m_p v_p^2 / 2$. The scaling suggests that for a flat ultra-thin target of optimal thickness, the quasi-monoenergetic proton and carbon ion energy can reach about 200 MeV and 100 MeV per nucleon, respectively, with $a_0 = 25$, corresponding to around 1 PW laser power. This opens up the possibility of applying RPA-based laser hadron accelerator with sub-petawatt laser for medical applications, fast ignition, and proton imaging methods.

3.4. The Influences of Different Initial Conditions on the Results

The scaling in Figure 3.3 shows that although the development time t_s is independent of input amplitude a_0, the accelerating times for proton and carbon ion cases are slightly different. To investigate the dependence of t_s on different initial conditions and to verify that the mechanism of the RPA is still the same among different input parameters, we compare the evolution results with the cases of a laser beam with plane wave profile in transverse dimension and a thinner foil target.

Figure 3.5 shows the evolution of particles at the same time steps as in Figure 3.1 while we use circularly polarized plane wave instead of Gaussian beam to

illuminate on the foil. The interleaving high and low density regions in transverse dimension indicate that RTI is still the principal instability in destroying the electron layer and broadening the energy spectrum. The time of transparency $t_s = 18T_L$ is longer than the Gaussian beam case by about 1.5 wave periods due to a slower density reducing speed, and the similar average energies with the Gaussian beam case verifies the RPA mechanism and the validity of Eqs. (2.25) and (2.28). Since the spot size of the Gaussian profile is large compared to the foil thickness and the laser wavelength, the foil development in the center part does not differ from the plane wave case considerably, hence the differences in t_s between these two cases are not so significant.

Figure 3.6 shows the same plots while we decrease the thickness of the foil to $l_0 = 0.1\lambda_L$ and consequently increase the density $n_{e0} = 83.3n_{cr}$ to keep Eq. (2.27) satisfied. The average energy is also the same and agrees with Eqs. (2.25) and (2.28), and the developing time $t_s = 14.5T_L$ is $2T_L$ less than the original case, that is, the energy spread at $17T_L$ is $\Delta E / E = 22.8\%$, slightly greater than the case of thicker foil, since initially when electrons are pushed forward, a denser proton foil has a greater relative initial density perturbation and Coulomb repulsion force. The similarity between these two cases shows that the scaling law within the range of moderately altered density and thickness is still valid with marginally modified t_s values.

3.5. Advantages and Limitations

In summary, we have reported here the energy scaling of accelerated protons and carbon ions with laser radiation intensity for the laser radiation pressure acceleration of thin foils. We found that with a laser power of about one petawatt, quasi

monogenetic protons with 200 MeV and carbon ions with 100 MeV per nucleon can be obtained. The limit of energy is due to that light leaks through the foil caused by self-induced transparency at the density minima at the nonlinear stage of the Raleigh-Taylor instability. To extend the acceleration time, we need to either find method to slow down the growth of RTI, or search another way to accelerate the proton even after electrons becoming transparent to the laser. We found out that the latter approach seems to be promising and relatively easy to achieve experimentally by simply introducing a multi-species foil. We therefore continue to discuss the mechanism and comparison in detail in the following chapter.

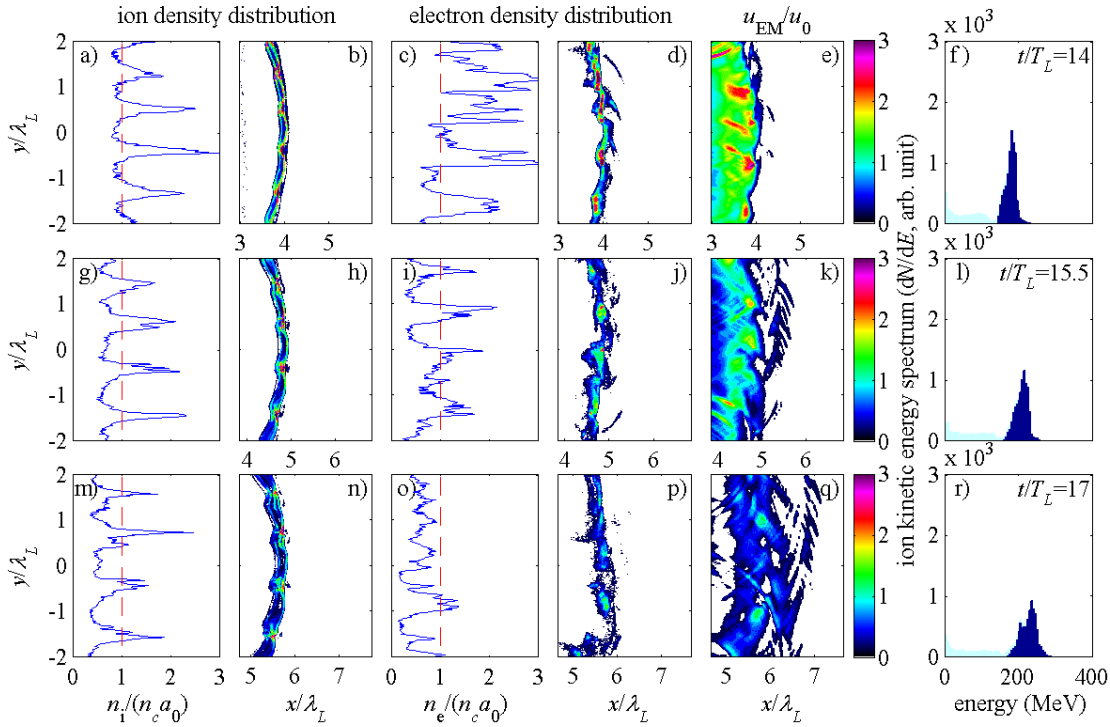

Figure 3.1: 2D PIC simulation results of the evolution of averaged proton density transverse to laser beam (the first column), proton density map (the second column), averaged electron density transverse to laser beam (the third column), electron density map (the fourth column), normalized electromagnetic field energy density over incident laser energy density (the fifth column) and energy spectrum of the protons (the sixth column) at three instants. Top, middle, and bottom rows are at $t = 14T_{\mathrm{L}}$, $15.5T_{\mathrm{L}}$, and $17T_{\mathrm{L}}$, respectively. The red vertical dashed lines in the first and the third columns show the critical density value. In the last column, dark-blue histograms show proton spectra collected within a window of $|y| < \lambda_{\mathrm{L}}$ and a width of $\lambda_{\mathrm{L}}/2$ in x co-moving with the foil; light-blue ones show proton spectra within $|y| < \lambda_{\mathrm{L}}$ and covering the entire simulation range in x.

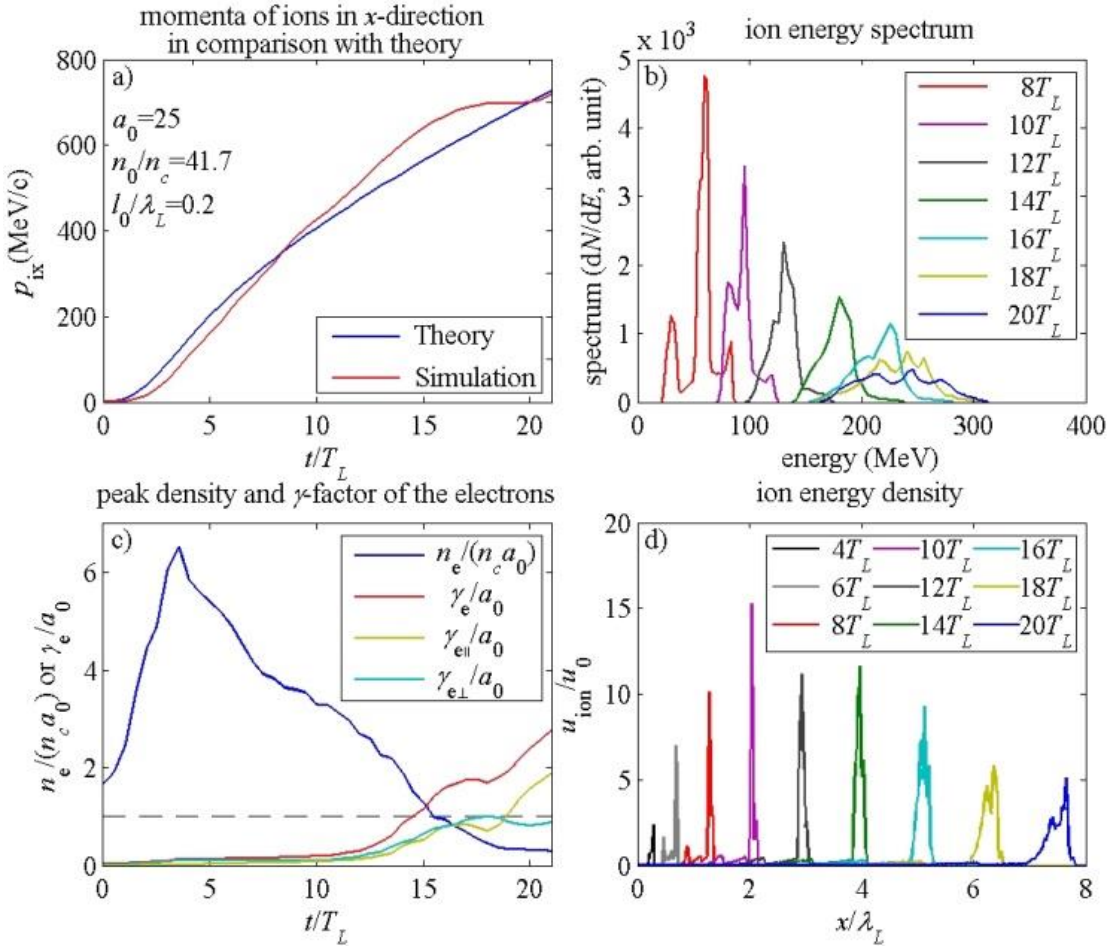

Figure 3.2: Simulation results with the same input parameters as in Figure 3.1. (a) Time evolution of ion momentum averaged within a $0.5\lambda_{\mathrm{L}} \times 2\lambda_{\mathrm{L}}$ window co-moving with the target from simulation (red line) and 1D theoretical calculation (blue line) using Eqs. (2.25) and (2.28). (b) The evolution of ion energy spectra collected within the window as defined in (a). (c) The time evolution of normalized average density $n_{\mathrm{e}}/(n_{\mathrm{cr}} a_0)$, of the electron layer (blue line), average γ_{e}/a_0, $\gamma_{\mathrm{e}\parallel}/a_0$, and $\gamma_{\mathrm{e}\perp}/a_0$ within a $0.05\lambda_{\mathrm{L}} \times 4\lambda_{\mathrm{L}}$ window co-moving with the target. The time when $n_{\mathrm{e}}/(n_{\mathrm{cr}} a_0) \approx 1$ is around $t = 16T_{\mathrm{L}}$. (d) Evolution of the spatial distribution of the normalized ion energy density. The energy density is averaged over $1\lambda_{\mathrm{L}}$ in y. The normalization factor $u_0 \approx 5.7 \times 10^{16}\,\mathrm{J/m^3}$ is the incident laser energy density.

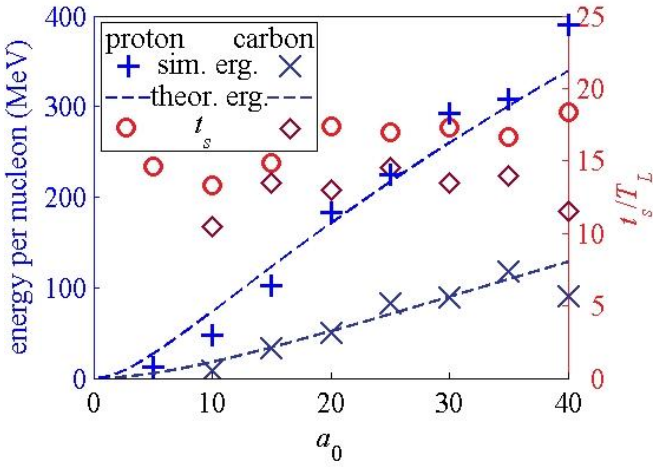

Figure 3.3: The energy scaling from 2D PIC simulations for protons and carbon ions. The saturation time t_s is recorded when the maximum of quasi-monoenergy (under the constraint $\Delta E / E_p \leq 20\%$) is obtained. The dashed lines are theoretical calculations of the energy scaling.

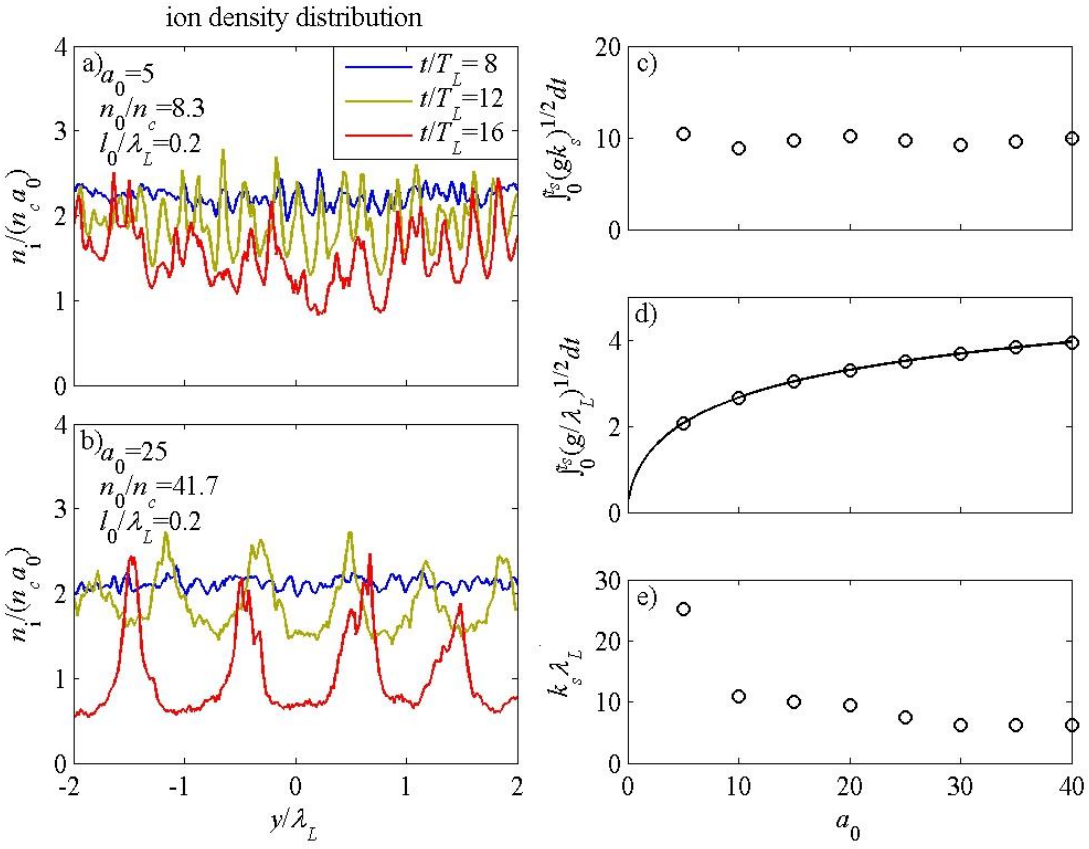

Figure 3.4: (a) The transverse ion density distribution averaged over a window along the laser propagation direction with the normalized laser wave amplitude $a_0 = 5$, $n_{e0}/n_{cr} = 8.3$, at $t = 8T_L$, $t = 12T_L$ and $t = 16T_L$. (b) The case of incident laser amplitude $a_0 = 25$ and target density $n_{e0}/n_{cr} = 41.7$ at the same time instants as in (a). (c) The dependence of the total growth α of the mode with wave number k_s at the saturation time on the laser amplitude. (d) Values of $\int_0^{t_s}(g/\lambda_L)^{1/2}\mathrm{d}t$ vs. normalized laser amplitude a_0. (e) $k_s\lambda_L$ vs. a_0, where $2\pi/k_s$ is the dominant transverse periodic structure scale length just before the broadening of the proton energy spectrum in the simulation.

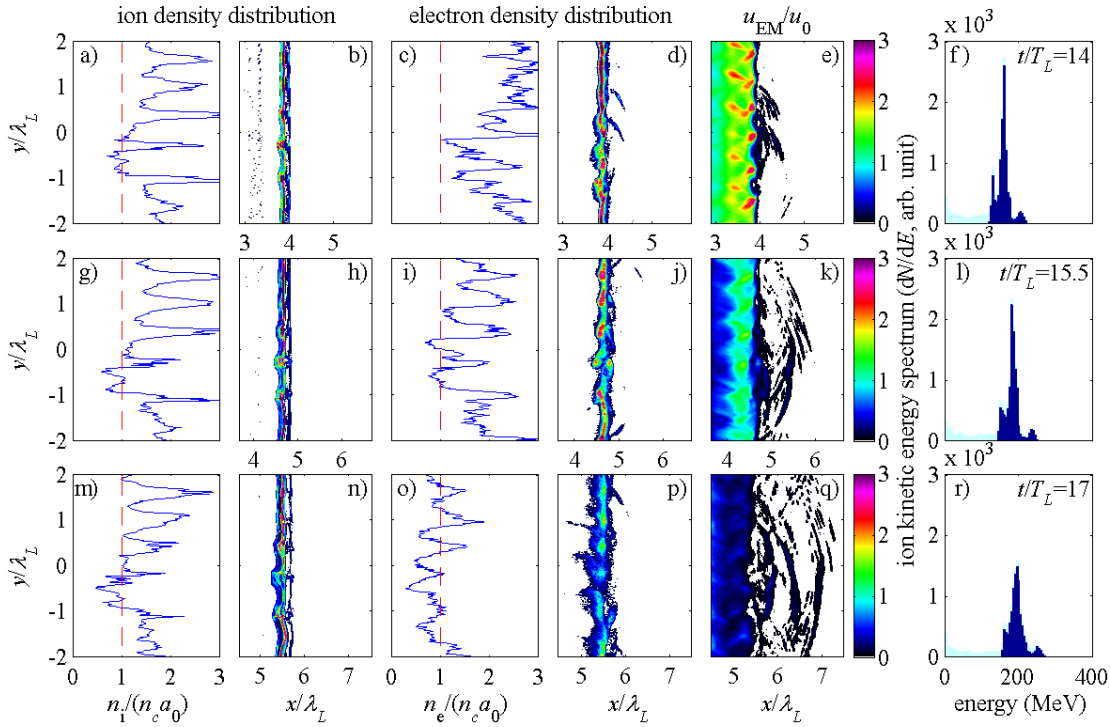

Figure 3.5: The same simulation as in Figure 3.1 but the Gaussian beam is replaced by a plane wave.

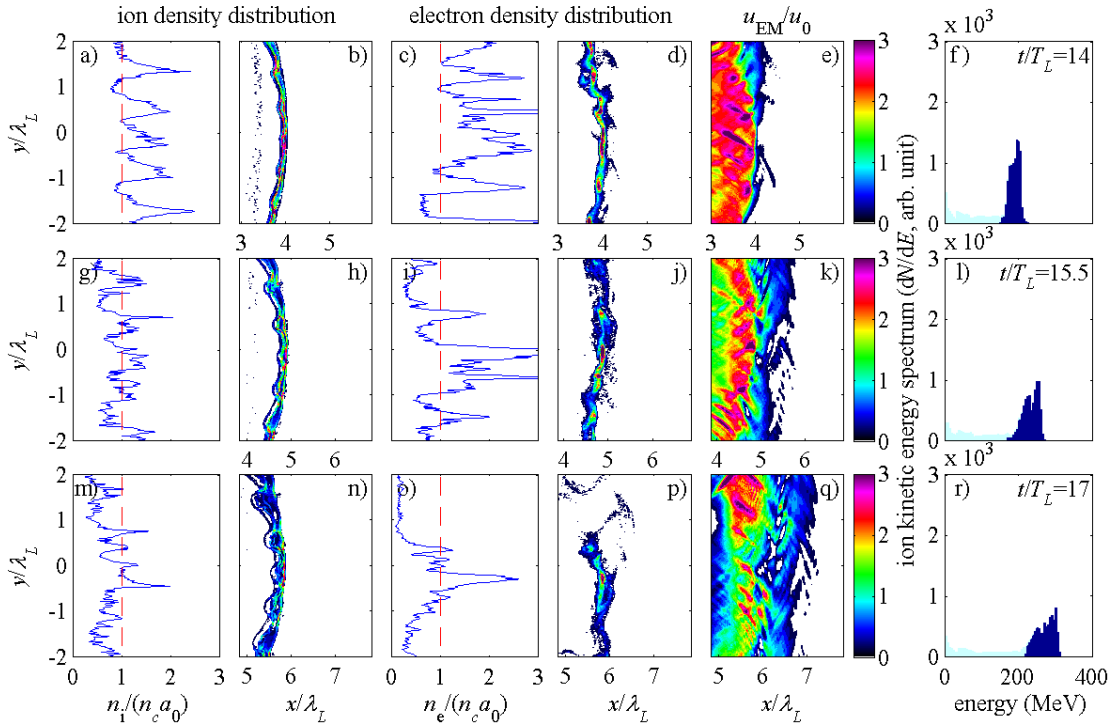

Figure 3.6: The same simulation as in Figure 3.1 but the foil density is doubled and thickness is halved.

Chapter 4

Multi-Ion Foils and Coulomb Repulsion

The acceleration of protons by combination of laser radiation pressure acceleration and Coulomb repulsion of carbon ions in a multi-species thin foil made of carbon and hydrogen is studied theoretically and numerically. The carbon layer helps delay the proton layer from disruption due to the Rayleigh-Taylor instability, maintain the quasi-monoenergetic proton layer, and accelerate it by the electron-shielded Coulomb repulsion for much longer duration than the acceleration time using single-ion hydrogen foils. Particle-in-cell simulations with a normalized peak laser amplitude of $a_0 = 5$ show a resulting quasi-monoenergetic proton energy of about 70 MeV with the foil made of 90% carbon and 10% hydrogen, in contrast to 10 MeV using a single-ion hydrogen foil. An analytical model is presented to explain quantitatively the proton energy evolution in agreement with the simulation results. The energy dependence of the quasi-monoenergetic proton beam on the concentration of carbon and hydrogen are also examined.

4.1. Introductions

Recently, laser ion acceleration for applications to proton cancer therapy gains great interest because its low collateral damage to healthy tissue [63,65,105]. In proton cancer therapy, monoenergetic proton beams of high quality with fluxes of 10^9 to 10^{11} particles per second and with a tunable energy 50-250 MeV are required to target the tumor location. In previous chapters, it was shown that with moderate laser intensity $a_0 = 5$, the proton energy obtainable is only 10 MeV, not enough for medical

application. However, in this chapter, we report an effective way of laser acceleration of quasi-monoenergetic protons with modest laser power using multi-species targets.

It was shown in previous chapter by 2D PIC simulations that the RTI can limit the ion acceleration achieved by RPA and broaden the proton beam's energy spectrum [39,41,45,50–52]. It puts a limit on the time a foil can be accelerated before it becomes transparent to the laser light and loses its monoenergetic properties. For RPA of a thin-foil target of one species, the energy scaling study with PIC simulations as shown in Figure 3.3 indicates that a high power (2-3 petawatt) laser is needed to obtain around 200 MeV quasi-monoenergetic protons with an energy spread within 20% of the peak flux energy. Several researches on understanding and overcoming the unfavorable RTI effect were performed [51–55], and it is still an ongoing problem.

We here show that generation of 60 MeV proton beam with modest laser power of 70 TW is feasible by combining the RPA and shielded Coulomb repulsion (SCR), using a multi-ion foil made of majority carbon (90%) and minority hydrogen (10%). This combination can significantly extend the duration of acceleration for the quasi-monoenergetic protons, and hence a proton beam with much higher energy can be produced with the same laser power. The carbon layer delays the disruption of proton layer due to the RTI significantly while accelerating the proton layer and maintaining its integrity. Earlier work [56] on using the Coulomb repulsion force between ions in acceleration used a laser beam with high intensity to sweep out the electron and to instantaneously accelerate protons by direct Coulomb explosion. Here we instead apply a laser beam with modest power and observed that the acceleration is stable for a long time while the repulsive force is partially shielded by the electrons. There have been a

few studies of the interactions between laser and multi-species targets [55,57,58] that indicate the similar proton acceleration. However, the physics of acceleration and scaling of achievable proton energy in not well understood. In particular, Qiao *et al.* [57] proposed late stage proton acceleration due to leaky laser radiation, whose physics is different from what we consider here, the combined RPA and SCR mechanism. In this paper, we present the scaling of the proton energy with respect to the initial carbon-hydrogen concentration ratios and the initial density of the foil by using 2D PIC simulations. Finally, we present a theoretical model of the proton acceleration by SCR that agrees well with simulation results.

4.2. Scheme of Acceleration

Here we employ 2D PIC simulations to study the production of quasi-monoenergetic protons generated by the combination of RPA and SCR of a multi-ion foil consisting of carbon and hydrogen. The simulation domain is $-30 \le x/\lambda_{\mathrm{L}} \le 70$, $-15 \le y/\lambda_{\mathrm{L}} \le 15$ and is divided into 100 grids per wavelength. The field boundary conditions are absorbing at the $\pm y$ and $+x$ boundaries, and the laser beam is injected at the $-x$ boundary. Absorbing boundary conditions are used for the particles at all boundaries. The foil is initially located at $0 \le x \le l_0$ with $l_0 = 0.2\lambda_{\mathrm{L}}$ being the foil thickness, and is resolved by 49 quasi-particles of each species per grid. The time step is $0.0067T_{\mathrm{L}}$, with $T_{\mathrm{L}} = 3.33\mathrm{fs}$, corresponding to $\lambda_{\mathrm{L}} = 1\mu\mathrm{m}$. The amplitude of the incident circularly polarized laser has a Gaussian profile in the transverse direction with the spot size being $16\lambda_{\mathrm{L}}$ in diameter and a time profile of $3\lambda_{\mathrm{L}}$ Gaussian rising time and a continuous waveform thereafter.

Figure 4.1 shows a comparison between the acceleration of a foil consisting of (a) 90% carbon and 10% hydrogen, and (b) pure hydrogen, accelerated by a circularly polarized laser beam of normalized amplitude $a_0 = \max(a_y) = \max(a_z) = 5$, corresponding to $I_0 = \varepsilon_0 m_e^2 c^3 \omega_L^2 a_0^2 / e^2 = 3.4 \times 10^{19}\,\mathrm{W/cm^2}$. The initial electron density is $n_{e0} = 8.3 n_{cr} = 9.25 \times 10^{21}\,\mathrm{cm^{-3}}$, which satisfies the optimal thickness condition [Equation (2.27)] of the radiation pressure acceleration of a single-species foil. The comparison between the single- and multi-species foil cases shows clearly that the acceleration time for the multi-species foil is significantly longer, and the obtainable proton energy is higher. For the RPA of a hydrogen foil, the RTI destroys the electron layer and widens the energy spectrum of the protons within 20 wave periods. During the RPA, once the electron density of the foil falls below the critical value, the laser light can leak through the target and no longer efficiently accelerates the protons. On the other hand, for the acceleration of a multi-ion foil, the mechanism of the acceleration can be divided into two phases. During the RPA phase, while the whole foil is accelerated, the lighter protons with greater charge-to-mass ratio pass ahead of the heavier carbon ions. The RTI creates transverse density ripples in the carbon and proton layers. When the electron layer becomes underdense due to the RTI, it is no longer pushed by the radiation pressure, and the carbon layer stops being accelerated, leaving the proton layer ahead. This leads to the SCR phase, where the net electrostatic field from the carbon-electron layer further pushes the proton layer forward and accelerates it to higher energy. After that the foil has become transparent to the laser light, the electron layer stabilizes to provide a static electrostatic field, which accelerates the protons and smoothens the transverse density ripples in the proton layer.

The whole process is shown as a series of cartoon in Figure 4.2. The protons are now held as a stable layer, boosting the acceleration time to about $200T_{\mathrm{L}}$, which is an improvement of one order of magnitude compared to the RPA of the single ion proton foil.

The acceleration mechanism is demonstrated quantitatively in Figure 4.3, where the proton layer is continuously accelerated [Figure 4.3(a)] while retaining its monoenergetic property [Figure 4.3(b)] even after that the electron layer has become transparent to the laser beam. In contrast, the carbon layer, which acts like the proton layer in the acceleration of a single-ion foil, is initially accelerated by RPA until the electrons become underdense due to the RTI. The acceleration of protons is attributed to the spatial charge distribution, which consists of the electrons in front of the proton layer and the partially shielded carbon layer behind it. Figure 4.3(c) shows the density distribution within $|y| < \lambda_{\mathrm{L}}$ when the electron density is far below the critical density. Due to the scarce amount of the electrons in front of the proton layer, the acceleration from behind (the SCR) is the dominant factor pushing the proton layer forward. To differentiate the contribution of the static electric field behind the proton layer at position x_{p} to the one ahead of it, the longitudinal electric field due to the charge sources from behind within $|y| < \lambda_{\mathrm{L}}$ by 1D calculation, $E_{x,\mathrm{L}}$, is shown in Figure 4.3(d), along with the electric field computed from the charges both behind and ahead of the foil, $E_{x,\mathrm{tot}}$, and the one obtained from the simulation, $E_{x,\mathrm{sim}}$. That is,

$$
\begin{aligned}
E_{x,\mathrm{L}} &= \frac{e}{2\varepsilon_0}\int_{-\infty}^{x_\mathrm{p}}[6\bar{n}_\mathrm{C}(x)-\bar{n}_\mathrm{e}(x)]\mathrm{d}x \\
E_{x,\mathrm{tot}} &= \frac{e}{2\varepsilon_0}\int_{-\infty}^{\infty}[6\bar{n}_\mathrm{C}(x)-\bar{n}_\mathrm{e}(x)]\mathrm{sgn}(x_\mathrm{p}-x)\mathrm{d}x\,, \\
E_{x,\mathrm{sim}} &= \bar{E}_x(x=x_\mathrm{p})
\end{aligned}
\tag{4.1}
$$

where the bar notation indicates taking average along y direction over the range $|y|<\lambda_\mathrm{L}$. At later stage ($t>80T_\mathrm{L}$), we can see that the electric field from the charges behind is the major portion of the total electric field at the position of the proton. The good agreement between the simulation data and the 1D electric field interpretation in Figure 4.3(d) also shows that using 1D model in computing the equation of motion can relatively simply describe the acceleration scheme quantitatively within acceptable errors, which leads to the argument shown in Section 4.4.

4.3. Energy Scaling with Concentration

By increasing the percentage of carbon ions, the portion of protons falling behind decreases and the Coulomb repulsion from the carbon ions becomes higher. Therefore, the protons can continue to be accelerated as a monoenergetic layer for a longer time. The obtainable energy is also substantially increased. To explore the relationship between the concentration of carbon and the obtainable energy, we perform a series of simulations increasing the fraction of carbon in the foil with 10% increment, decreasing the fraction of proton accordingly and keeping the initial electron number density as a constant. The result is shown in Figure 4.4. For carbon concentration lower than 50%, there are two mechanisms dominating the obtainable energy with increasing carbon percentage – reduction of the RPA due to a heavier foil and enhancement of the SCR due to a larger amount of carbon ions and less overlapping

between the carbon layer and the proton layer. The latter factor becomes relatively more significant with increasing carbon concentration, and at 50%, the Coulomb repulsion is large enough to compensate the reduction of the RPA.

The obtainable energy from the Coulomb force is proportional to the total charge of the carbon layer, leading to a larger electric potential. Increasing the carbon concentration can provide greater repulsive force and energy. It is shown in Figure 4.4 that in the region of small carbon percentage, the obtainable proton monoenergy is slightly decreased with increasing carbon percentage. In this region, the separation of the carbon and proton layers is not significant, so that the repulsion force from the carbon layer is not large enough to enhance the obtainable energy against the reduction of the RPA. For higher carbon concentration, the proton layer is almost totally separated from the carbon ion layer during the RPA phase, and it thus maintains monoenergy for a longer time and accelerates more efficiently. With $a_0 = 5$, corresponding to the intensity of $7 \times 10^{19}\,\mathrm{W/cm^2}$ and the power of 70 TW (with spot size diameter $16\lambda_L$), the obtainable proton quasi-monoenergy for 90% carbon and 10% hydrogen composite target can reach as high as 61 MeV, more than five times the energy obtainable from pure hydrogen targets.

4.4. Theoretical Model of Proton Acceleration by Coulomb Repulsion

From discussion above (see Figure 4.4), we conclude that high carbon concentration helps to increase the obtainable proton energy through SCR. We would like to present here a theoretical model for shielded Coulomb repulsion of the protons by the carbon layer. We first derive the electric potential and the electric field of the

electron-shielded carbon layer and then solve the equation of motion for the proton, as a test particle in the given field. We assume that the carbon and proton layers are completely separated, and protons are such small minority with almost no effects on the carbon motion. We consider the electrostatic force on the proton layer (acting like a test particle) in a frame moving with the constant velocity v_{C} of the carbon layer. The terminal velocity is achieved due to the RPA phase, which is terminated when the electrons become almost transparent to the laser light. This is due to the RTI rendering the electron layer density ripple so large that the electron layer becomes underdense, and the radiation pressure can no longer holds the electrons. The electrons can move until they achieve the balance of the electric force and the thermal force due to their pressure, which is then of the order of radiation pressure, indicating their temperature being of the order of ponderomotive energy. The electron density thus has a Boltzmann distribution as electrons are very hot, and the electrostatic potential on the proton layer with the electron screening is governed by the Poisson equation with Boltzmann electrons as a charge source,

$$\frac{\mathrm{d}^2\phi}{\mathrm{d}x^2} = \frac{en_0}{\varepsilon_0}\exp\left(\frac{e\phi}{k_{\mathrm{B}}T_{\mathrm{e}}}\right), \tag{4.2}$$

where the electric field boundary condition is determined by the net charge of carbon ions and electrons via Gauss's law. Multiplying equation (2) by $\mathrm{d}\phi/\mathrm{d}x$ and integrating along x, we have

$$\frac{1}{2}\left(\frac{\mathrm{d}\phi}{\mathrm{d}x}\right)^2 = \frac{n_0 k_{\mathrm{B}} T_{\mathrm{e}}}{\varepsilon_0}\left[\exp\left(\frac{e\phi}{k_{\mathrm{B}}T_{\mathrm{e}}}\right) + C_1\right]. \tag{4.3}$$

Integrating again, we then have

$$\phi(x) = \frac{2k_{\mathrm{B}}T_{\mathrm{e}}}{-\mathrm{e}} \ln\left[\frac{1}{\sqrt{C_1}} \sinh \sqrt{\frac{C_1}{2}} \left(\frac{x}{\lambda_{\mathrm{D}}} + C_2 \right) \right], \tag{4.4}$$

where C_1 and C_2 are integration constants, and $\lambda_{\mathrm{D}} = \sqrt{\varepsilon_0 k_{\mathrm{B}} T_{\mathrm{e}} / n_0 e^2}$ is the Debye length. Therefore the electric field can be derived from the electric potential as

$$E_x = -\frac{\mathrm{d}\phi}{\mathrm{d}x} = \frac{\sqrt{2C_1}k_{\mathrm{B}}T_{\mathrm{e}}}{e\lambda_{\mathrm{D}}} \coth \sqrt{\frac{C_1}{2}} \left(\frac{x}{\lambda_{\mathrm{D}}} + C_2 \right). \tag{4.5}$$

The integration constant C_1 can be determined without knowing the detailed charge distribution by Gauss's law that $E_x = \sigma_{\mathrm{net}} / 2\varepsilon_0$ when the position x is very far from the carbon layer, where $\sigma_{\mathrm{net}} = e\int (6n_{\mathrm{C}} - n_{\mathrm{e}})\mathrm{d}x$ is the net surface charge density of the carbon-electron foil. That is,

$$E_x \to \frac{\sqrt{2C_1}k_{\mathrm{B}}T_{\mathrm{e}}}{e\lambda_{\mathrm{D}}} = \frac{\sigma_{\mathrm{net}}}{2\varepsilon_0} \Rightarrow \sqrt{2C_1} = \frac{e\lambda_{\mathrm{D}}\sigma_{\mathrm{net}}}{2\varepsilon_0 k_{\mathrm{B}} T_{\mathrm{e}}}. \tag{4.6}$$

The whole system moves with velocity v_{C}, and hence the constant C_2, acting as a shift in x without altering the field profile, can be absorbed into the initial condition of the position. We can then express the equation of motion in the lab frame as

$$\begin{cases} \dfrac{\mathrm{d}x_{\mathrm{p}}}{\mathrm{d}t} = v_{\mathrm{p}} \\ \dfrac{\mathrm{d}(\gamma_{\mathrm{p}} v_{\mathrm{p}})}{\mathrm{d}t} = \dfrac{eE_x}{m_{\mathrm{p}}} = \dfrac{e\sigma_{\mathrm{net}}}{2\varepsilon_0 m_{\mathrm{p}}} \coth \dfrac{(x - v_{\mathrm{C}}t)e\sigma_{\mathrm{net}}}{4\varepsilon_0 k_{\mathrm{B}} T_{\mathrm{e}}} \end{cases}. \tag{4.7}$$

The system of equations (4.7) can be solved numerically with the coefficients and initial conditions obtained from the simulation. The parameters and the results using a foil made of 90% carbon and 10% hydrogen are shown in Figure 4.5. The initial time is chosen to be $t_0 = 50T_{\mathrm{L}}$, the time of complete separation between the carbon ion layer and the proton layer as shown in Figure 4.5(a). The initial displacement is

determined by the initial acceleration, and the result $x_{p0} - v_C t_0 = 1.3\lambda_L$ is consistent with the density plot shown in Figure 4.5(a), where the carbon layer velocity v_C, as shown in Figure 4.3(a), is a constant $0.07c$, comparable to its sound speed. The evolution of the center of mass of the carbon layer as shown in Figure 4.5(b), in comparison with the integrated value from its average velocity, verifies that the carbon-electron system moves with a constant velocity and hence the validity of describing the accelerating process in the inertial frame moving with such velocity. The temperature of the Maxwell-distributed underdense electrons in the center-of-mass frame, as shown in Figure 4.5(c), is kept roughly a constant $k_B T_e = 2.46 m_e c^2$, defined by a best fit curve in its energy spectrum, by the continuous laser wave. The agreement in the distribution between the simulation and the theory also verifies the validity of equation (4.2). The difference in charges during $50 < t/T_L < 150$ within the window $-1 < y/\lambda_L < 1$ is seen in Figure 4.5(d), where we assume that particles escaping this range are not effectively participate in the acceleration scheme, is 0.07 times the initial electrons in average. This is the main factor deciding the acceleration and is the reason why we call it SCR. One important consequence from this observation is that a large concentration of carbon is necessary for the initially less abundant positive charges of carbon ions to overcome the gradually escaping electrons after the end of the RPA phase. Although the acceleration is relatively small compared to the RPA, the accelerating time is much longer due to the negative slope in the electric field, which exerts a greater force in the protons left behind. The comparison between the theoretical calculation and the simulation result in Figure 4.5(e) shows great consistency initially, and some deviation after the separation between the proton layer and the carbon ion layer being too large

to use the 1D approximation. To increase the obtainable energy, we should either increase the input amplitude (larger T_e and v_C) or apply greater amount of carbon ions (larger σ_{net}), which could be achieved by increasing the carbon concentration (Figure 4.4) or increasing the overall number of particles in the foil (discussed in the next section).

4.5. Further Energy Boost by Increasing the Initial Foil Density and the Input Laser Intensity

From the argument above, we can see that the acceleration and obtainable energy depends more on SCR with a higher carbon ion concentration. The acceleration due to SCR is proportional to the amount of positive charges behind the protons. Increasing the initial density seems to be a promising way of increasing the obtainable energy. As long as the carbon and proton layers are separated during the RPA phase, increasing the initial density can enhance not only the acceleration but also the number of protons.

To verify this statement, we carried out a series of simulations with the same parameters as mentioned in the previous section but setting the initial density three times as large. The result is shown in Figure 4.6. We first notice that the threshold for the enhancement in the SCR to compensate the reduction of the RPA is still around 50%, which gives an empirical general criterion in this acceleration scheme. Second, the acceleration time is significantly enhanced, especially in the cases of 80% and 90% carbon concentrations, which implies that the acceleration by SCR is very stable for high initial carbon concentration.

In Figure 4.7, we show a case with higher intensity $a_0 = 10$, which corresponds to 270 TW power. It shows that 100 MeV monoenergy protons could be achieved with multi-ion foils, whereas with a single ion foil it can reach a monoenergy of merely 50 MeV [44]. The result in Figure 4.7 shows that the monoenergetic peak at $t = 190T_L$ with energy 110 MeV is sharp ($\Delta E / E = 7\%$), omitting the low-energy peak due to the protons moving backwards.

4.6. The Effects of Smaller Spot Size

The evolution of energy in the one-dimensional theoretical model discussed in section 4.5 fits well if the charge distribution in the center part is independent of the perpendicular dimension y. This assumption fails far away from the foil if a smaller laser spot size of $2\lambda_L$ instead of $16\lambda_L$ is used. However, even though the acceleration value calculated in the 1D model does not match the 2D simulation value, the mechanism for SCR is the same. The density distribution in Figure 4.8 shows that only the particles in the vicinity of the center axis are affected, and the protons from the center part then expands largely in *y*-direction. Immobility of carbon ions in large-*y* region results in less effective acceleration, as shown in Figure 4.8(d) that only 22 MeV of proton beam, corresponding to $\gamma\beta_x = 0.22$, is obtained. Greater expansion of protons in *y*-direction largely reduces the total number of protons in the quasi-monoenergetic peak to 1.7×10^6, about 1/30 of the value obtained with the original parameters, which is 5.5×10^7. However, since the input power of the laser beam due to a smaller spot size is also reduced to 1/64 (1.1 TW in value), the portion of laser energy converted to the quasi-monoenergetic protons is 90% of the value with large spot size.

Therefore, this acceleration scheme could in principle be applied to cases with more realistic settings as well.

4.7. Conclusions

In summary, we have compared the laser acceleration of single- and multi-species foils and found energy scaling for different ion concentrations. The detrimental effects of the RTI of pure hydrogen foils are significantly reduced by the inclusion of carbon ions, which give an additional boost to the proton energy via SCR. With increasing carbon concentration, the acceleration time is significantly extended, and consequently the obtainable monoenergy is also considerably increased. In particular, we have found that there exists a critical value of carbon concentration, above which the shielded Coulomb repulsion is effective due to a distinct separation between the two different ion species. The proton monoenergy can be further boosted with a denser foil due to a greater repulsive force from the carbon ions. The resulting proton monoenergy could reach 78 MeV by using a laser beam of merely 70 TW, a significant reduction in required laser power. Moreover, 110 MeV of proton energy can also be obtained by a laser beam of input power 270 TW, which is a promising result for future applications.

It appears in this chapter that using multi-species foils is a perfect way to extend both acceleration and monoenergetic time. However, there are also some unfavorable side in this scheme. First of all, the majority species in the foil – the carbon ions do not have monoenergetic property at all, implying that the total number of protons is small compared to a pure-hydrogen foil. For example, in a C_9H_1 molecule, the ratio of total

carbon charge to proton charge is 54:1, meaning that the initial proton number is merely 2% in amount compared to a hydrogen foil with the same electron density. Moreover, since there is no radiation pressure from the laser to the electron layer after penetration, the laser energy can only be used to heat up electrons, which is not an efficient way of acceleration. In next chapter we discuss about further improvement in proton energy by modifying laser profile after penetration, followed by discussion on utilizing a laser with a more realistic short pulse profile in Chapter 6.

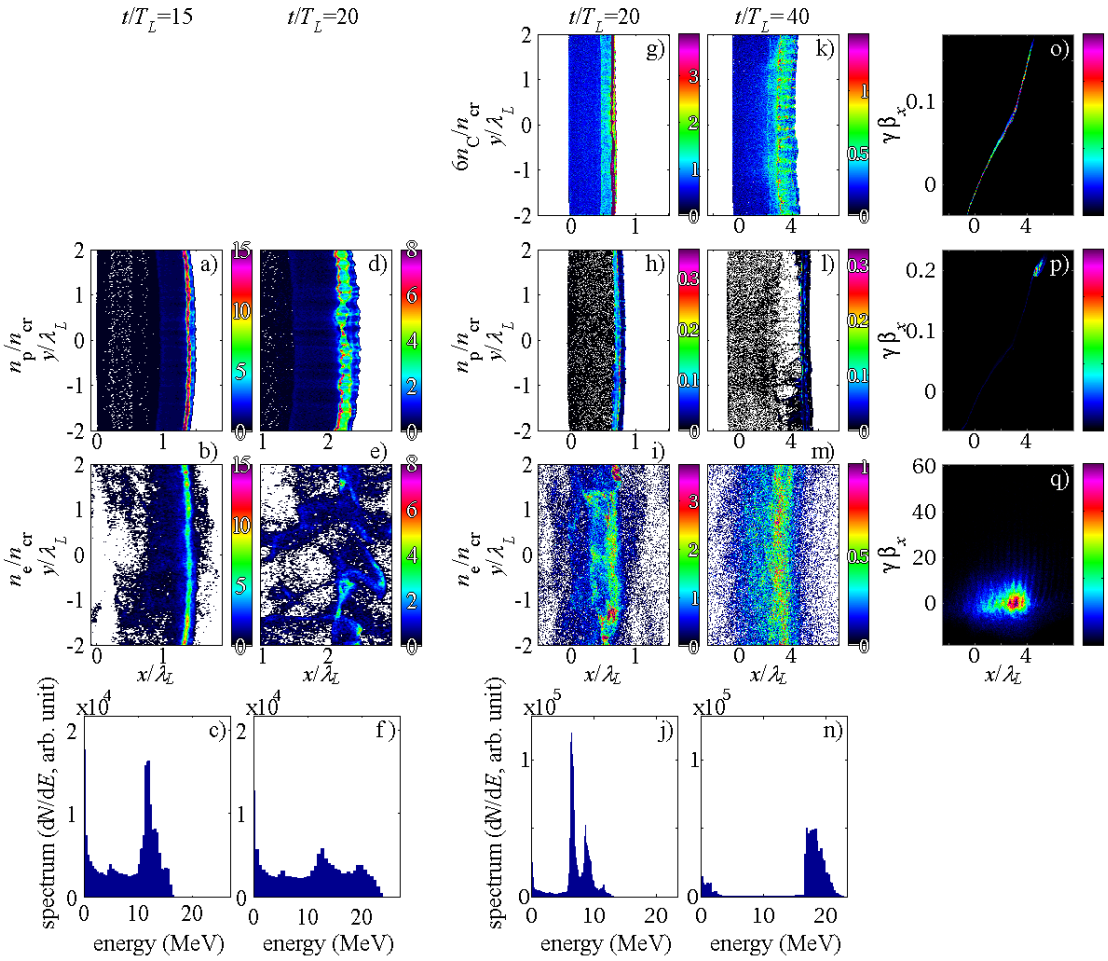

Figure 4.1: 2D PIC simulation results showing the evolution of a single-ion foil and a multi-ion foil accelerated by a circularly polarized laser. The first three rows from top are the density maps of the carbon ions, the protons and the electrons, respectively. The fourth row is the proton energy histogram within a window of $|y| < \lambda_L$ and covering the entire simulation range in x. The first and the second columns represent the times when electron layers become transparent and post-transparent, respectively, in the acceleration of a single-ion foil. The third and fourth columns represent the same condition in the acceleration of a multi-ion foil. The fifth column is the phase space of the fourth column with arbitrary units in the colorbars, which shows the trapping of the protons while the velocities of the carbon ions are widely spread. The color of zero value in this column is set as black to emphasize the difference.

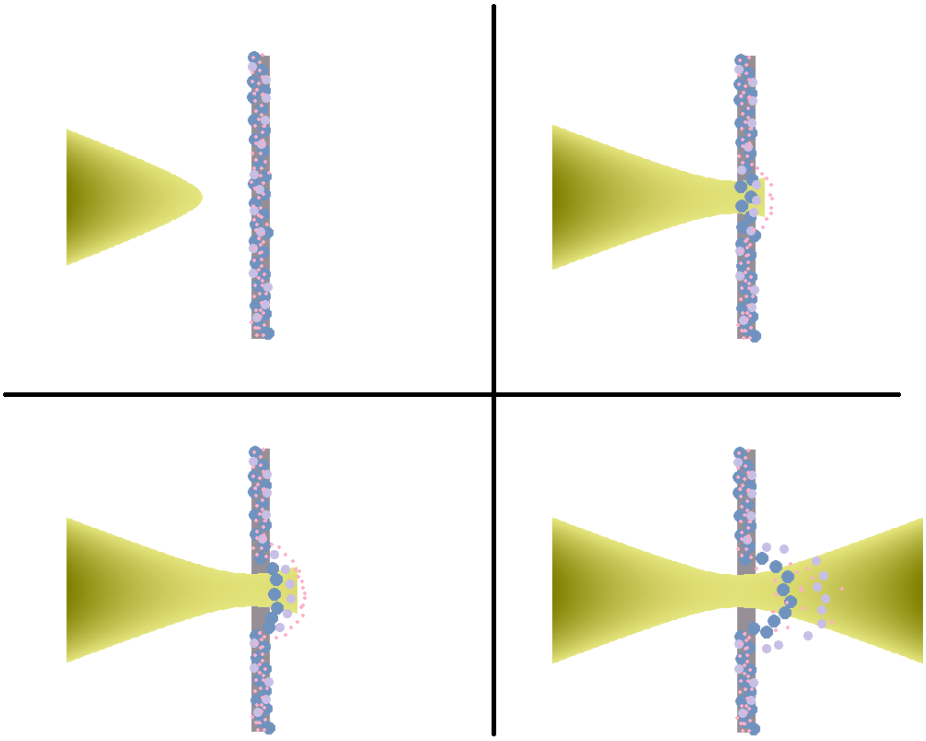

Figure 4.2: A cartoon showing the process of laser acceleration of multi-ion foil. The laser beam is shown in yellow, electrons in pink, protons in purple and carbon ions in blue.

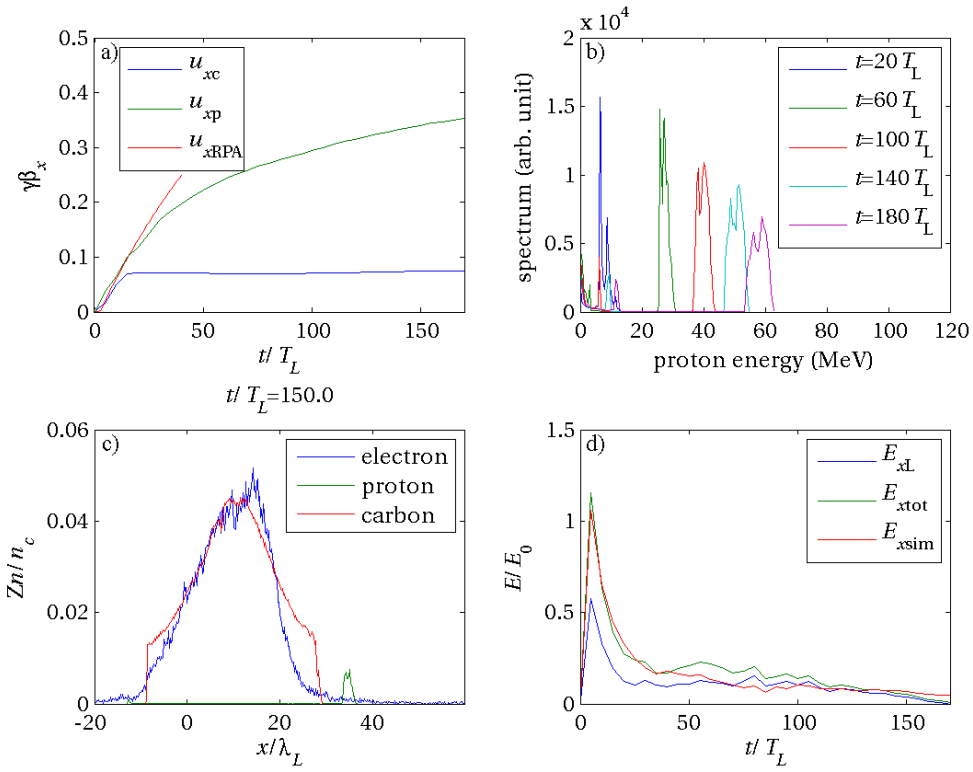

Figure 4.3: Simulation results with the same input parameters as the multi-ion case shown in Figure 4.1. (a) Time evolution of ion momenta averaged within a window of $|y|<\lambda_L$ and 1D theoretical calculation using Eqs. (2.25) and (2.28). The blue, green and red lines represent the average longitudinal velocities of the carbon ions, protons and the theoretical velocity prediction of the foil as a whole, respectively. (b) The time evolution of proton energy spectra within $|y|<\lambda_L$. (c) The charge density of the charged particles with respect to x at $y=0$ when $t=150T_L$. (d) The evolution of the longitudinal electric fields at the position of the proton foil computed from the charges from behind (blue line) and from both behind and ahead (green line), compared with the simulation results (red line).

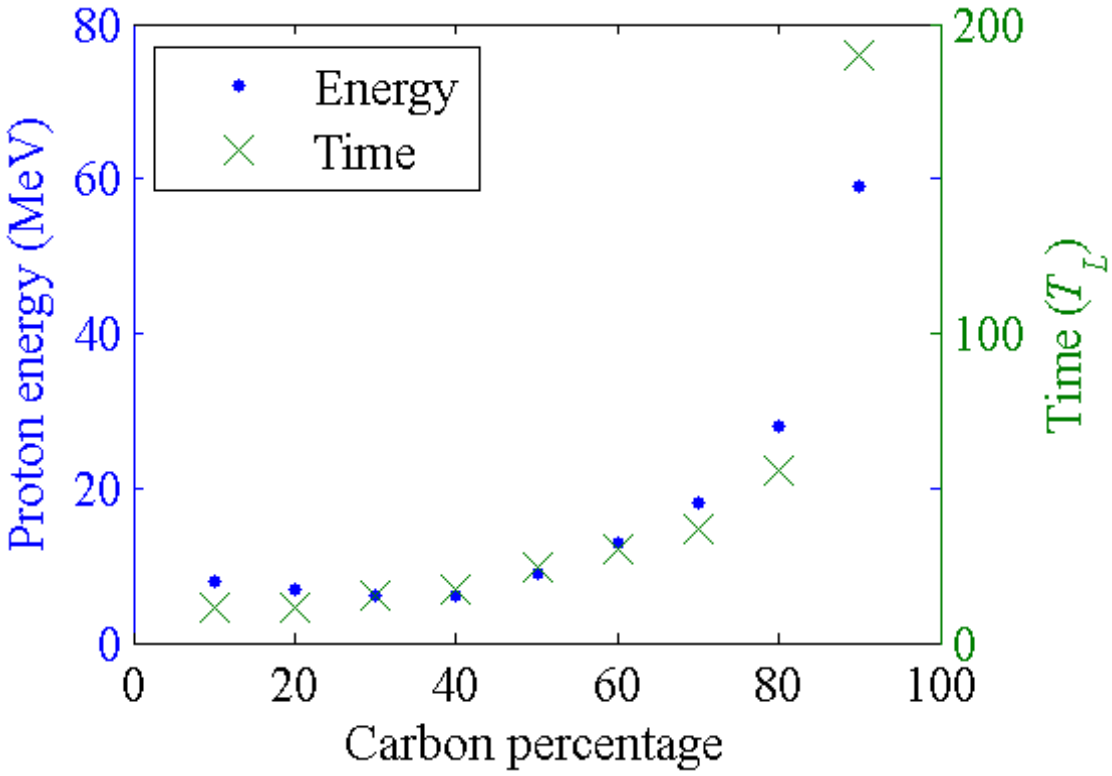

Figure 4.4: The energy scaling of protons with respect to the carbon concentration in the cases of multi-ion acceleration from 2D PIC simulations. The saturation time t_s is recorded when the maximum of quasi-monoenergy (under the constraint $\Delta E / E \leq 20\%$) is obtained.

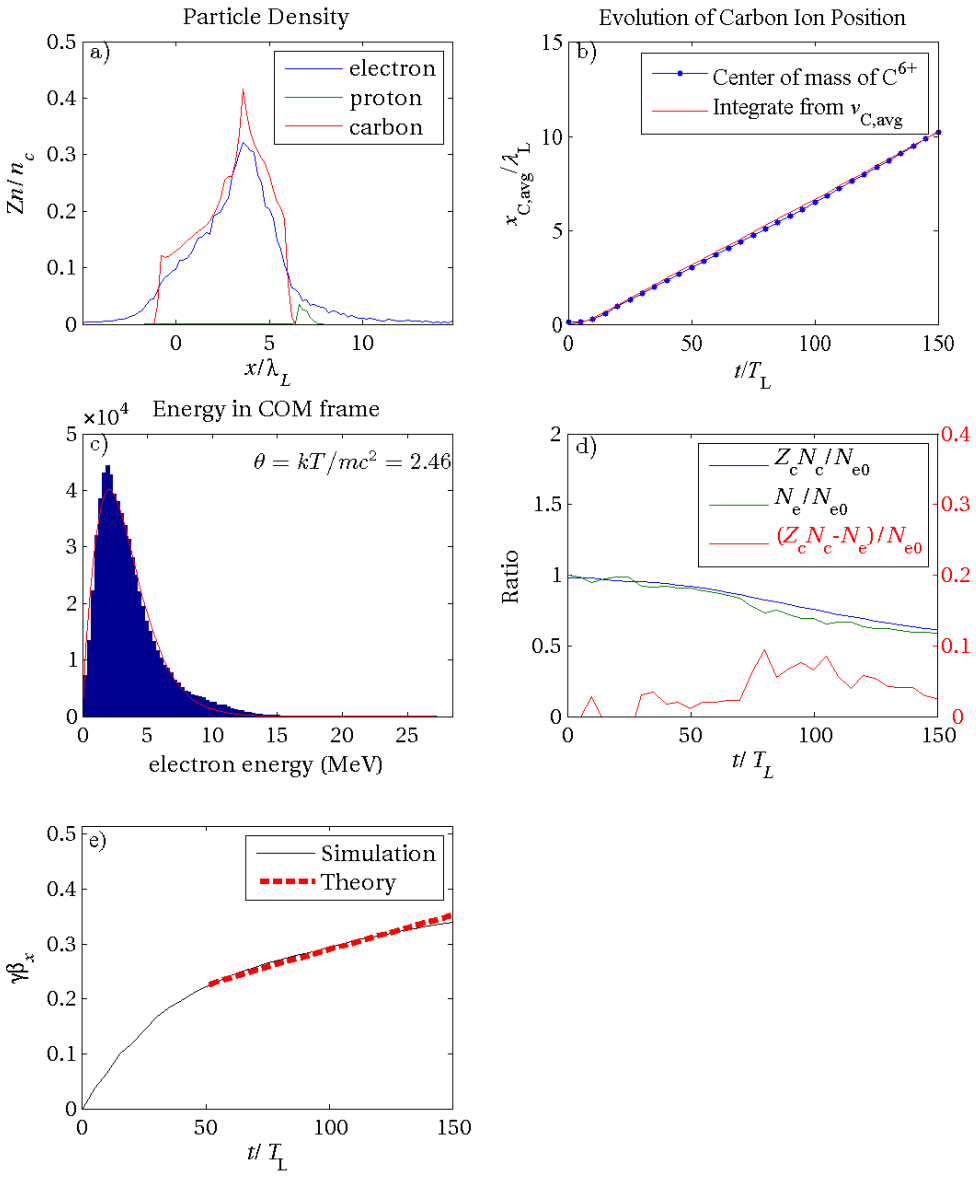

Figure 4.5: Simulation and theoretical results using a foil made of 90% carbon and 10% hydrogen: (a) the initial particle densities around the proton position $x_0 = 2.5\lambda_L$, (b) the center of carbon ion layer, (c) the electron energy distribution in center-of-mass frame, compared to a Maxwellian distribution with temperature $k_B T_e / m_e c^2 = 2.46$, (d) the relative particle densities in the foil, showing that the total relative particle charge is $\sigma_{net} / \sigma_{e0} = 0.07$, and (e) a comparison between the proton energy obtained in the simulation (solid line) and the theoretical SCR model (dashed line). The initial velocity $\gamma\beta_x = 0.022$ is used in the theoretical calculation.

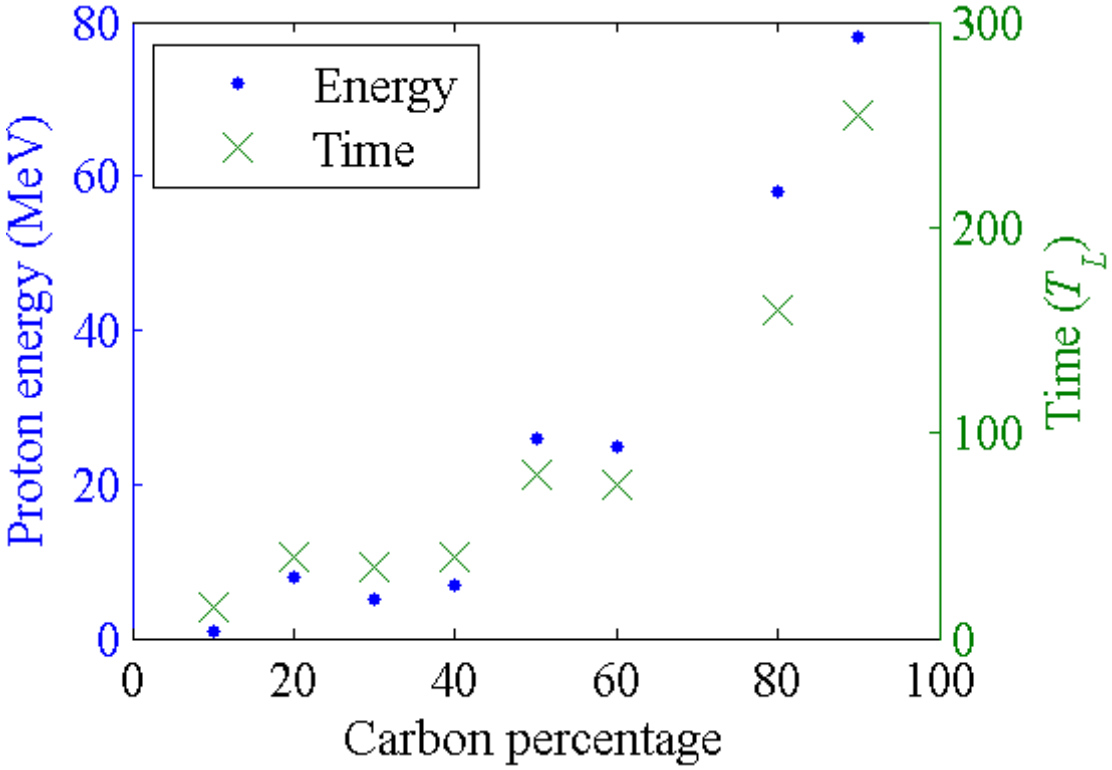

Figure 4.6: Similar plot as in Figure 4.4 but with three times as large initial foil densities.

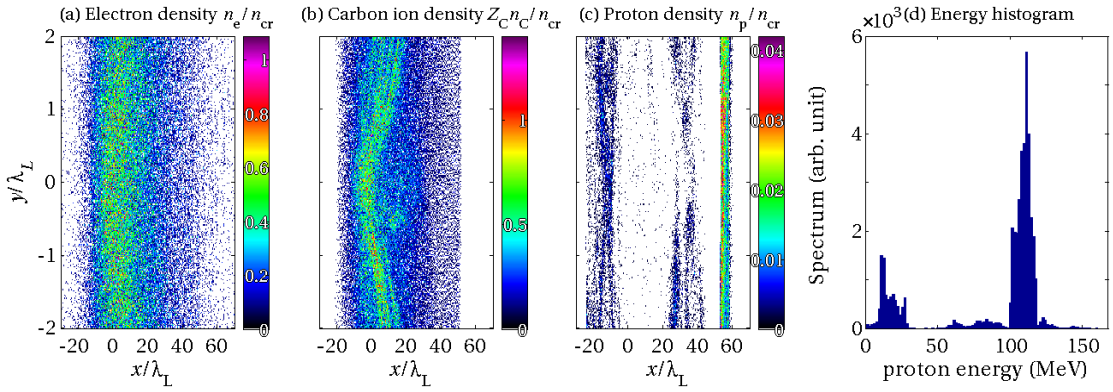

Figure 4.7: The simulation result at $t = 190T_L$ with input parameters the same as in Figure 4.1, except for $a_0 = 10$, $n_{e0} = 100n_{cr}$ and $n_{C0} : n_{p0} = 9:1$, showing the number densities of (a) electrons, (b) carbon ions, and (c) protons. Panel (d) shows the proton energy histogram within a window of $|y| < \lambda_L$, covering the entire simulation range in x.

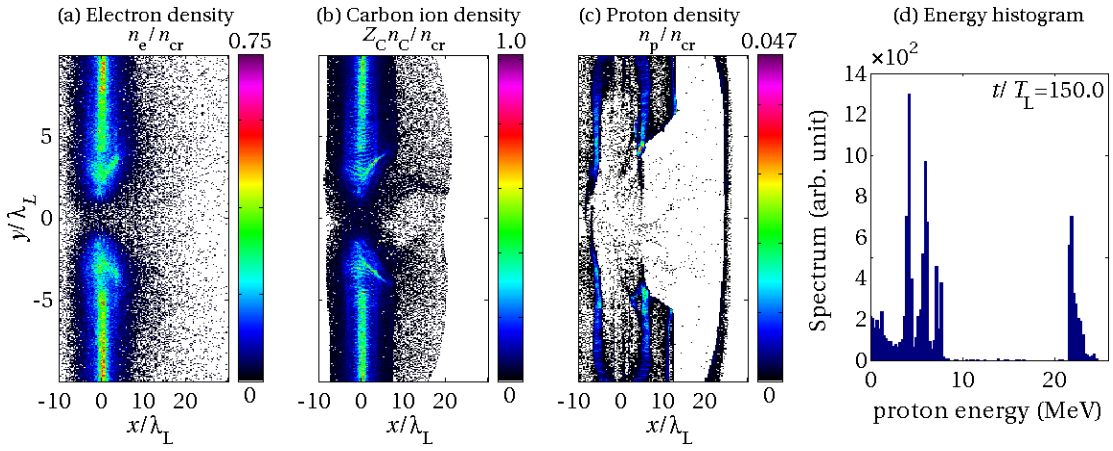

Figure 4.8: The simulation result at $t = 150T_L$ with input parameters the same as in Figure 4.1, except for the spot size being $2\lambda_L$ in diameter, showing the number densities of (a) electrons, (b) carbon ions, and (c) protons. Panel (d) shows the proton energy histogram within a window of $|y| < \lambda_L$, covering the entire simulation range in x.

Chapter 5

Further Improvement by Laser Profile Design – Laser Polarization Switch

In this chapter, we present a scheme to significantly increase the energy of quasi-monoenergetic protons accelerated by a laser beam without increasing the input power. This improvement is accomplished by first irradiating the foil several wave periods with circular polarization and then switching the laser to linear polarization. The polarization switch increases the electron temperature and thereby moves more electrons ahead of the proton layer, resulting in a space charge electric field pushing the protons forwards. The scaling of the proton energy evolution with respect to the switching time is studied, and an optimal switching time is obtained. The proton energy for the case with optimal switching time can reach about 80 MeV with an input laser power of 70 TW, an improvement of more than 30% compared to the case without polarization switch.

5.1. Introduction

The scheme of laser RPA of quasi-monoenergetic protons has been actively studied in theory and simulations[36–42,44,46] and experiments[49,62]. To overcome the problem of short accelerating time, researches have shown that the energy can be further increased by using a thin composite multi-ion proton-carbon foil [47,54–58]. In particular, Chapter 4 suggested that higher proton energy is mainly resulting from two different stages of acceleration – RPA and SCR stages. Using a laser beam with 70 terawatt power to irradiate a carbon-proton target with 10% protons, we can achieve a

quasi-monoenergetic proton beam with 60 MeV of energy, which is several times the energy obtainable from a pure hydrogen foil.

In this chapter, we present a scheme based on the SCR to further boost the energy of the monoenergetic protons without increasing the input laser power. It has been shown that circularly polarized waves can accelerate the protons mono-energetically by suppressing the oscillatory motion of electrons, whereas linear polarization waves broaden the electrons more rapidly with higher temperature[48,106,107]. In our scheme we combine the advantages of these two by switching the laser from circular to linear polarization after that the RPA has fully separated the protons from carbon ions, and the electron temperature is significantly increased due to the oscillatory ponderomotive force by the linearly polarized laser, allowing larger amount of electrons to be distributed in front of the proton layer and to provide a force pulling the proton layer forward. Our 2D PIC simulations show that 80 MeV of proton energy can be achieved using the polarization switch, an improvement of more than 30% compared to the previous result of 60 MeV using only circular polarization.

5.2. Simulation Setup

In order to demonstrate the acceleration scheme with polarization switch, we employ 2D PIC simulations and analyze the dynamics of the macro-particles to compare the differences among different switching conditions. The simulation domain is $-30 \le x/\lambda_L \le 70$ and $-15 \le y/\lambda_L \le 15$, and the grid size is $\lambda_L/100$ in both the x and y dimensions, where $\lambda_L = 1.0\,\mu\text{m}$ is the laser wavelength. The boundary

conditions are absorbing at all boundaries for particles and fields, and the laser electromagnetic wave is injected at the $-x$ boundary. The foil, consisting of 90% carbon and 10% hydrogen, is initially located at $0 \le x \le l_0$ and is resolved by 49 macro-particles of each species per cell with initial thickness $l_0 = 0.2\lambda_{\mathrm{L}}$ and electron density $n_{\mathrm{e}0} = 8.3 n_{\mathrm{cr}}$. Here $n_{\mathrm{cr}} = \varepsilon_0 m_{\mathrm{e}} \omega_{\mathrm{L}}^2 / e^2$ is the critical density, where m_{e} is the mass of an electron, e is the elementary charge, ε_0 is the vacuum permittivity and ω_{L} is the laser angular frequency. The amplitude of the incident laser beam has a Gaussian profile in the transverse direction with spot size, defined as the diameter at e^{-2} of the peak intensity, being $16\lambda_{\mathrm{L}}$. The spatial profile along the x-axis is shown in Figure 5.1. The profile of the input laser is a combination of an $L_{\mathrm{R}} = 3\lambda_{\mathrm{L}}$ Gaussian raising, continuous circular polarized wave until L_{S}, and then linear polarized wave thereafter. The normalized laser amplitude is $a_0 = eE_{y,z} / m_{\mathrm{e}} \omega_{\mathrm{L}} c = 5$, corresponding to 70 TW input power. The total power of the laser beam is the same before and after the switch, and therefore the amplitude after the switch is increased by a factor of $\sqrt{2}$. The switching parameter L_{S} is varied for different sets of simulations.

5.3. Simulation Results

We compare the simulation results for the cases with polarization switch at $L_{\mathrm{S}} = 25\lambda_{\mathrm{L}}$ and without polarization switch, as shown in Figure 5.2. The general acceleration mechanisms for both cases are similar. A triple layer consisting of proton, electron and carbon is formed, and the proton layer continues to be accelerated by Coulomb repulsion from the net charge of carbon and electron layers after that the RTI

has disrupted the electron layer. On the other hand, the density distributions of electrons, which shield most of carbon charge's contribution to Coulomb repulsion, are very different between the two cases. At the earlier stage $t = 50T_{\mathrm{L}}$ (upper half panels), we can visibly observe the wave-like structure in the longitudinal direction of the electron distribution from the foil irradiated by linear polarized laser beam (the first row), whereas the structure is smoother in the one with circular polarization (the second row). The linearly polarized laser beam conveys more energy to electrons due to both the oscillatory electric field in transverse direction and the enhanced peak amplitude, resulting in a distribution with more energetic electrons capable of staying in front of the proton layer instead of being pulled back by the carbon layer, as shown in the fourth column of Figure 5.2. Therefore, the shielding effect of Coulomb repulsion due to electrons trapped in the carbon layer is also strongly reduced, resulting in an increase of in the proton acceleration efficiency as shown in the last column of Figure 5.2.

At a later stage at $t = 150T_{\mathrm{L}}$ (lower half panels of Figure 5.2), a more clear improvement in the obtainable proton energy can be seen. We observe in the electron density distribution that the two key features of the case with a linear polarized beam (the third row of Figure 5.2), which are the oscillatory motion and ahead-of-proton distribution of electrons, last for a significant time. This heavy-tail distribution then provide a larger electrostatic force pushing the protons and resulting in a substantial improvement of the proton energy to 68MeV as shown in the last column of Figure 5.2. In comparison, a proton energy of only 55MeV is achieved in the case without switch (the fourth row of Figure 5.2).

5.4. Data Analysis

To explain the enhanced proton energy resulting from polarization switch, we further analyze the particle and field distribution data in detail. It has already been shown[47] that during the process of SCR, the proton energy evolution can be approximated by a simple one-dimensional model, assuming the proton layer as a test charge, the electron distribution as Maxwellian and the carbon layer as moving with constant velocity. The equation of motion of the proton layer is[47]

$$\begin{cases} \dfrac{\mathrm{d}x_\mathrm{p}}{\mathrm{d}t} = v_\mathrm{p}, \\ \dfrac{\mathrm{d}(\gamma_\mathrm{p} v_\mathrm{p})}{\mathrm{d}t} = \dfrac{eE_x}{m_\mathrm{p}} = \dfrac{e\sigma_\mathrm{net}}{2\varepsilon_0 m_\mathrm{p}} \coth \dfrac{(x_\mathrm{p} - v_\mathrm{C} t) e\sigma_\mathrm{net}}{4\varepsilon_0 k_\mathrm{B} T_\mathrm{e}}, \end{cases} \tag{5.1}$$

where $x_\mathrm{p}, v_\mathrm{p}$, and γ_p are respectively the position, velocity and relativistic gamma factor of the proton layer, v_C is the velocity of the carbon ion layer, e and m_p are respectively the charge and mass of a proton, ε_0 is the vacuum electric permittivity, k_B is Boltzmann's constant, E_x is the longitudinal electric field at x_p, T_e is the electron temperature and σ_net is the net surface charge density.

Equation (5.1) shows that there are mainly three parameters deciding the acceleration of the proton layer: $T_\mathrm{e}, v_\mathrm{C}$ and σ_net. In Figure 5.3, we demonstrate the fitting of electron energy histogram in the center-of-mass frame with relativistic Maxwellian distribution in the first two rows, one with polarization switch and the other without. It can be seen that not only do they fit well with Maxwellian distributions, which satisfies the assumption of the model, but the temperature of the case with polarization switch is also significantly greater, indicating a greater electric field and

acceleration as shown in Figure 5.4. The other two parameters v_C and σ_{net}, on the other hand, do not change considerably regarding the switch, as presented in Figure 5.5, implying that the remarkable improvement of proton velocity, which is also shown in the first column of Figure 5.5, results mainly from the wider distribution of hotter electrons.

To demonstrate the agreement between the simulation result and the theoretical prediction in 1D model, we plot the evolution of the average momentum of proton in Figure 5.6. The initial conditions we imposed in the theory are $k_B T_e / m_e c^2 = 6.0$, $\sigma_{net} / \sigma_{e0} = 0.07$, $\gamma_{p0} v_{p0} = 0.23c$ and $x_{p0} = 1.7\lambda_L$. This 1D model successfully describes the proton energy evolution while the distance between the proton and carbon layers are moderate compared to the laser spot size. However, the momentum evolution trend for large separation, which is comparable to the spot size as shown in Figure 5.6(a) when $t = 150T_L$, is then different. We apply a minor modification to consider the Coulomb potential in 2D situation when the separation between the proton and carbon layers is large and include the derivation in the next section. The comparison of momentum evolution between theoretical predictions and the simulation result are shown in Figure 5.6(b).

5.5. 2D Modification of the Equation of Motion

Previously, we calculated the equation of motion using 1D Poison equation. However, as the separation between the protons and the carbon ions becomes longer and longer, the consequence that electrostatic field converges to a non-zero constant in the 1D model is no longer valid, and therefore considering the equation of motion in

2D geometry becomes necessary. When distance is comparable with or greater than the spot size, we then neglect the insignificant portion of electrons moving to the other side of proton layer and assume simply that the net charge behind the proton layer is a constant and can be approximated as a uniformly charged cylinder with its axis aligned with z-direction. Therefore, the electric field can be simply written as

$$E_x = \frac{e}{2\pi\varepsilon_0 (x_\mathrm{p} - v_\mathrm{C} t)} \int_R n_\mathrm{net} \, \mathrm{d}\sigma \,, \tag{5.2}$$

where R denotes a limited region behind the proton layer where carbon ion is the dominant species. When $t = 150 T_\mathrm{L}$, the time when $x_\mathrm{p} - v_\mathrm{C} t$ becomes greater than the threshold distance $x_\mathrm{th} = 20\lambda_\mathrm{L}$, which we choose to be slightly greater than the spot size, and the longitudinal dimension of region R is about 15 wavelength, as shown in Figure 5.6(a). The y-direction in the integration is decided from the initial condition $E_{x,\mathrm{1D}} = E_{x,\mathrm{2D}}$ as a continuous connection between these two models. We can therefore obtain the equation of motion similar to Equation (5.1) but substitute the acceleration term as

$$\frac{\mathrm{d}(\gamma_\mathrm{p} v_\mathrm{p})}{\mathrm{d}t} = \frac{eE_x}{m_\mathrm{p}} = \begin{cases} \dfrac{e\sigma_\mathrm{net}}{2\varepsilon_0 m_\mathrm{p}} \coth \dfrac{(x_\mathrm{p} - v_\mathrm{C} t) e\sigma_\mathrm{net}}{4\varepsilon_0 k_\mathrm{B} T_\mathrm{e}}, & x_\mathrm{p} - v_\mathrm{C} t < x_\mathrm{th} \\ \dfrac{e\sigma_\mathrm{net}}{2\varepsilon_0 m_\mathrm{p}} \dfrac{x_\mathrm{th}}{x_\mathrm{p} - v_\mathrm{C} t} \coth \dfrac{x_\mathrm{th} e\sigma_\mathrm{net}}{4\varepsilon_0 k_\mathrm{B} T_\mathrm{e}}, & x_\mathrm{p} - v_\mathrm{C} t \geq x_\mathrm{th} \end{cases} . \tag{5.3}$$

The correction successfully resolves the issue that the acceleration do not approach zero as distance increases and provides a more reasonable result compared with simulation. Furthermore, in real 3D condition, we should consider the electric field as

$$E_x = \frac{e}{4\pi\varepsilon_0 (x_p - v_C t)^2} \int_R n_{net} \, dV \,, \tag{5.4}$$

which decreases even faster with increasing distance.

5.6. Scaling

Since we have demonstrated that performing polarization switch from circular to linear polarization can increase the electron temperature, resulting in larger portion of electrons staying ahead of the proton layer, and consequently generate quasi-monoenergetic protons with higher energy, it is of interest whether there exists an optimal switching time. To explore the relationship between the switching time and the obtainable monoenergy, we perform simulations by varying the switching time by $5T_L$ in each simulation, and display the result in Figure 5.7. The resultant proton quasi-monoenergy is maximized when the laser polarization is switched from circular to linear $t_S = 25T_L$ after hitting the foil, demonstrating the existence of optimal switching time.

The reason for that $t_S = 25T_L$ is an optimal switching time is mainly the balance between the effectiveness of SCR and the complete separation between carbon ions and protons due to the RPA. It is clear that switching to linear polarization can increase the acceleration efficiency of SCR, and one may consider to switch it as soon as possible. However, a principal presumption of SCR is full separation between the carbon ions and protons, which is primarily based on the uneven acceleration of RPA on the charges with different charge-to-mass ratios. Therefore, if the laser polarization is switched before full separation between protons and carbon ions occurs, the efficiency of SCR is reduced and the protons spread out in energy. In Figure 5.7, we

can conclude that the proton energy with an optimal switching time can reach about 30% more than the one achieved with a purely circularly polarized case at $t = 200T_{\mathrm{L}}$, and that the RPA induced charge separation phase is crucial in this mechanism as the proton energy obtained with complete linear polarization is even worse than the one with complete circular polarization.

5.7. Conclusion

In summary, we demonstrated through 2D PIC simulations that polarization switch can increase the energy of quasi-monoenergetic proton by 30% without increasing the input power, indicating that the efficiency is increased by 30% as well. The main reason for such an improvement is due to larger proportion of electrons in front of the proton layer resulting from higher energy, making those electrons pull the protons forward instead of backward. The optimal time to switch from circular to linear polarization with typical input parameters $a_0 = 5$, $l_0 = 0.2\lambda_{\mathrm{L}}$, $n_{\mathrm{e0}} = 8.3n_{\mathrm{cr}}$ and $n_{\mathrm{C0}} : n_{\mathrm{p0}} = 9:1$ for a 70 TW laser is $25T_{\mathrm{L}}$, a time period required for the RPA to completely separate the proton layer from the carbon ion layer. Numerically, we can generate a quasi-monoenergetic proton beam of 80MeV by a laser beam with moderate power of 70TW, which is promising for future applications.

Until this chapter, all the cases studied are using continuous input laser with fixed amplitudes as input parameters to simplify the calculation. In such case, for example, we can substitute the integration in Equation (2.27) into a simple multiplication. However, it is not practical nor efficient to actually use continuous wave in accelerating protons, especially while knowing that energy conversion efficiency

decreases after penetration. In the next chapter, we then use a more realistic laser pulse to show that the acceleration scheme discussed thus far is still valid and practical. Furthermore, optimization of laser spot size with fixed pulse power and total energy is also presented.

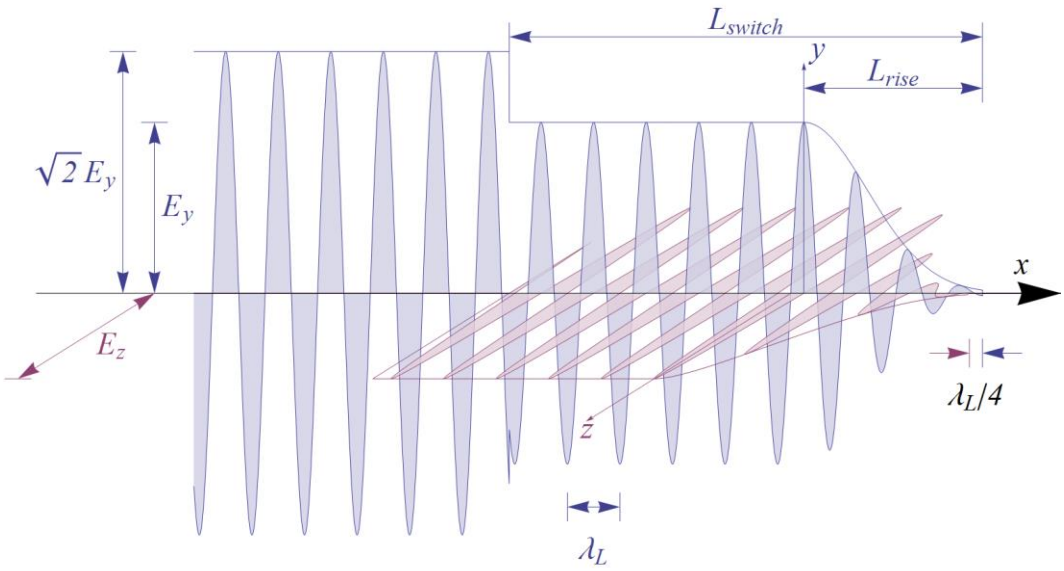

Figure 5.1: The profile along the $x-$axis of the injected laser electric field. The parameter L_{switch} in the figure is denoted as L_{S} in the text.

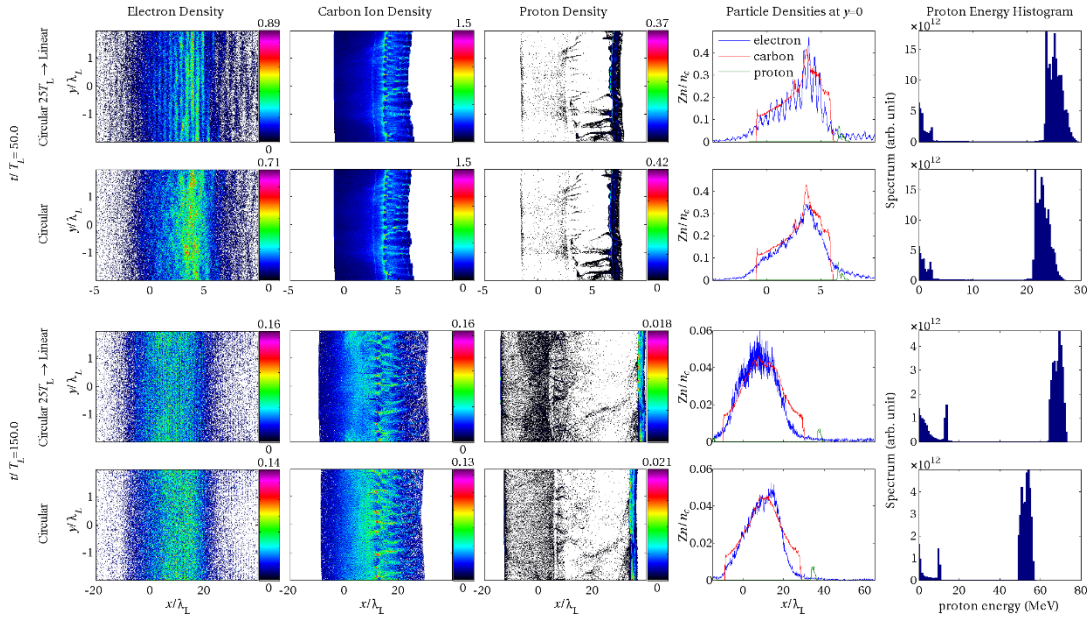

Figure 5.2: Comparison of particle densities and proton energy between cases with and without polarization switch. The upper half panels show simulation data at $t = 50T_{\mathrm{L}}$, and the lower half ones at $t = 150T_{\mathrm{L}}$. The first and third rows show cases with laser switching from circular to linear polarization with $L_{\mathrm{S}} = 25\lambda_{\mathrm{L}}$, and the second and fourth rows show cases one with circular polarization. The columns from left to right are respectively the data of electron, carbon ion and proton density distribution, all particle densities at the center axis and proton energy histogram.

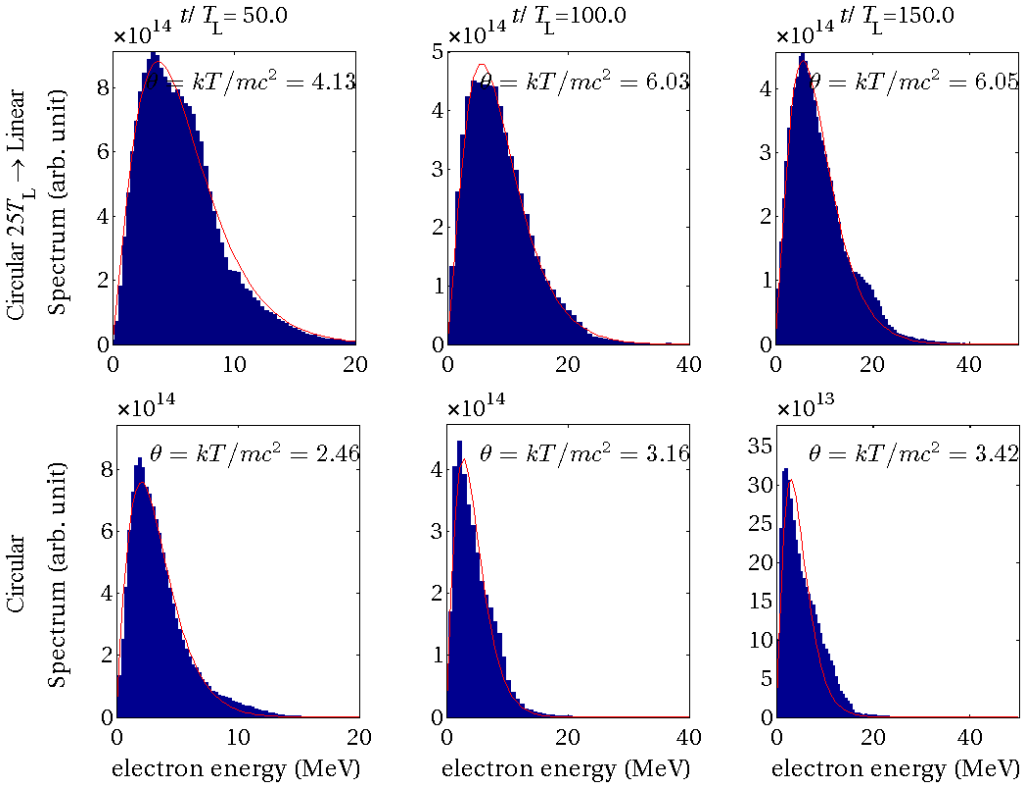

Figure 5.3: The electron energy histogram in the center-of-mass frame for the cases with and without polarization switch. The upper and lower rows show histograms with and without polarization switch, respectively. The red curves in the first two rows are fittings of relativistic Maxwellian distributions with temperatures shown on the plots. The data are shown at $t = 50T_{\mathrm{L}}, 100T_{\mathrm{L}}$ and $150T_{\mathrm{L}}$ from the first to the third column, respectively.

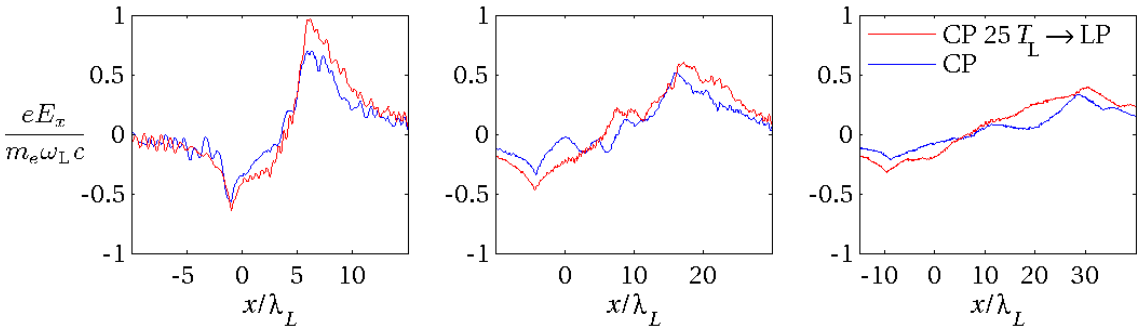

Figure 5.4: The electrostatic field for the cases with and without polarization switch. The normalized electric fields in *x* direction are shown, where the red curves are the longitudinal electric field with polarization switch, and the blue curves without polarization switch. The data are shown at $t = 50T_L, 100T_L$ and $150T_L$ from the first to the third column, respectively.

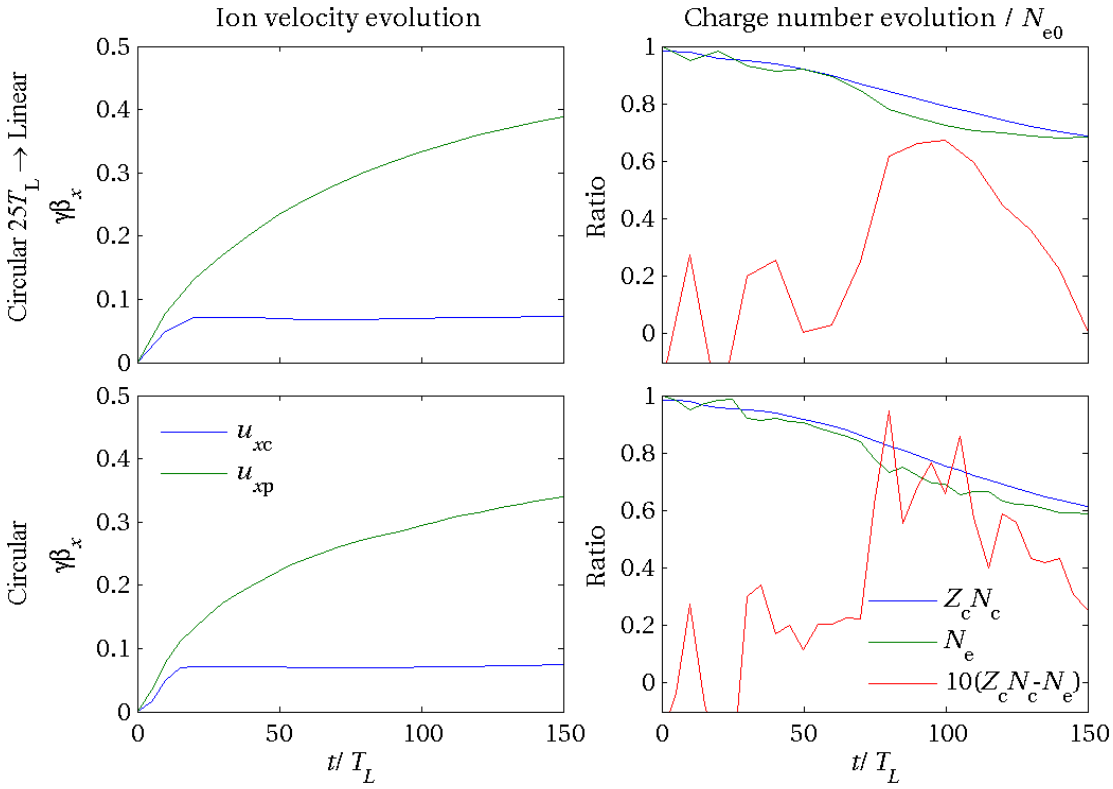

Figure 5.5: The evolution of particle momentum (the first column) and number (the second column) with and without polarization switch. The upper and lower rows are the switching and non-switching cases, respectively. In the figure of particle number, the charge difference (red line) is scaled up ten times to feature the comparison between cases.

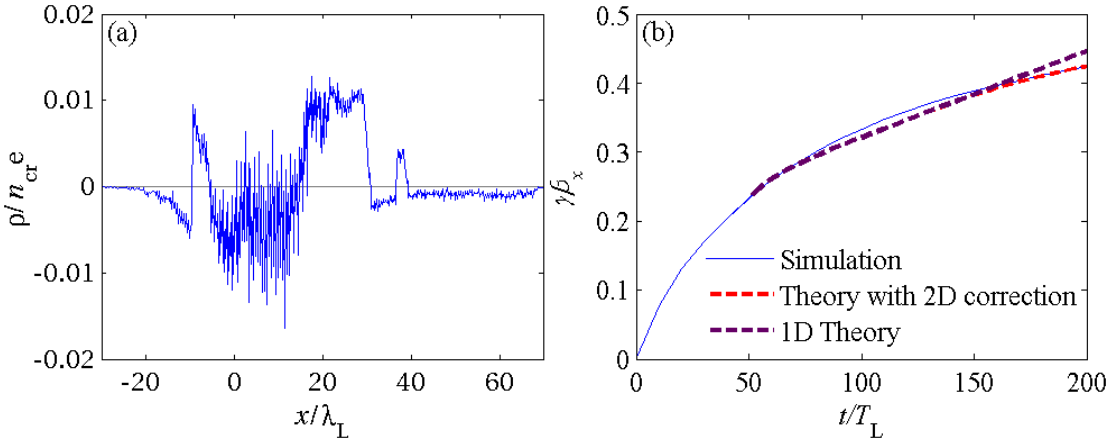

Figure 5.6: The evolution of particle momentum (the first column) and number (the second column) with and without polarization switch. The upper and lower rows are the switching and non-switching cases, respectively. In the figure of particle number, the charge difference (red line) is scaled up ten times to feature the comparison between cases.

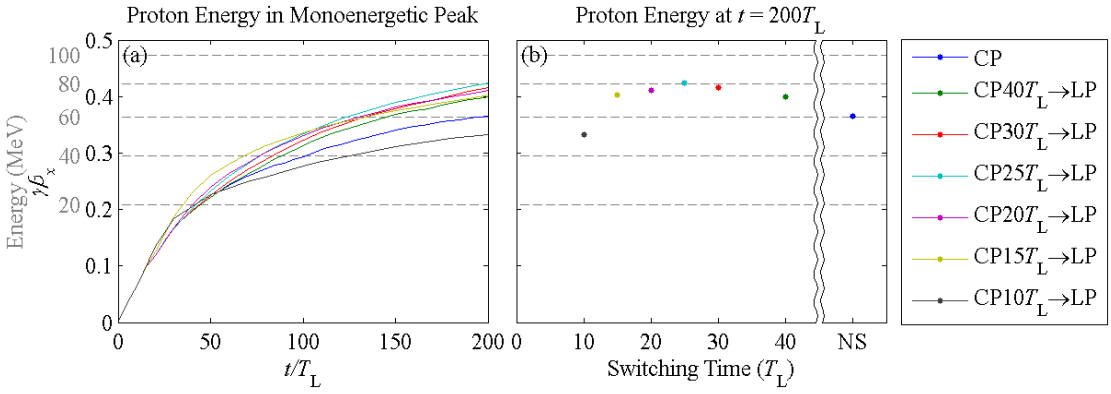

Figure 5.7: (a) Momentum evolution of quasi-monoenergetic protons with switching time scaling from 10 to 40 wave periods. The dashed lines indicate the equivalent energy scale. (b) The proton energy at $t = 200T_L$ for different switching times, where NS denotes the non-switching case. The optimal time of switching is $t_S = 25T_L$.

Chapter 6

Optimization in Laser Spot Size using a Short Laser Pulse

In this chapter, we present a numerical study of the effect of the laser spot size of a circularly polarized laser beam on the energy of quasi-monoenergetic protons in laser proton acceleration using a thin carbon-hydrogen foil. The used proton acceleration scheme is a combination of laser radiation pressure and shielded Coulomb repulsion due to the carbon ions. We observe that the spot size plays a crucial role in determining the net charge of the electron-shielded carbon ion foil and consequently the efficiency of proton acceleration. Using a laser pulse with fixed input energy and pulse length impinging on a carbon-hydrogen foil, a laser beam with smaller spot sizes can generate higher energy but fewer quasi-monoenergetic protons. We studied the scaling of the proton energy with respect to the laser spot size and obtained an optimal spot size for maximum proton energy flux. With such an optimal spot size, we can generate an 80 MeV quasi-monoenergetic proton beam containing more than 10^8 protons using a laser beam with power 250 TW and energy 10 J.

6.1. Introduction

In order to acquire quasi-monoenergetic protons, the scheme of laser RPA has been actively studied in theory and simulations[36–42,44,46] and experiments[49,62]. By using a thin composite foil made of carbon and hydrogen, it was demonstrated in previous chapters that there are two different stages of acceleration to further push the proton forward – RPA and SCR. In the SCR stage of laser acceleration of protons from a multi-ion foil, there are two crucial factors deciding the acceleration efficiency, the

carbon-proton ratio and the laser spot size. Clearly the total charge of the electrons in a neutralized foil is always greater than that of the carbon ions, and therefore after the electrons become underdense and cease to be accelerated by the radiation pressure, a majority of them will return to the carbon layer and slow down the acceleration of the protons. Therefore, in order to successfully accelerate the protons, we should both decrease the charge difference between carbon ions and electrons, and keep the electrons from returning to the carbon layer. In previous chapter, we has studied the first factor and concluded that higher carbon concentration leads to increased proton energy. In this chapter, we focus on the effect of the spot size. We present that a small spot size can help to repel the electrons in the transverse direction and keep them away from the central axis of the laser beam, generating an environment with abundant positive charges due to the carbon ions. Using a laser pulse with power 250 TW and energy 10J, we can obtain a beam of quasi-monoenergetic protons with energies exceeding 100 MeV, which is promising for medical applications.

6.2. Simulation Setup

In order to demonstrate the acceleration process for different spot sizes, we employ two-dimensional (2D) particle-in-cell (PIC) simulations. The simulation domain is $-50 \le x/\lambda_{\mathrm{L}} \le 100$ and $-25 \le y/\lambda_{\mathrm{L}} \le 25$, and the grid size is $\lambda_{\mathrm{L}}/100$ in x dimension and $\lambda_{\mathrm{L}}/50$ in y dimension, where $\lambda_{\mathrm{L}} = 800\,\mathrm{nm}$ is the laser wavelength. The boundary conditions are absorbing at all boundaries for particles and fields, and the laser wave is injected at the negative x-boundary. The foil, consisting of 90% carbon and 10% hydrogen, is initially located at $0 \le x \le l_0$ with initial thickness

$l_0 = 0.15\lambda_L$ and electron density $n_{e0} = 49n_{cr}$ and is resolved by 100 macro-particles of each species per cell. Here $n_{cr} = \varepsilon_0 m_e \omega_L^2 / e^2$ is the critical density, where m_e is the mass of an electron, e is the elementary charge, ε_0 is the vacuum permittivity and ω_L is the laser angular frequency. The amplitude of the incident laser has a Gaussian profile in the transverse direction with spot size, defined as the diameter $d = 2w_0$ at e^{-2} of the peak intensity, and a half-sine wave in time profile with a full duration of $30T_L$, where w_0 and $T_L = \lambda_L / c_0$ are respectively the waist size and the wave period.

6.3. Simulation Result and Analysis

We compare the simulation results using two different spot sizes being $w_0 = 5.0$ and $w_0 = 7.5$, where the input laser peak amplitudes for the two cases are $a_0 = 15$ and $a_0 = 10$, respectively, such that the total power of the input laser are kept identical. Figure 6.1 shows the comparison of the density distribution of each species in these two cases at $t = 30T_L$, when the tail of laser pulses reaches the foil. We can see that the foil moves further due to a greater ponderomotive force in the case with smaller spot size and larger peak amplitude. On the other hand, with greater spot size, the foil moves more uniformly and can maintain the layer structure for a longer time. We also observe that the typical size of the density perturbation in the transverse direction due to the RTI is smaller in the case with greater spot size, which is consistent with our previous work[44] indicating that a smaller laser amplitude results in larger saturation wavenumber k_s. Figure 6.2 shows the density distributions of each species along with the electrostatic field at the center axis at the same time. Since the electrons in the case

with greater amplitude and smaller spot size are further spread out in both longitudinal and transverse directions, the net positive charge of the carbon-electron layer is larger, providing a greater electrostatic force pushing the proton layer forward compared to the case with smaller amplitude and larger spot size. The reason that the electrons are further spread out in longitudinal direction is because greater input laser amplitude can result in great electron temperature [47], whereas a further electron spread in transverse direction is due to a greater gradient in the laser ponderomotive force. Since these factors both positively contribute to the electrostatic field near the central axis, a more focused laser pulse can significantly further accelerate the proton layer.

Although using a more focused laser beam can significantly increase the acceleration of the proton layer and consequently the energy of the quasi-monoenergetic peak, the disadvantage with a too large transverse gradient in laser intensity is that it inevitably drives away the protons in the transverse direction as well. Therefore, the number of protons accelerated along the central axis is diminished with reduced spot size. Since the shape of carbon-electron layer is also affected by the laser spot size, this effect becomes more and more destructive with time even after the laser pulse has passed. Figure 6.3 shows the density distribution of the charged particles at $t = 100T_{\mathrm{L}}$ when the laser pulses has long passed the foil. Two observations can be made at the later stage of the acceleration process. On one hand, during the time that the laser pulse no longer interacts with the foil, the electrons will gradually return to the carbon layer due to the attractive force, resulting in a reduction in proton acceleration. We observed that the proton acceleration for both cases is significantly smaller at $t = 100T_{\mathrm{L}}$ than during the first 30 wave periods. On the other hand, the evolution of the density

distributions are very different. The charged particles in the case with smaller laser spot size are blown out more thoroughly so that the density of the proton layer is only about 20% compared to the case with larger spot size. Therefore, if we evaluate the energy conversion efficiency as the total energy of the proton layer divided by the input laser energy, a more focused laser beam may not always lead to a higher value.

6.4. Scaling

Two questions arise from the observations described above. On one hand, since the proton acceleration with large laser spot size is evidently smaller, it is of interest whether there is a criterion for an optimal laser spot size for quasi-monoenergetic acceleration of the protons. Since the Coulomb repulsion is based on the positive net charge of the carbon-electron layer due to that a portion of the electrons are blown away from the center part of the carbon layer, using a laser beam with too large spot size may not force the electrons to escape transversely and result in a more neutralized carbon-electron layer. Noticing that the initial charge number of the electrons is actually higher than the total charge of the carbon ions, the carbon-electron layer can easily be totally neutralized if the laser beam fails to push away a large enough amount of electrons from the carbon layer. In this case, the proton layer is no longer accelerated by the SCR process. Therefore, it is crucial to find the criterion of the laser spot size so that the proton layer can be successfully accelerated by SCR. Figure 6.4 shows a comparison of proton energy spectra for different spot sizes from the largest (a) to the smallest one (e). With a large laser spot size, not only are the protons less accelerated, but the energy spectrum is more broadened as well. We can observe in Figure 6.4(c)-(e) that a spot size of $w_0 \leq 5\lambda_L$ is required to have the full-width-half-maximum (FWHM) spread in

proton energy within 15%. Moreover, although with fewer protons, 160 MeV of quasi-monoenergetic protons are obtained in this acceleration scheme. On the other hand, after knowing that a beam of quasi-monoenergetic protons is obtainable if the laser spot size is small enough, it is also important to explore the maximum of the energy conversion efficiency among different spot sizes. Figure 6.5 shows the evolution of average proton energies in the quasi-monoenergetic peaks, total proton numbers and total proton energies near the center axis among different input laser spot sizes. In Figure 6.5(a), in additional to the fact we have discussed above that the energy is negatively relative to the laser spot size, we can also see that the acceleration of protons after the laser pulse, $t > 30T_{\mathrm{L}}$, becomes gradual and soon reaches its saturation value, which is a similar effect regardless of the input spot sizes, showing that the acceleration of SCR decreases with increasing distance between the proton and carbon-electron layers. Moreover, the proton energy spectra at $t = 100T_{\mathrm{L}}$ shown in Figure 6.4 also indicate that the quasi-monoenergetic property of protons with a small enough laser spot size can last for a long time even after the acceleration is saturated [see Figure 6.5(a)], suggesting that SCR is a stable acceleration scheme. In contrast, Figure 6.5(b) shows that the number of protons we can obtain drops drastically while reducing the laser spot size. For example, the number of protons in the quasi-monoenergetic peak in the case with spot size $w_0 = 1\lambda_{\mathrm{L}}$ is less than 10% of the number in the $w_0 = 10\lambda_{\mathrm{L}}$ case. Considering these two factors altogether in order to explore the condition for optimal energy conversion efficiency, we can then observe from Figure 6.5(c) that $w_0 = 5\lambda_{\mathrm{L}}$ is an optimal value of conversion efficiency over these spot size values.

6.5. Conclusions

We have numerically demonstrated the effects of different spot sizes on the two-stage acceleration schemes, RPA and SCR, using a finite laser pulse with a full duration of $30T_{\mathrm{L}}$, peak power of 250 TW and total energy of 10 J irradiated on a carbon-hydrogen thin foil. We compared cases with different laser spot sizes and observed that the optimal value of the spot size is about $w_0 = 5\lambda_{\mathrm{L}}$ for maximal energy conversion efficiency. Using this scheme, $\sim 10^7$ quasi-monoenergetic protons with 160 MeV energy (the maximal proton energy case) or about $\sim 10^8$ quasi-monoenergetic protons with 80 MeV energy (the maximal efficiency case) can be obtained with moderate laser input power and energy, which is promising for future applications.

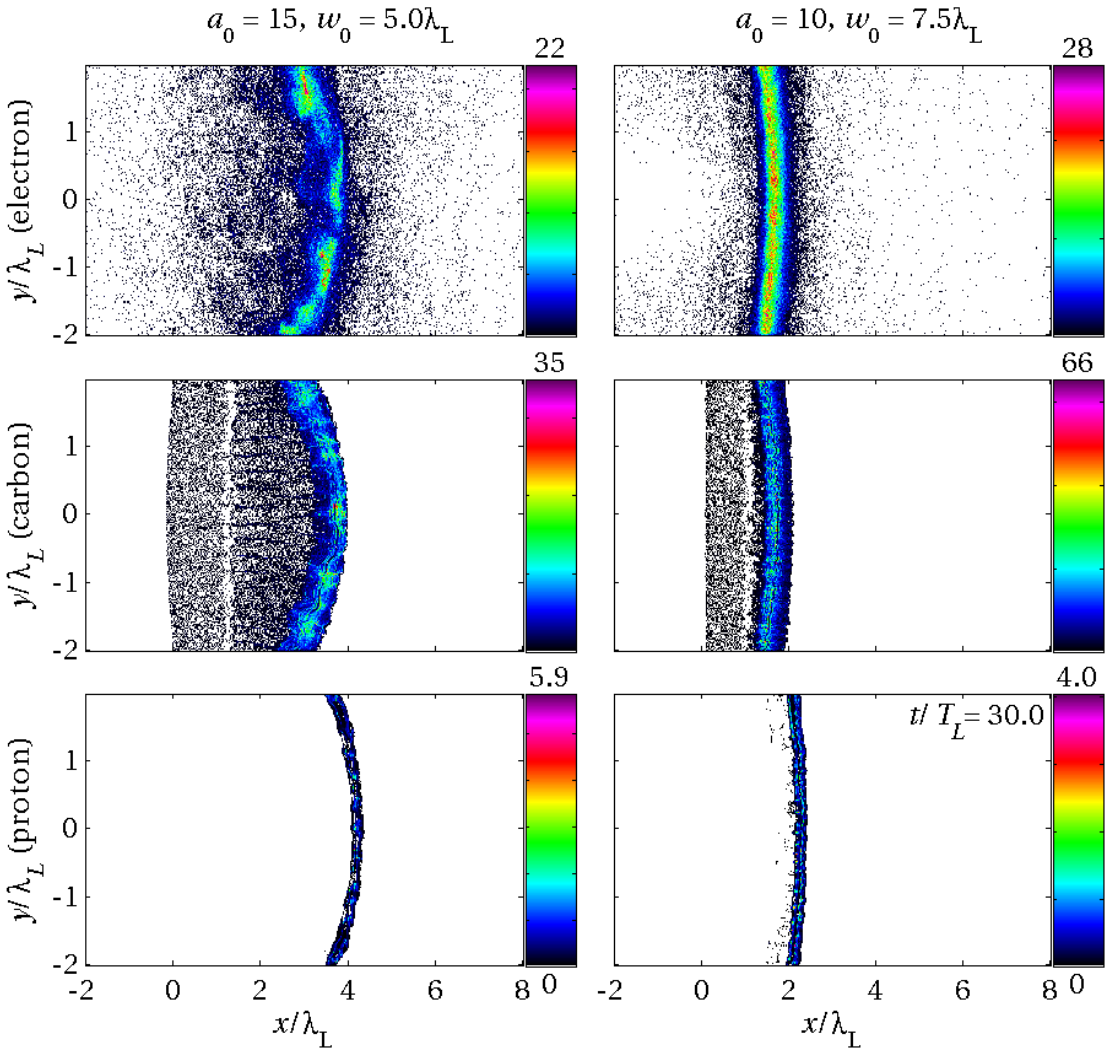

Figure 6.1: The density distribution of electrons, carbon ions and protons (the 1st, 2nd and 3rd rows, respectively) in the cases with input laser parameters being respectively $a_0 = 15$, $w_0 = 5.0\lambda_L$ (the 1st column) and $a_0 = 10$, $w_0 = 7.5\lambda_L$ (the 2nd column) at $t = 30T_L$.

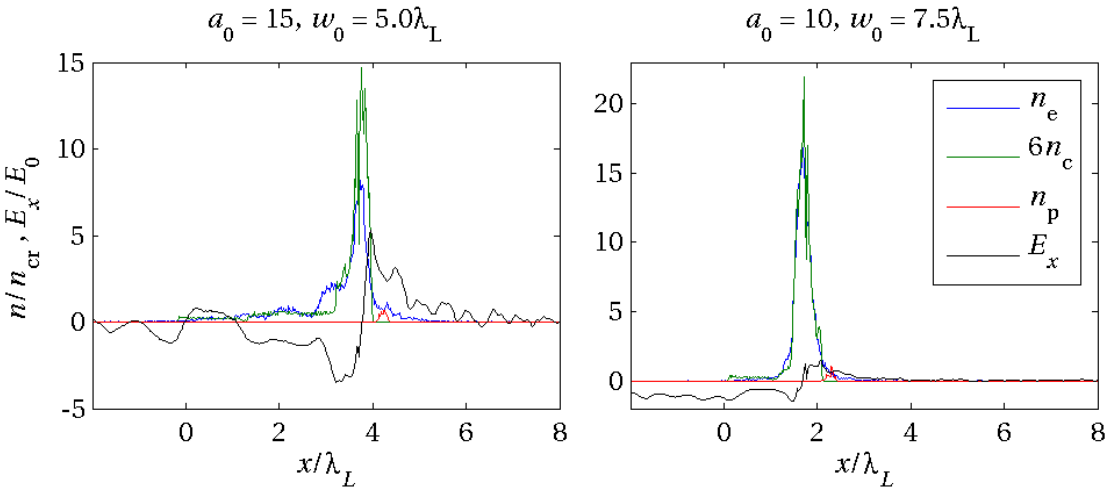

Figure 6.2: The density distributions at $t = 30T_L$ of electrons, carbon ions and protons and electrostatic field at the center axis with the same parameters as in Figure 6.1.

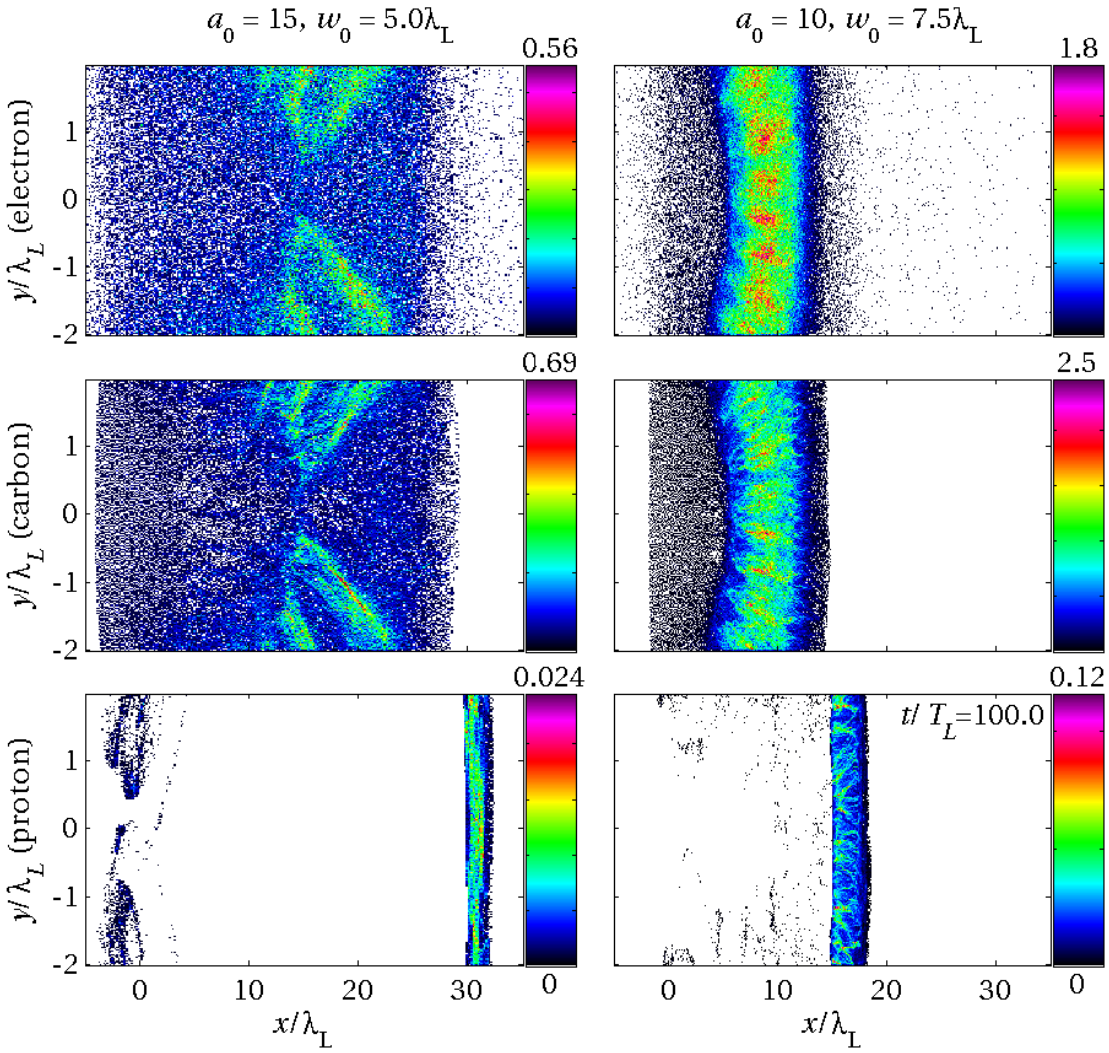

Figure 6.3: The distribution of the charged particles with the same parameters as in Figure 6.1 at $t = 100T_L$.

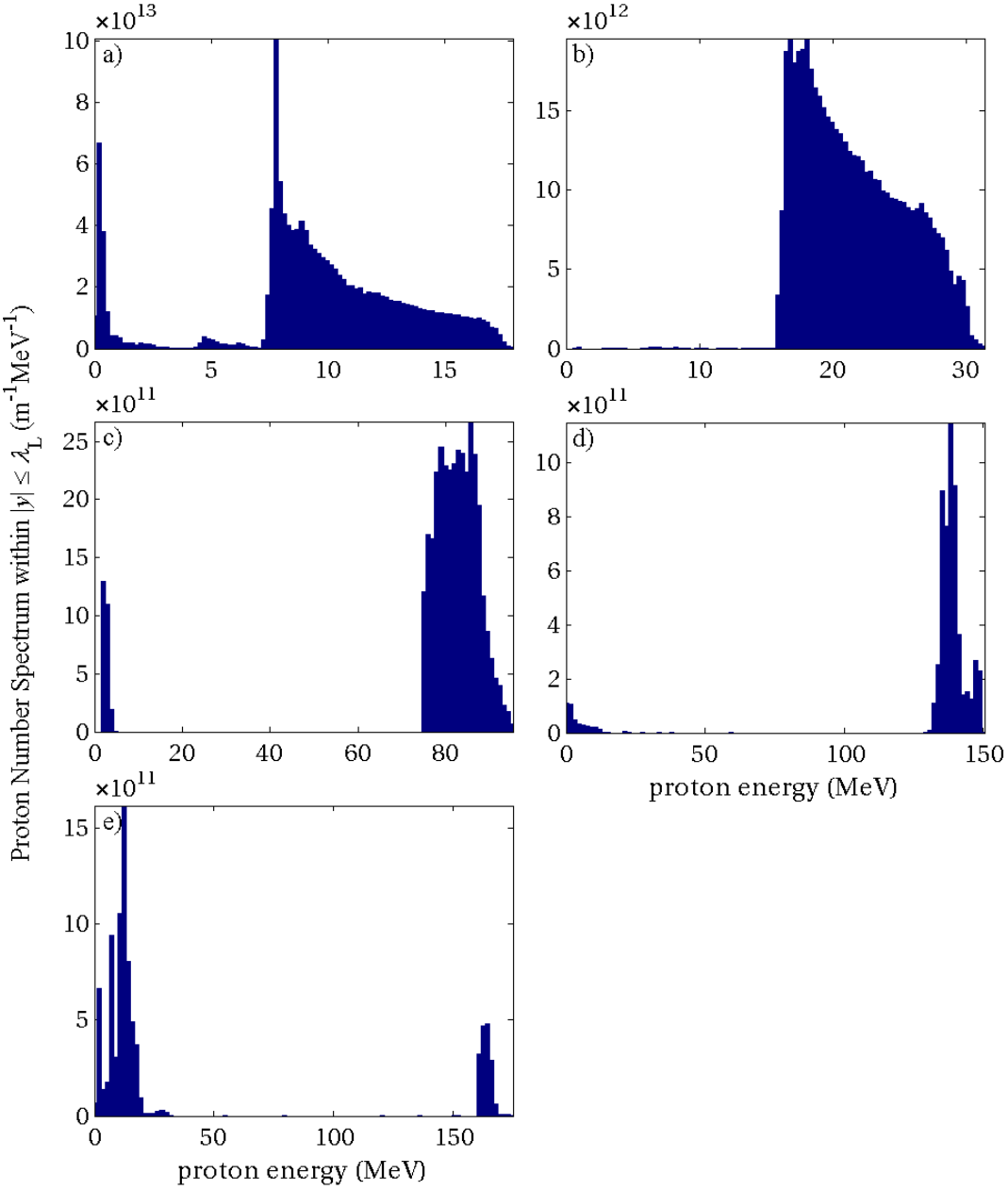

Figure 6.4: The proton energy spectra with different laser spot sizes at $t = 100T_{\mathrm{L}}$. The input parameters are (a) $a_0 = 7.6$, $w_0 = 10\lambda_{\mathrm{L}}$, (b) $a_0 = 10$, $w_0 = 7.5\lambda_{\mathrm{L}}$, (c) $a_0 = 15$, $w_0 = 5.0\lambda_{\mathrm{L}}$, (d) $a_0 = 30$, $w_0 = 2.5\lambda_{\mathrm{L}}$ and (e) $a_0 = 76$, $w_0 = 1.0\lambda_{\mathrm{L}}$.

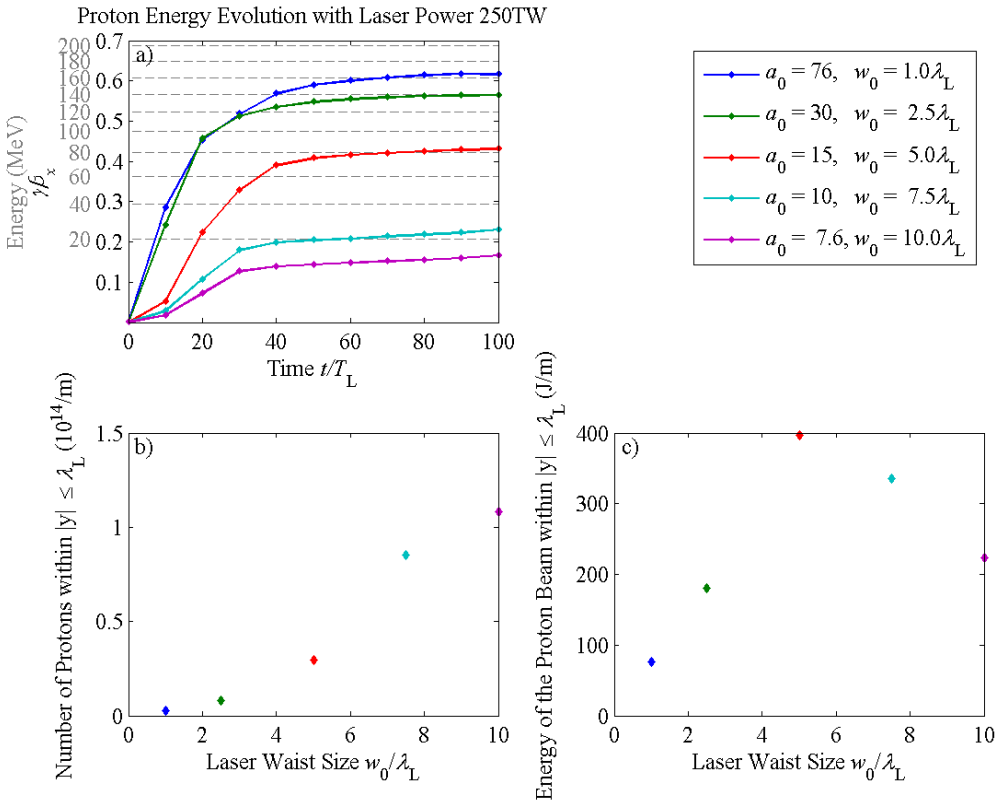

Figure 6.5: The comparison of (a) the evolution of proton momentum, (b) the proton number and (c) the proton energy flux among different input laser spot sizes.

Chapter 7

Medical Implication

In all the previous chapters, we discussed the schemes of generation of a monoenergetic proton beam from an intense laser pulse and verified that a high-energy proton beam is obtainable with well-behaved quasi-monoenergetic property using a laser beam with relatively moderate power. In this chapter, we explore the medical application of proton cancer therapy using the protons generated from the laser proton acceleration schemes. The basic concept determining the quality of proton therapy is the energy dosage in the tissue as a function of position, which is commonly known as a Bragg peak. The more portion that the energy is deposed into the desired region, the less unwanted damage will be done on healthy tissues. In order to reduce the spread of energy dosage, massive particle beams with monoenergetic properties are required. We will compare in this chapter the Bragg peaks caused by a variety of different beams, including the data from the output of PIC simulation and show that the energy spread is significantly reduced by using laser acceleration of multi-species foils.

7.1. Proton Cancer Therapy

Cancer therapy has been one of the most critical and demanding research topics until now. The most direct therapy is to destroy the cancer cells physically by high-energy photon or particle beams. The study of radiation therapy can be traced back to the 19^{th} century when x-ray was discovered by Wilhelm Röntgen in 1895. With the active development of particle acceleration technique in these decades, it was demonstrated that proton therapy holds great promise to revolutionize the treatment of

certain cancers because of the lower collateral damage to healthy tissue, an issue that is critically important for pediatric patients.

Figure 7.1 shows the comparison between these two different therapies. The energy dosage in the tissue caused by a photon beam is the greatest around the surface and decays with increasing depth, causing a large entry dosage near to the surface and finite exit dosage to cause damage on deeper tissues, whereas the dosage caused by a monoenergetic proton beam is concentrated at a specific stopping range so that the damage to the peripheral region is significantly reduced. In practical, the tumor cells may spread out to its vicinity so that a combination of monoenergetic proton beams are superposed to produce a flat structure in energy dosage function. The combined flat shape of these superposed Bragg peaks is called spread out Bragg peak (SOBP), and is currently used as an essential technique in proton therapy.

Figure 7.2 demonstrates the energy dosage, or namely the damage done on the tissues, between these two different therapies. It is apparently that excess radiation due to radiotherapy, as shown in the third column, is widely spread and harmful to healthy tissues, which may put the patients at risk due to various potential complications. Therefore, the importance of developing effective and efficient proton acceleration scheme cannot be overemphasized in contemporary medical technology.

7.2. Bragg Peak of Monoenergetic Ion Beams

To study the dependence of the shape of Bragg peaks to the input proton beam energy, we used a Monte-Carlo simulation tool named SRIM to numerically demonstrate the scaling. Figure 7.3 shows the relationship between the energy deposition distributions and the input proton beam energies varying from 1-100 MeV.

In this figure, we can obviously observe that with greater proton beam energy, the stopping range is also longer, and that a beam of proton with energy of 100 MeV could reach a depth of 8 cm, suitable for dealing with some shallowly resided tumor cells.

Besides the energy of the beam particle, it is also important to understand the dependence of the Bragg peak to the mass of the beam particles, which then explains the reason why using a proton beam is better than an electron beam in particle therapy. Figure 7.4 shows the two dimensional energy dosage maps due to three ion beams with the same energy per nucleon but different charges and masses. In this simulation set, we carefully examine the input ion beams with identical velocity, such that the energy per nucleon is always 50 MeV/u. Compared to a proton beam, we increase the total charge of the ion particle to $+2e$ and search for the mass of the particle so that the stopping depth is the same. The mass that can achieve this goal is $4m_{\mathrm{p}}$, indicating that with the same input velocity, the stopping range of energy dosage is determined by mass per charge squared. This is further verified in the third case where the charge and mass of the beam are respectively $+4e$ and $16m_{\mathrm{p}}$. This is a reasonable result since the recoiling acceleration on the ion is determined by the EM force from the induced dipole of the water molecule, proportional to the ion charge squared (since the induced charge is proportional to the ion charge), divided by the mass of the ion itself, proportional to the ion mass. Moreover, by comparing the energy dosage spread among these beams, it is clear that the damage to the peripheral tissues if significantly reduced using an ion beam with larger mass. We can therefore conclude that using an ion beam with heavier mass can sharpen the Bragg peak and reduce the unwanted energy dosage spread. That is, using a carbon ion beam in particle cancer therapy is better than using a proton beam,

which is still much better than using an electron beam. However, due to a small charge to mass ratio, carbon ion is also more difficult to be accelerated. Since we mainly do proton acceleration in previous chapters, in the next subsection, we still focus on the Bragg peak of proton beams as well.

7.3. Energy Dosage of Proton Beams from Laser Proton Acceleration

After discussing factors in the monochromic ion beams determining the shape of Bragg peaks, we then compute the energy dosage map using real data dumped from the PIC code to see quantitatively the effect of monoenergetic property while injecting such proton beams into the water layer.

Figure 7.5 shows the comparison of the energy dosage of the proton beams acquired from laser proton acceleration between two cases using single- and multi-species foils. The average energy of the proton beams are picked intentionally to be close to each other to make a fair comparison. In the case with single-species foil as shown in the left column of Figure 7.5, a laser beam with higher intensity must be used to reach the same energy level with the multi-species foil cases, as shown in the right column. An obvious bubble structure, the sign of RTI, can also be observed in the single-species foil case, causing the energy spectrum to be rapidly broadened. Moreover, the energy dosage map using the laser accelerated proton from a pure hydrogen foil is clearly not concentrated, indicating that the requirement of the monoenergetic property of the proton beam in medical use is so strict that proton beams generated solely by RPA using a pure hydrogen foil could hardly fulfill such a high standard. In contrary, the shape of Bragg peak of the proton beam generated in the

multi-species case is observably concentrated and focused, indicating that the monoenergetic property of the proton beam generated from multi-species foils is better-behaved and more favorable to be applied in medical applications.

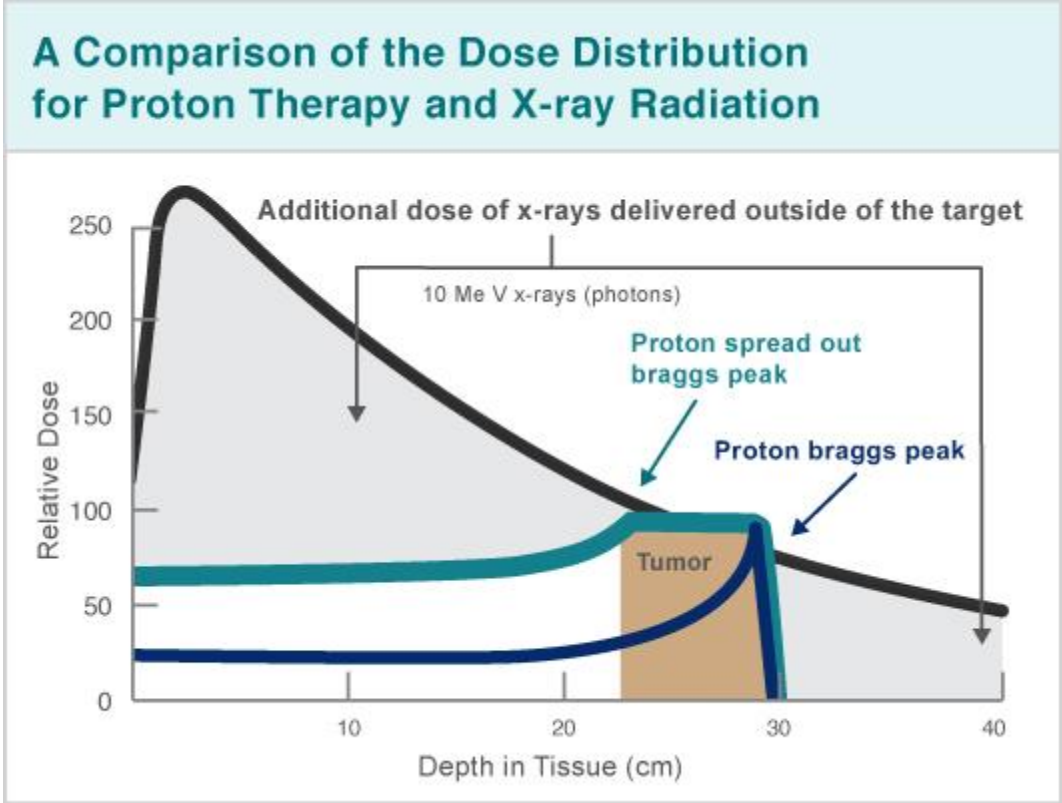

Figure 7.1: The comparison of energy dosage distribution as a function of depth between proton therapy and radiotherapy. Courtesy of Procure Treatment Centers, Inc. (*http://procure.com/*).

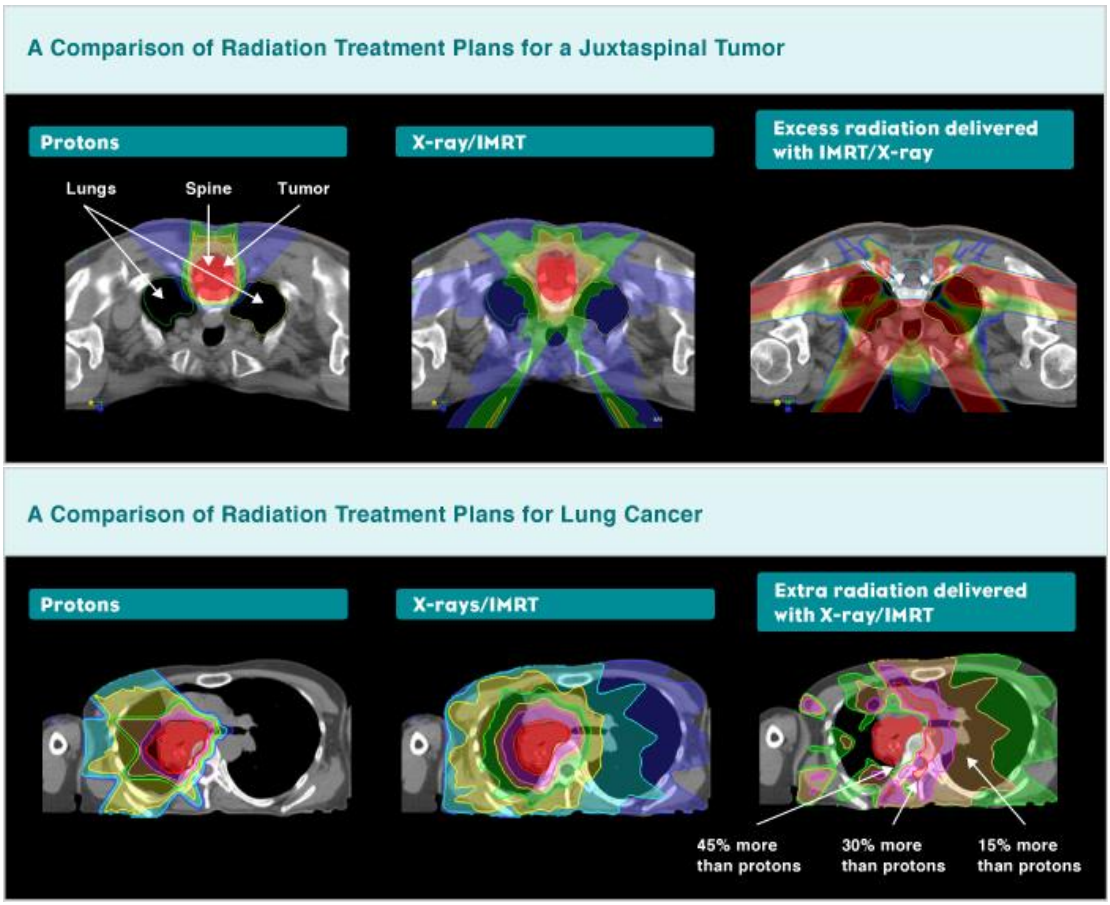

Figure 7.2: The comparison of energy dosage distribution between proton therapy and radiotherapy in a human body. Courtesy of Procure Treatment Centers, Inc. (*http://procure.com/*).

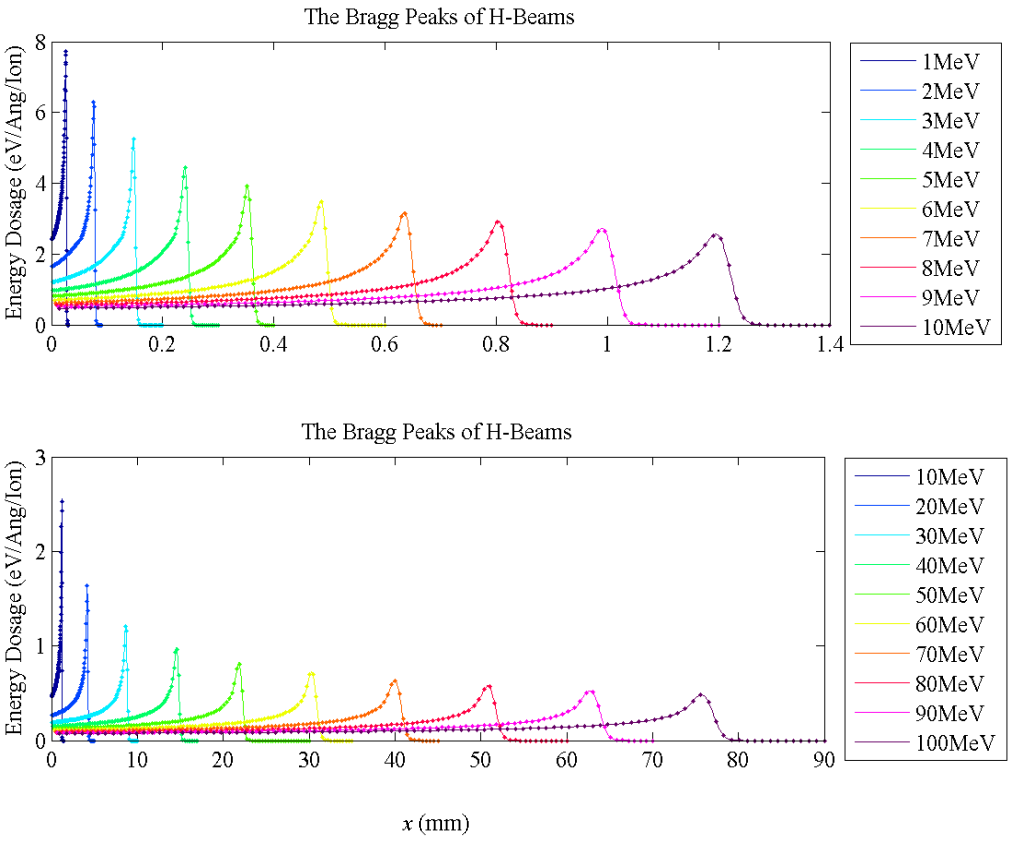

Figure 7.3: The Bragg peak of a monoenergetic proton beam with various input energies. The upper figure shows the Bragg peak of proton beams with moderate proton energy 1-10 MeV, and the lower one shows with greater proton energy 10-100 MeV.

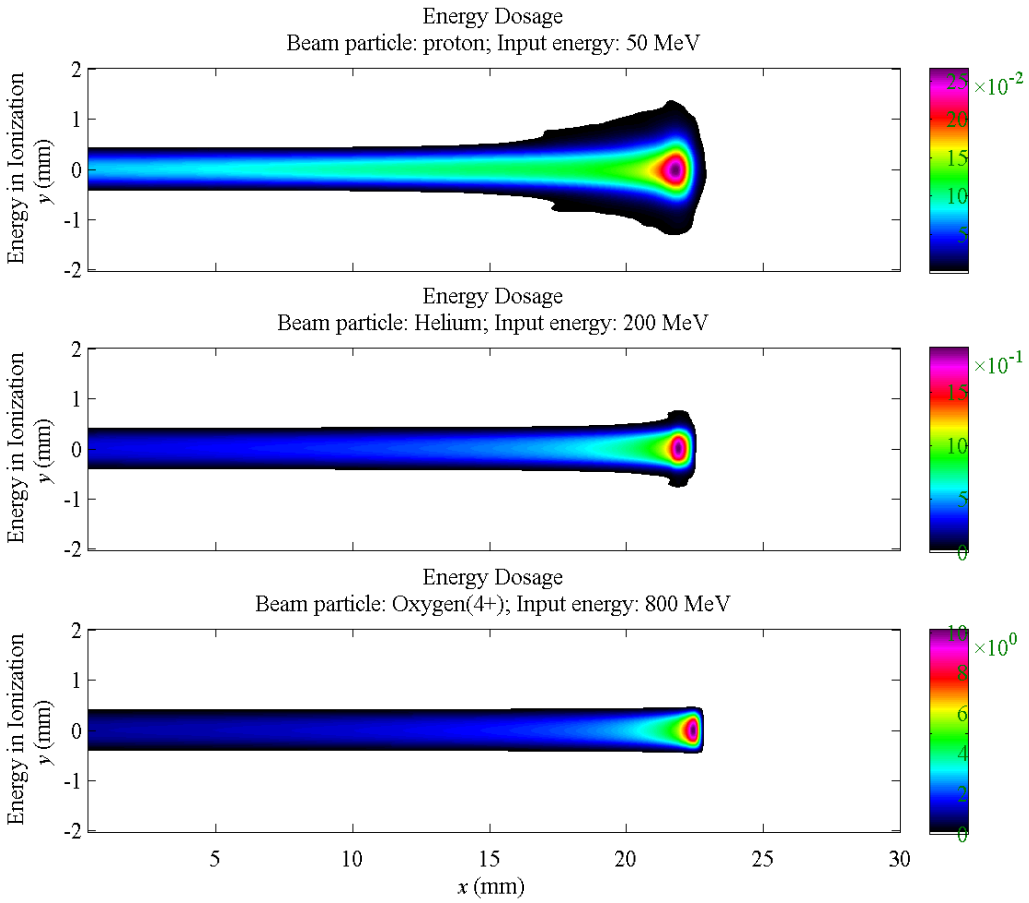

Figure 7.4: Two dimensional distribution of energy dosage due to ion beams with the same input velocity but different charges and masses, which are e/m_p, $2e/4m_p$ and $4e/16m_p$, respectively from the uppermost plot to the lowermost one.

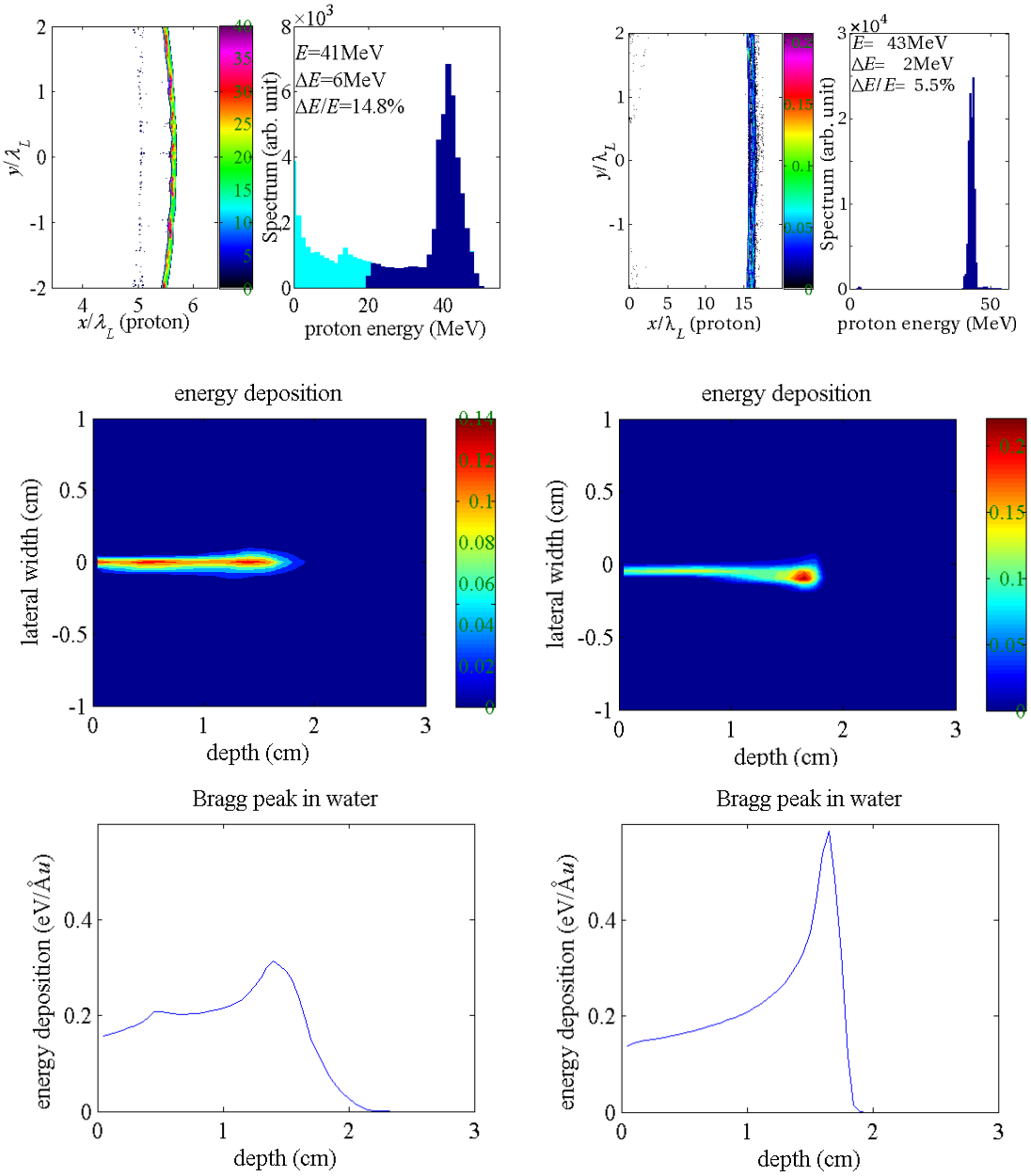

Figure 7.5: A series of comparison between two cases, where the left half is the laser acceleration of proton using a pure hydrogen foil with input parameters $a_0 = 10$, $n_{0e} = 16.7 n_{cr}$, $l_0 = 0.2\lambda_L$, and the right half is the laser acceleration of proton using a multi-species foil with input paramters $a_0 = 5$, $n_{0e} = 8.3 n_{cr}$, $l_0 = 0.2\lambda_L$ and $n_{0C} : n_{0p} = 9:1$. We compare the density distributions, energy spectra, 2D energy dosage distributions and Bragg peaks between these two cases.

Chapter 8

Summary and Future Prospect

We have studied several different mechanisms of laser acceleration of protons and the scaling relationship to optimize the parameters. Using a high-intensity circularly polarized beam to accelerate protons from an overdense ultra-thin foil has been proved to be a promising way to effectively obtain a high-energy quasi-monoenergetic proton beam.

8.1. Summary of Results

In summary, we have derived the theoretical model of the laser radiation pressure acceleration of protons, obtaining their energy evolution and the optimal thickness condition. We discussed the influence of Rayleigh-Taylor instability in two or three dimensions, which effectively limits the acceleration time. We found the scaling of proton energy obtainable while maintaining good beam quality, with respect to the input laser amplitudes using a hydrogen foil with optimal thickness.

In order to remediate the Rayleigh-Taylor instabilities and to improve the obtainable proton energy, multi-species foils are introduced. The carbon component helps to stabilize the RTI of the proton layer and significantly extend the duration of the acceleration. Moreover, it also helps to increase the acceleration of protons by the Coulomb repulsion of Carbons, shielded by thermal electrons. We have calibrated simulation results with theoretical model. Numerically, the effective energy of the accelerated protons could be increased by six times using a foil consist of 90% carbon and 10% hydrogen. That is, with a C-H foil, 60 MeV of quasi-monoenergetic protons

are obtained using a laser beam of 70 TW power, compared with 10 MeV protons for a pure hydrogen foil. This is a promising improvement and could help in ultimately achieving tabletop accelerators for obtaining proton beams of 100 MeV with moderate laser power.

The mechanisms mentioned above could also be applied in a more realistic laser parameter range using a short pulse of 250TW power and 10 J total energy. By scanning the spot size from one to ten laser wavelengths, we obtained a proton beam of 80 MeV and 10^8 particles with maximal energy flux outcome at a spot size of five wavelengths in radius. On the other hand, a quasi-monoenergetic proton beam of 160 MeV energy could also be obtained with 10^7 particles at a spot size of one wavelength in radius.

To further optimize the acceleration efficiency, we switched the laser polarization from circular to linear in the halfway to delay the time for electrons to return and recombine with the carbon ion. The scaling of the proton energy with different scaling time shows that switching the polarization at 25 wave period can help to increase the proton energy by 33% with the laser input energy unchanged.

The results obtained in this research show a promising way to revolutionize the method of accelerating protons in medical use. The Bragg peak of a laser-accelerated proton beam from a multi-species foil is well confined in a small region, implying a minor lateral damage to healthy tissues in particle cancer therapy.

8.2. Future Prospect

In the future, we hope to collaborate with experimental settings and explore the methods to lift the obstacles in limiting the quality of the proton beams that is unsolved

in this thesis work such as the production of a thin foil with desired concentration or the contract ratio issues of a laser beam. Furthermore, we also wish to acquire better computational power in order to be capable of running three-dimensional simulations with sufficient resolution, or assigning an ultrathin foil with high solid density while keeping the grid size less than the Debye length, to better approach the real physical situation during the acceleration. We would also like to study the possibility of utilizing this scheme to the acceleration of heavier ions since there are many advantages of using carbon ion beams in the medical applications. We hope this thesis work could provide some insights in the physics of laser acceleration of protons and contribute to bring affordable tabletop ion accelerator facilities into reality.

Appendix A

Particle-in-Cell Simulation

Particle-in-cell (PIC) simulation is useful in understanding the physics and verifying a theoretical model as it allows observation of the evolution of many physical quantities directly. However, since the number of particles involved in a real physical process is often greater than the ability of computer resources by many orders of magnitude, the simulation are often performed by introducing "macro-particles" and "discretized space and time" as long as the smallest structure of particle interaction is resolved, which is namely the electron Debye length in space and electron-plasma oscillation period in time. Although there are many advance methods which are developed and included in the PIC simulation, the fundamental process of PIC code is mainly a repeat of a three-stage cycle in each time step: using the position and velocity $(\mathbf{x}, \mathbf{v})$ of particles to calculate charge and current density distribution $(\rho, \mathbf{J})$, using such distribution to calculate the evolution of electromagnetic field $(\mathbf{E}, \mathbf{B})$ by Maxwell Equations, and finally updating the position and velocity from the Lorentz force due to the fields.

In order to represent the real situation within affordable computation resources, we should carefully choose the effects to be simplified or neglected and the effects to be carefully calculated in the simulation process. The relativistic effect is fully considered since the electrons in laser acceleration process is highly relativistic. On the other hand, to simplify the complexity, we assumed that the target is pre-ionized without actually computing the detailed ionization distribution of each ion. The

ionization time and final degrees of ionization using a long laser pulse with normalized amplitude $a_0 \approx 1$ and a thick overdense foil consist of carbon and aluminum ions were studied previously [108], and in their results, the majority of carbon ions are highly ionized within a few waveperiods, which implies the applicability of the assumption of fully ionization with a much higher laser amplitude and much thinner. Moreover, we also assumed the process is collisionless, since according to NRL Plasma Formula, the electron collision rate $\nu_{\mathrm{e}} = 2.91\times10^{-6} n_{\mathrm{e}} \ln\Lambda T_{\mathrm{e}}^{-3/2} \mathrm{sec}^{-1} \sim 10^{5}\ \mathrm{sec}^{-1}$ and the ion collision rate $\nu_{\mathrm{i}} = 4.80\times10^{-8} Z^{4} \mu^{-1/2} n_{\mathrm{i}} \ln\Lambda T_{\mathrm{i}}^{-3/2}\ \mathrm{sec}^{-1} \sim 10^{2}\ \mathrm{sec}^{-1}$ are both significantly lower than the frequency scales of the electromagnetic waves and plasma waves.

Bibliography

[1] Maxwell J C 1873 *A treatise on electricity and magnetism* (Oxford : Clarendon Press)

[2] Bartoli A 1884 Il calorico raggiante e il secondo principio di termodinamica *Nuovo Cim* **15** 193–202

[3] Lebedev P 1901 The experimental study of the pressure of the light *Ann. Phys* **6** 433

[4] Einstein A 1917 *Zur Quantentheorie der Strahlung* (Hirzel)

[5] Planck M and Masius M 1914 *The Theory of Heat Radiation* (Blakiston)

[6] Kastler A 1950 Quelques suggestions concernant la production optique et la détection optique d'une inégalité de population des niveaux de quantifigation spatiale des atomes. Application à l'expérience de Stern et Gerlach et à la résonance magnétique *Journal de Physique et le Radium* **11** 255–65

[7] Gordon J P, Zeiger H J and Townes C H 1954 Molecular Microwave Oscillator and New Hyperfine Structure in the Microwave Spectrum of NH_{3} *Phys. Rev.* **95** 282–4

[8] Wideröe R 1928 Ü ber ein neues Prinzip zur Herstellung hoher Spannungen *Archiv f. Elektrotechnik* **21** 387–406

[9] Lawrence E O 1934 Method and apparatus for the acceleration of ions

[10] McMillan E M 1945 The Synchrotron—A Proposed High Energy Particle Accelerator *Phys. Rev.* **68** 143–4

[11] Strickland D and Mourou G 1985 Compression of amplified chirped optical pulses *Optics Communications* **56** 219–21

[12] Cook C E 1960 Pulse Compression-Key to More Efficient Radar Transmission *Proceedings of the IRE* **48** 310–6

[13] Backus S, Durfee C G, Murnane M M and Kapteyn H C 1998 High power ultrafast lasers *Review of Scientific Instruments* **69** 1207

[14] Marx G 1966 Interstellar Vehicle Propelled By Terrestrial Laser Beam *Nature* **211** 22–3

[15] Simmons J F L and McInnes C R 1993 Was Marx right? or How efficient are laser driven interstellar spacecraft? *American Journal of Physics* **61** 205

[16] Kantrowitz A R 1974 Ram Jet Powered by a Laser Beam

[17] Tajima T and Dawson J M 1979 Laser Electron Accelerator *Phys. Rev. Lett.* **43** 267–70

[18] Geddes C G R, Toth C, van Tilborg J, Esarey E, Schroeder C B, Bruhwiler D, Nieter C, Cary J and Leemans W P 2004 High-quality electron beams from a laser wakefield accelerator using plasma-channel guiding *Nature* **431** 538–41

[19] Mangles S P D, Murphy C D, Najmudin Z, Thomas A G R, Collier J L, Dangor A E, Divall E J, Foster P S, Gallacher J G, Hooker C J, Jaroszynski D A, Langley A J, Mori W B, Norreys P A, Tsung F S, Viskup R, Walton B R and Krushelnick K 2004 Monoenergetic beams of relativistic electrons from intense laser–plasma interactions *Nature* **431** 535–8

[20] Faure J, Glinec Y, Pukhov A, Kiselev S, Gordienko S, Lefebvre E, Rousseau J-P, Burgy F and Malka V 2004 A laser–plasma accelerator producing monoenergetic electron beams *Nature* **431** 541–4

[21] Leemans W P, Nagler B, Gonsalves A J, Tóth C, Nakamura K, Geddes C G R, Esarey E, Schroeder C B and Hooker S M 2006 GeV electron beams from a centimetre-scale accelerator *Nat Phys* **2** 696–9

[22] Kneip S, Nagel S R, Martins S F, Mangles S P D, Bellei C, Chekhlov O, Clarke R J, Delerue N, Divall E J, Doucas G, Ertel K, Fiuza F, Fonseca R, Foster P, Hawkes S J, Hooker C J, Krushelnick K, Mori W B, Palmer C A J, Phuoc K T, Rajeev P P, Schreiber J, Streeter M J V, Urner D, Vieira J, Silva L O and Najmudin Z 2009 Near-GeV Acceleration of Electrons by a Nonlinear Plasma Wave Driven by a Self-Guided Laser Pulse *Phys. Rev. Lett.* **103** 035002

[23] Joshi C 2007 The development of laser- and beam-driven plasma accelerators as an experimental field *Physics of Plasmas* **14** 055501–055501–14

[24] Esarey E, Sprangle P, Krall J and Ting A 1996 Overview of plasma-based accelerator concepts *IEEE Transactions on Plasma Science* **24** 252–88

[25] Wilks S C, Langdon A B, Cowan T E, Roth M, Singh M, Hatchett S, Key M H, Pennington D, MacKinnon A and Snavely R A 2001 Energetic proton generation in ultra-intense laser–solid interactions *Physics of Plasmas* **8** 542–9

[26] Pukhov A 2001 Three-Dimensional Simulations of Ion Acceleration from a Foil Irradiated by a Short-Pulse Laser *Phys. Rev. Lett.* **86** 3562–5

[27] Schwoerer H, Pfotenhauer S, Jäckel O, Amthor K-U, Liesfeld B, Ziegler W, Sauerbrey R, Ledingham K W D and Esirkepov T 2006 Laser-plasma acceleration of quasi-monoenergetic protons from microstructured targets *Nature* **439** 445–8

[28] Hegelich B M, Albright B J, Cobble J, Flippo K, Letzring S, Paffett M, Ruhl H, Schreiber J, Schulze R K and Fernández J C 2006 Laser acceleration of quasi-monoenergetic MeV ion beams *Nature* **439** 441–4

[29] Ter-Avetisyan S, Schnürer M, Nickles P V, Kalashnikov M, Risse E, Sokollik T, Sandner W, Andreev A and Tikhonchuk V 2006 Quasimonoenergetic Deuteron Bursts Produced by Ultraintense Laser Pulses *Phys. Rev. Lett.* **96** 145006

[30] Fuchs J, Cecchetti C A, Borghesi M, Grismayer T, d' Humières E, Antici P, Atzeni S, Mora P, Pipahl A, Romagnani L, Schiavi A, Sentoku Y, Toncian T, Audebert P and Willi O 2007 Laser-Foil Acceleration of High-Energy Protons in Small-Scale Plasma Gradients *Phys. Rev. Lett.* **99** 015002

[31] Mora P 2007 Laser driven ion acceleration *AIP Conference Proceedings* **920** 98–117

[32] Yin L, Albright B J, Hegelich B M, Bowers K J, Flippo K A, Kwan T J T and Fernández J C 2007 Monoenergetic and GeV ion acceleration from the laser breakout afterburner using ultrathin targets *Physics of Plasmas* **14** 056706–056706–8

[33] Robson L, Simpson P T, Clarke R J, Ledingham K W D, Lindau F, Lundh O, McCanny T, Mora P, Neely D, Wahlström C-G, Zepf M and McKenna P 2007 Scaling of proton acceleration driven by petawatt-laser–plasma interactions *Nat Phys* **3** 58–62

[34] Yin L, Albright B J, Bowers K J, Jung D, Fernández J C and Hegelich B M 2011 Three-Dimensional Dynamics of Breakout Afterburner Ion Acceleration Using High-Contrast Short-Pulse Laser and Nanoscale Targets *Phys. Rev. Lett.* **107** 045003

[35] Yin L, Albright B J, Jung D, Bowers K J, Shah R C, Palaniyappan S, Fernández J C and Hegelich B M 2011 Mono-energetic ion beam acceleration in solitary waves during relativistic transparency using high-contrast circularly polarized short-pulse laser and nanoscale targets *Physics of Plasmas* **18** 053103–053103–8

[36] Esirkepov T, Borghesi M, Bulanov S V, Mourou G and Tajima T 2004 Highly Efficient Relativistic-Ion Generation in the Laser-Piston Regime *Phys. Rev. Lett.* **92** 175003

[37] Yan X Q, Lin C, Sheng Z M, Guo Z Y, Liu B C, Lu Y R, Fang J X and Chen J E 2008 Generating High-Current Monoenergetic Proton Beams by a CircularlyPolarized Laser Pulse in the Phase-StableAcceleration Regime *Phys. Rev. Lett.* **100** 135003

[38] Liu C S, Tripathi V K and Shao X 2008 Laser Acceleration of Monoenergetic Protons Trapped in Moving Double Layer *AIP Conference Proceedings* **1061** 246–54

[39] Klimo O, Psikal J, Limpouch J and Tikhonchuk V T 2008 Monoenergetic ion beams from ultrathin foils irradiated by ultrahigh-contrast circularly polarized laser pulses *Phys. Rev. ST Accel. Beams* **11** 031301

[40] Tripathi V K, Liu C S, Shao X, Eliasson B and Sagdeev R Z 2009 Laser acceleration of monoenergetic protons in a self-organized double layer from thin foil *Plasma Phys. Control. Fusion* **51** 024014

[41] Robinson A P L, Zepf M, Kar S, Evans R G and Bellei C 2008 Radiation pressure acceleration of thin foils with circularly polarized laser pulses *New J. Phys.* **10** 013021

[42] Eliasson B, Liu C S, Shao X, Sagdeev R Z and Shukla P K 2009 Laser acceleration of monoenergetic protons via a double layer emerging from an ultra-thin foil *New J. Phys.* **11** 073006

[43] Liu C S, Shao X, Eliasson B, Liu T C, Dudnikova G and Sagdeev R Z 2011 Laser Acceleration of Quasi-Monoenergetic Protons via Radiation Pressure Driven Thin Foil *AIP Conference Proceedings* **1320** 104–10

[44] Liu T-C, Shao X, Liu C-S, Su J-J, Eliasson B, Tripathi V, Dudnikova G and Sagdeev R Z 2011 Energetics and energy scaling of quasi-monoenergetic protons in laser radiation pressure acceleration *Physics of Plasmas* **18** 123105–123105–7

[45] Liu C S, Shao X, Liu T C, Su J J, He M Q, Eliasson B, Tripathi V K, Dudnikova G, Sagdeev R Z, Wilks S, Chen C D and Sheng Z M 2012 Laser Radiation Pressure Accelerator for Quasi-Monoenergetic Proton Generation and Its Medical Implications *Progress in Ultrafast Intense Laser Science VIII* Springer Series in Chemical Physics vol 103, ed K Yamanouchi, M Nisoli, W T Hill, A W Castleman, J P Toennies, K Yamanouchi and W Zinth (Springer Berlin Heidelberg) pp 177–95

[46] He M-Q, Shao X, Liu C-S, Liu T-C, Su J-J, Dudnikova G, Sagdeev R Z and Sheng Z-M 2012 Quasi-monoenergetic protons accelerated by laser radiation pressure and shocks in thin gaseous targets *Physics of Plasmas* **19** 073116–073116–5

[47] Liu T-C, Shao X, Liu C-S, He M, Eliasson B, Tripathi V, Su J-J, Wang J and Chen S-H 2013 Generation of quasi-monoenergetic protons from thin multi-ion foils by a combination of laser radiation pressure acceleration and shielded Coulomb repulsion *New J. Phys.* **15** 025026

[48] Macchi A, Cattani F, Liseykina T V and Cornolti F 2005 Laser Acceleration of Ion Bunches at the Front Surface of Overdense Plasmas *Phys. Rev. Lett.* **94** 165003

[49] Henig A, Steinke S, Schnürer M, Sokollik T, Hörlein R, Kiefer D, Jung D, Schreiber J, Hegelich B M, Yan X Q, Meyer-ter-Vehn J, Tajima T, Nickles P V, Sandner W and Habs D 2009 Radiation-Pressure Acceleration of Ion Beams Driven by Circularly Polarized Laser Pulses *Phys. Rev. Lett.* **103** 245003

[50] Snavely R A, Key M H, Hatchett S P, Cowan T E, Roth M, Phillips T W, Stoyer M A, Henry E A, Sangster T C, Singh M S, Wilks S C, MacKinnon A, Offenberger A, Pennington D M, Yasuike K, Langdon A B, Lasinski B F, Johnson J, Perry M D and Campbell E M 2000 Intense High-Energy Proton Beams from Petawatt-Laser Irradiation of Solids *Phys. Rev. Lett.* **85** 2945–8

[51] Pegoraro F and Bulanov S V 2007 Photon Bubbles and Ion Acceleration in a Plasma Dominated by the Radiation Pressure of an Electromagnetic Pulse *Phys. Rev. Lett.* **99** 065002

[52] Palmer C A J, Schreiber J, Nagel S R, Dover N P, Bellei C, Beg F N, Bott S, Clarke R J, Dangor A E, Hassan S M, Hilz P, Jung D, Kneip S, Mangles S P D, Lancaster K L, Rehman A, Robinson A P L, Spindloe C, Szerypo J, Tatarakis M, Yeung M, Zepf M and Najmudin Z 2012 Rayleigh-Taylor Instability of an Ultrathin Foil Accelerated by the Radiation Pressure of an Intense Laser *Phys. Rev. Lett.* **108** 225002

[53] Chen M, Pukhov A, Yu T P and Sheng Z M 2009 Enhanced Collimated GeV Monoenergetic Ion Acceleration from a Shaped Foil Target Irradiated by a Circularly Polarized Laser Pulse *Phys. Rev. Lett.* **103** 024801

[54] Yu T-P, Pukhov A, Shvets G and Chen M 2010 Stable Laser-Driven Proton Beam Acceleration from a Two-Ion-Species Ultrathin Foil *Phys. Rev. Lett.* **105** 065002

[55] Yu T P, Pukhov A, Shvets G, Chen M, Ratliff T H, Yi S A and Khudik V 2011 Simulations of stable compact proton beam acceleration from a two-ion-species ultrathin foil *Physics of Plasmas* **18** 043110–043110–10

[56] Bulanov S S, Brantov A, Bychenkov V Y, Chvykov V, Kalinchenko G, Matsuoka T, Rousseau P, Reed S, Yanovsky V, Litzenberg D W, Krushelnick K and Maksimchuk A 2008 Accelerating monoenergetic protons from ultrathin foils by flat-top laser pulses in the directed-Coulomb-explosion regime *Phys. Rev. E* **78** 026412

[57] Qiao B, Zepf M, Borghesi M, Dromey B, Geissler M, Karmakar A and Gibbon P 2010 Radiation-Pressure Acceleration of Ion Beams from Nanofoil Targets: The Leaky Light-Sail Regime *Phys. Rev. Lett.* **105** 155002

[58] Pae K h., Choi I w. and Lee J 2011 Effect of target composition on proton acceleration by intense laser pulses in the radiation pressure acceleration regime *Laser and Particle Beams* **29** 11–6

[59] Wu D, Zheng C Y, Zhou C T, Yan X Q, Yu M Y and He X T 2013 Suppressing longitudinal double-layer oscillations by using elliptically polarized laser pulses in the hole-boring radiation pressure acceleration regime *Physics of Plasmas* **20** 023102–023102–5

[60] Wang H Y, Yan X Q, Chen J E, He X T, Ma W J, Bin J H, Schreiber J, Tajima T and Habs D 2013 Efficient and stable proton acceleration by irradiating a two-layer target with a linearly polarized laser pulse *Physics of Plasmas* **20** 013101–013101–6

[61] Ali Bake M, Xie B-S, Shan-Zhang and Wang H-Y 2013 Energetic protons from an ultraintense laser interacting with a symmetric parabolic concave target *Physics of Plasmas* **20** 033112–033112–6

[62] Jung D, Yin L, Albright B J, Gautier D C, Hörlein R, Kiefer D, Henig A, Johnson R, Letzring S, Palaniyappan S, Shah R, Shimada T, Yan X Q, Bowers K J, Tajima T, Fernández J C, Habs D and Hegelich B M 2011 Monoenergetic Ion Beam Generation by Driving Ion Solitary Waves with Circularly Polarized Laser Light *Phys. Rev. Lett.* **107** 115002

[63] Wilson R R 1946 Radiological Use of Fast Protons *Radiology* **47** 487–91

[64] Amaldi U and Kraft G 2005 Radiotherapy with beams of carbon ions *Rep. Prog. Phys.* **68** 1861

[65] Jones B 2006 The case for particle therapy *Br J Radiol* **79** 24–31

[66] Fokas E, Kraft G, An H and Engenhart-Cabillic R 2009 Ion beam radiobiology and cancer: Time to update ourselves *Biochimica et Biophysica Acta (BBA) - Reviews on Cancer* **1796** 216–29

[67] Miller D W 1995 A review of proton beam radiation therapy *Medical Physics* **22** 1943–54

[68] Anon 2013 *Particle therapy facilities in operation* (Particle Therapy Co-operation Group)

[69] Ledingham K 2006 Desktop accelerators: Going up? *Nat Phys* **2** 11–2

[70] Ledingham K W D, Galster W and Sauerbrey R 2007 Laser-driven proton oncology — a unique new cancer therapy? *Br J Radiol* **80** 855–8

[71] Bin J, Allinger K, Assmann W, Dollinger G, Drexler G A, Friedl A A, Habs D, Hilz P, Hoerlein R, Humble N, Karsch S, Khrennikov K, Kiefer D, Krausz F, Ma W, Michalski D, Molls M, Raith S, Reinhardt S, Röper B, Schmid T E, Tajima T, Wenz J, Zlobinskaya O, Schreiber J and Wilkens J J 2012 A laser-driven nanosecond proton source for radiobiological studies *Applied Physics Letters* **101** 243701–243701–4

[72] Roth M, Cowan T E, Key M H, Hatchett S P, Brown C, Fountain W, Johnson J, Pennington D M, Snavely R A, Wilks S C, Yasuike K, Ruhl H, Pegoraro F, Bulanov S V, Campbell E M, Perry M D and Powell H 2001 Fast Ignition by Intense Laser-Accelerated Proton Beams *Phys. Rev. Lett.* **86** 436–9

[73] Honrubia J J, Fernández J C, Temporal M, Hegelich B M and Meyer-ter-Vehn J 2009 Fast ignition of inertial fusion targets by laser-driven carbon beams *Physics of Plasmas* **16** 102701–102701–7

[74] Borghesi M, Schiavi A, Campbell D H, Haines M G, Willi O, MacKinnon A J, Gizzi L A, Galimberti M, Clarke R J and Ruhl H 2001 Proton imaging: a diagnostic for inertial confinement fusion/fast ignitor studies *Plasma Phys. Control. Fusion* **43** A267

[75] Cobble J A, Johnson R P, Cowan T E, Renard-Le Galloudec N and Allen M 2002 High resolution laser-driven proton radiography *Journal of Applied Physics* **92** 1775–9

[76] Mora P and Antonsen J 1997 Kinetic modeling of intense, short laser pulses propagating in tenuous plasmas *Physics of Plasmas* **4** 217

[77] Sprangle P, Esarey E, Ting A and Joyce G 1988 Laser wakefield acceleration and relativistic optical guiding *Applied Physics Letters* **53** 2146

[78] Ting A, Esarey E and Sprangle P 1990 Nonlinear wake-field generation and relativistic focusing of intense laser pulses in plasmas *Physics of Fluids B: Plasma Physics* **2** 1390

[79] Sprangle P, Esarey E and Ting A 1990 Nonlinear interaction of intense laser pulses in plasmas *Phys. Rev. A* **41** 4463–9

[80] Joshi C and Katsouleas T 2003 Plasma Accelerators at the Energy Frontier and on Tabletops *Physics Today* **56** 47–53

[81] Clark E L, Krushelnick K, Davies J R, Zepf M, Tatarakis M, Beg F N, Machacek A, Norreys P A, Santala M I K, Watts I and Dangor A E 2000 Measurements of Energetic Proton Transport through Magnetized Plasma from Intense Laser Interactions with Solids *Phys. Rev. Lett.* **84** 670–3

[82] Krushelnick K, Clark E L, Zepf M, Davies J R, Beg F N, Machacek A, Santala M I K, Tatarakis M, Watts I, Norreys P A and Dangor A E 2000 Energetic proton production from relativistic laser interaction with high density plasmas *Physics of Plasmas* **7** 2055

[83] Denavit J 1979 Collisionless plasma expansion into a vacuum *Physics of Fluids* **22** 1384

[84] Mackinnon A J, Sentoku Y, Patel P K, Price D W, Hatchett S, Key M H, Andersen C, Snavely R and Freeman R R 2002 Enhancement of Proton Acceleration by Hot-Electron Recirculation in Thin Foils Irradiated by Ultraintense Laser Pulses *Phys. Rev. Lett.* **88** 215006

[85] McKenna P, Ledingham K W D, Yang J M, Robson L, McCanny T, Shimizu S, Clarke R J, Neely D, Spohr K, Chapman R, Singhal R P, Krushelnick K, Wei M S and Norreys P A 2004 Characterization of proton and heavier ion acceleration in ultrahigh-intensity laser interactions with heated target foils *Phys. Rev. E* **70** 036405

[86] Gaillard S A, Kluge T, Flippo K A, Bussmann M, Gall B, Lockard T, Geissel M, Offermann D T, Schollmeier M, Sentoku Y and Cowan T E 2011 Increased laser-accelerated proton energies via direct laser-light-pressure acceleration of electrons in microcone targets *Physics of Plasmas* **18** 056710–056710–11

[87] Kaluza M, Schreiber J, Santala M I K, Tsakiris G D, Eidmann K, Meyer-ter-Vehn J and Witte K J 2004 Influence of the Laser Prepulse on Proton Acceleration in Thin-Foil Experiments *Phys. Rev. Lett.* **93** 045003

[88] Bochkarev S G, Golovin G V, Uryupina D S, Shulyapov S A, Andriyash A V, Bychenkov V Y and Savel'ev A B 2012 Effect of a short weak prepulse on laser-triggered front-surface heavy-ion acceleration *Physics of Plasmas* **19** 103101–103101–7

[89] Henig A, Kiefer D, Markey K, Gautier D C, Flippo K A, Letzring S, Johnson R P, Shimada T, Yin L, Albright B J, Bowers K J, Fernández J C, Rykovanov S G, Wu H-C, Zepf M, Jung D, Liechtenstein V K, Schreiber J, Habs D and Hegelich B M 2009 Enhanced Laser-Driven Ion Acceleration in the Relativistic Transparency Regime *Phys. Rev. Lett.* **103** 045002

[90] Steinke S, Henig A, Schnürer M, Sokollik T, Nickles P v., Jung D, Kiefer D, Hörlein R, Schreiber J, Tajima T, Yan X q., Hegelich M, Meyer-ter-Vehn J, Sandner W and Habs D 2010 Efficient ion acceleration by collective laser-driven electron dynamics with ultra-thin foil targets *Laser and Particle Beams* **28** 215–21

[91] Steinke S, Hilz P, Schnürer M, Priebe G, Bränzel J, Abicht F, Kiefer D, Kreuzer C, Ostermayr T, Schreiber J, Andreev A A, Yu T P, Pukhov A and Sandner W 2013 Stable laser-ion acceleration in the light sail regime *Phys. Rev. ST Accel. Beams* **16** 011303

[92] Rayleigh 1882 Investigation of the Character of the Equilibrium of an Incompressible Heavy Fluid of Variable Density *Proceedings of the London Mathematical Society* **s1-14** 170–7

[93] Taylor G 1950 The Instability of Liquid Surfaces when Accelerated in a Direction Perpendicular to their Planes. I *Proc. R. Soc. Lond. A* **201** 192–6

[94] Bychenkov V Y, Novikov V N, Batani D, Tikhonchuk V T and Bochkarev S G 2004 Ion acceleration in expanding multispecies plasmas *Physics of Plasmas* **11** 3242–50

[95] Haberberger D, Tochitsky S, Fiuza F, Gong C, Fonseca R A, Silva L O, Mori W B and Joshi C 2012 Collisionless shocks in laser-produced plasma generate monoenergetic high-energy proton beams *Nat Phys* **8** 95–9

[96] Fiuza F, Stockem A, Boella E, Fonseca R A, Silva L O, Haberberger D, Tochitsky S, Gong C, Mori W B and Joshi C 2012 Laser-Driven Shock Acceleration of Monoenergetic Ion Beams *Phys. Rev. Lett.* **109** 215001

[97] Fiuza F, Stockem A, Boella E, Fonseca R A, Silva L O, Haberberger D, Tochitsky S, Mori W B and Joshi C 2013 Ion acceleration from laser-driven electrostatic shocks *Physics of Plasmas* **20** 056304–056304–12

[98] Palmer C A J, Dover N P, Pogorelsky I, Babzien M, Dudnikova G I, Ispiriyan M, Polyanskiy M N, Schreiber J, Shkolnikov P, Yakimenko V and Najmudin Z 2011 Monoenergetic Proton Beams Accelerated by a Radiation Pressure Driven Shock *Phys. Rev. Lett.* **106** 014801

[99] Yu T p., Chen M and Pukhov A 2009 High quality GeV proton beams from a density-modulated foil target *Laser and Particle Beams* **27** 611–7

[100] Markey K, McKenna P, Brenner C M, Carroll D C, Günther M M, Harres K, Kar S, Lancaster K, Nürnberg F, Quinn M N, Robinson A P L, Roth M, Zepf M and Neely D 2010 Spectral Enhancement in the Double Pulse Regime of Laser Proton Acceleration *Phys. Rev. Lett.* **105** 195008

[101] Zhuo H B, Chen Z L, Yu W, Sheng Z M, Yu M Y, Jin Z and Kodama R 2010 Quasimonoenergetic Proton Bunch Generation by Dual-Peaked Electrostatic-Field Acceleration in Foils Irradiated by an Intense Linearly Polarized Laser *Phys. Rev. Lett.* **105** 065003

[102] Chen M, Kumar N, Pukhov A and Yu T-P 2011 Stabilized radiation pressure dominated ion acceleration from surface modulated thin-foil targets *Physics of Plasmas* **18** 073106–073106–4

[103] Verboncoeur J P, Langdon A B and Gladd N T 1995 An object-oriented electromagnetic PIC code *Computer Physics Communications* **87** 199–211

[104] Nieter C and Cary J R 2004 VORPAL: a versatile plasma simulation code *Journal of Computational Physics* **196** 448–73

[105] Jones B 2005 Radiotherapy for the future *BMJ* **330** 979–80

[106] Liseikina T V and Macchi A 2007 Features of ion acceleration by circularly polarized laser pulses *Applied Physics Letters* **91** 171502–171502–3

[107] Rykovanov S G, Schreiber J, Meyer-ter-Vehn J, Bellei C, Henig A, Wu H C and Geissler M 2008 Ion acceleration with ultra-thin foils using elliptically polarized laser pulses *New J. Phys.* **10** 113005

[108] Petrov G M, Davis J and Petrova T 2009 Ionization dynamics of high-intensity laser–target interactions *Plasma Phys. Control. Fusion* **51** 095005